Mitochondria-Lysosome Crosstalk Shapes Metabolic Transition in Neonatal Enterocytes

Gonzalo Herranz,[1,2] Diego Alonso-Larre,[1,2,10] Tamara González,[1,2,10] Laura Akintche,[1,2] Alejandra Ramos-Manzano,[1,2,7] Marta Iborra-Pernichi,[1,2,8], María Velasco de la Esperanza[1,2], Covadonga Díaz-Díaz,[1,2,9] Ian G Ganley,[3] Patricia Boya,[4,5] Sara Cogliati,[6] Nuria Martínez-Martín,[1,2]* and Fernando Martín-Belmonte[1,2,11]**

[1]Program of Tissue and Organ Homeostasis, Centro de Biología Molecular Severo Ochoa, Consejo Superior de Investigaciones Científicas-Universidad Autónoma de Madrid, Madrid, Spain

[2]Intestinal Morphogenesis and Homeostasis Group, Área 3-Cancer, Instituto Ramón y Cajal de Investigación Sanitaria (IRYCIS), Madrid, Spain

[3]MRC Protein Phosphorylation and Ubiquitylation Unit, University of Dundee, Dundee, UK

[4]Dept of Cellular and Molecular Biology, Centro de Investigaciones Biológicas Margarita Salas, CSIC, Madrid, Spain

[5]Department of Neuroscience and Movement Science, Section of Medicine, University of Fribourg, Fribourg, Switzerland

[6]Program of Physiological and Pathological Processes, Centro de Biología Molecular Severo Ochoa, Consejo Superior de Investigaciones Científicas-Universidad Autónoma de Madrid, Madrid, Spain

[7]Present addresses: Immunology Department, Hospital Universitario de La Princesa, Instituto de Investigación Sanitaria (IIS)-Princesa, Madrid, Spain; Medicine Department, School of Medicine, Universidad Autónoma of Madrid, Madrid, Spain

[8]Present address: B Lymphocyte Biology Lab, Centro Nacional de Investigaciones Cardiovasculares (CNIC), Madrid, Spain

[9]Present addresses: Cardiovascular Regeneration Program, Centro Nacional de Investigaciones Cardiovasculares (CNIC), Madrid, Spain; Centro de Investigación Biomédica en Red de Enfermedades Cardiovasculares (CIBERCV), Madrid, Spain

[10]These authors contributed equally

[11]Senior author and Lead contact

*Correspondence: nmartinez@cbm.csic.es

**Correspondence: fmartin@cbm.csic.es

SUMMARY

The neonatal gastrointestinal tract mediates nutrient absorption and the establishment of immune tolerance to commensal microbiota. In early life, lysosome-rich enterocytes (LREs) in the ileum are necessary for the intracellular digestion of maternal milk proteins. However, the molecular mechanisms sustaining their function remain incompletely characterized. Here, we demonstrate that LRE mitochondrial homeostasis and autophagic capacity are critical for efficient nutrient uptake and maintenance of their specialized identity, as disruption of either process leads to premature differentiation into adult enterocytes with diminished endolysosomal and metabolic activity. Transcriptomic profiling further revealed that neonatal LREs exhibit a distinctive antioxidant signature, which preserves redox balance and safeguards the expression of the transcriptional regulators MAFB and BLIMP1, both central repressors of the neonatal-to-adult metabolic transition. These findings establish the mitochondria–lysosome axis as a key determinant of LRE function and neonatal metabolic programming. They also provide a mechanistic framework for understanding how organelle dysfunction and redox imbalance may contribute to early-life malnutrition syndromes, such as Kwashiorkor, and suggest therapeutic strategies aimed at preserving mitochondrial and lysosomal integrity.

KEYWORDS

Intestine, Enterocyte, Autophagy, Mitochondria, Lysosome, Neonatal, Metabolic Switch, ROS, Nutrient Absorption, Mouse

43 **INTRODUCTION**

44 The small intestine is a specialized section of the gastrointestinal tract (GIT) engaged in nutrient digestion
45 and absorption, while simultaneously acting as a barrier against harmful substances. It consists of a variety
46 of cell types, with epithelial and immune cells playing key roles in maintaining intestinal function. Through
47 their interactions with one another and the gut microbiota, these cells help create a finely balanced
48 microenvironment that supports both nutritional and immunological functions (Beumer and Clevers, 2021;
49 Choo et al., 2022). The main absorptive epithelial cells in the intestine are called enterocytes. They are the
50 most numerous cells in the intestinal epithelium and, along with secretory epithelial cells (including Paneth,
51 goblet, and enteroendocrine cells), originate from stem cells of the intestinal crypts (Beumer and Clevers,
52 2021).

53 Dietary protein is a macronutrient essential for growth and overall organismal homeostasis. In weaned
54 mammals, protein digestion takes place in the lumen of GIT, where gastric pepsin and intestinal proteases
55 sequentially break down proteins into oligopeptides and free amino acids, which are then absorbed by
56 enterocytes via specific transporters (Henning, 1981, 1985; Rombout et al., 1985).

57 However, in the intestinal lumen of suckling mammals and stomachless fishes, protease activity remains
58 low and protein digestion is incomplete (Henning, 1981, 1985; Rombout et al., 1985). For this reason, their
59 posterior-mid small intestine contains a population of lysosome-rich enterocytes (LREs), formerly referred
60 to as vacuolated enterocytes (Kleinman and Walker, 1984; Park et al., 2019; Rodríguez-Fraticelli et al.,
61 2015). These cells possess a highly developed endolysosomal system, including a prominent lysosomal
62 vacuole (LV), which is capable of internalising and metabolising intact proteins via non-specific fluid-phase
63 processes (pinocytosis) and receptor-mediated endocytosis and membrane adsorption (Fujita et al., 1990;
64 Gonnella and Neutra, 1984; Park et al., 2019; Rombout et al., 1985). Moreover, LREs facilitate the
65 transcytosis of antigens, maternal immunoglobulins, and antibodies across the epithelial barrier while
66 preserving their biological activity, contributing to the immune system development (Kulkarni and Newberry,
67 2019; Rombout et al., 1985). Recent studies have highlighted the nutritional importance of LREs during the
68 neonatal period. Key endolysosomal proteins, whose absence leads to developmental defects, have been
69 identified, including Mucolipins 1 and 3 (Remis et al., 2014), Pllp (Rodríguez-Fraticelli et al., 2015), Mamdc4
70 (also known as endotubin) (Cox et al., 2018) and Dab2 (Park et al., 2019). Despite these findings, the
71 molecular mechanisms that regulate endocytic and lysosomal pathways in LREs are still not fully
72 understood.

73 Autophagy is a conserved lysosome-dependent catabolic pathway that recycles intracellular components
74 and nutrients. This process involves the sequestration of cytoplasmic material into double-membraned
75 autophagosomes, which subsequently fuse with lysosomes for degradation and breakdown. The lipidation
76 of LC3, a key step in autophagosome formation, is mediated by the ATG12–ATG5–ATG16L1 complex (He,
77 2022; Kaur and Debnath, 2015). Mutations in components of this complex have been linked to intestinal
78 pathologies (Foerster et al., 2022; Larabi et al., 2020), and *Atg5*-deficient neonates exhibit increased

79 neonatal mortality under fasting conditions, underscoring the essential role of autophagy during early
80 postnatal life (Kuma et al., 2004). Despite this, the homeostatic role of autophagy throughout the entire
81 neonatal period, particularly in LRE biology, remains unclear.

82 Autophagy plays a crucial role in cellular metabolism and differentiation, primarily through the selective
83 elimination of mitochondria (mitophagy), thereby contributing to the control of reactive oxygen species
84 (ROS) levels (Wang et al., 2023; Zhong et al., 2024). Beyond their role in energy production, mitochondria
85 and ROS also function as key regulators of cell signalling and differentiation (Lennicke and Cochemé, 2021;
86 Morris and Jasper, 2021; Popov, 2023). In the intestinal epithelium, a gradient of increasing mitochondrial
87 mass, activity, and ROS levels has been described along the crypt–villus axis, correlating with higher
88 degrees of cellular differentiation (Rath et al., 2018). However, how mitochondrial homeostasis and ROS
89 dynamics influence the developmental remodelling of enterocytes remains poorly understood. In particular,
90 their role in regulating the metabolic and functional transition of neonatal LREs into adult enterocytes has
91 not yet been explored.

92 This study reveals that the mitochondria–lysosome axis is essential for the function and maturation of LREs.
93 We show that LREs rely on high autophagic and mitophagic activity to sustain nutrient absorption and
94 lysosomal integrity, and that disruption of either autophagy (*Atg16*cKO) or mitochondrial homeostasis
95 (*Tfam*cKO) leads to impaired endolysosomal function, oxidative stress, and premature weaning transition
96 through the repression of the transcription factors BLIMP1 and MAFB. These findings establish organelle
97 homeostasis as a critical determinant of neonatal enterocyte identity and provide mechanistic insights into
98 how its disruption contributes to early-life malnutrition.

99

100 **RESULTS**

101 ***Lysosome-rich enterocytes (LREs) display heightened basal autophagy levels essential for***
102 ***absorptive function***

103 Unlike adult enterocytes, LREs rely on intracellular digestion within lysosomes to process macromolecular
104 nutrients. This process demands a highly active endolysosomal system that breaks down complex proteins
105 into absorbable units, which confers a particular architecture to LREs (**Figures S1A and S1B**) (Fujita et al.,
106 1990). Autophagy, the cellular mechanism responsible for degrading and recycling cellular components,
107 plays a central role in maintaining lysosomal function and turnover (Yim and Mizushima, 2020). In LREs,
108 elevated basal autophagy may support endolysosomal activity. Exploring this hypothesis could clarify the
109 role of autophagy in the absorption and processing of nutrients in neonates, as well as its contribution to
110 early development.

111 Utilising the GFP-LC3 transgenic mouse model (*GFP-Map1lc3a*$^{TG/+}$) (Mizushima et al., 2004), we visualised
112 autophagosomes as GFP-LC3 positive puncta and monitored autophagy flux via western blot (WB) by
113 assessing the levels of free GFP, a byproduct of lysosomal degradation of GFP-LC3 II (**Figures 1A, 1B and**

114 **S1C**) (Mizushima et al., 2010; Ni et al., 2011). The presence and activity of LREs was determined by probing
115 with mCherry/ fluorescent dextrans that are internalised as a macromolecule by LREs, but not by adult
116 enterocytes (**Figures 1A, 1B, S1C, andS1D**) (Park et al., 2019). Following gavage, fluorescent-dextran was
117 rapidly internalised from the lumen into early and late endosomes (**Figure S1D**, arrowheads), accumulating
118 progressively in lysosomal vacuoles (LVs) (**Figure S1D**, arrows). WB analysis was performed on lysates
119 from epithelial cells in both proximal and distal sections of small intestines from GFP-LC3 mice at neonatal
120 stages (P1, P7 and P14), and post-weaning (P21–30). This analysis revealed a proximal-distal gradient of
121 protein absorption and autophagic degradation, mirroring the anterior-posterior intestinal maturation (**Figure**
122 **1B**) (Spence et al., 2011).

123 In the distal intestine, protein absorption preceded the induction of autophagy, with a subtle onset already
124 detectable at P1, although no free GFP signal was observed. By P7, both mCherry uptake and free GFP
125 increased markedly, with a strong accumulation of free GFP (**Figure 1B**, pink rectangle), indicating peak
126 autophagic activity in LREs—coinciding with the establishment of neonatal intestinal features (Hansson et
127 al., 2011). At P14, mCherry absorption persisted in the distal region, while free GFP levels declined, and
128 by weaning (P21) both signals were absent (**Figure 1B**). Quantification of mCherry and free GFP in distal
129 ileal epithelial lysates at P7 and P21 confirmed these developmental and regional differences (**Figures 1C**
130 **and S1C**).

131 In contrast, the proximal intestine displayed a different temporal profile. At P1, both mCherry and free GFP
132 were already present, but their levels progressively declined, and at P14 only low residual signals were
133 detectable. Note that undegraded GFP-LC3 forms (I and II) and intermediate degradation products
134 accumulated at P21, in both distal and proximal samples (**Figure 1B**).

135 Given these observations, we conclude that LREs maintain elevated autophagy levels relative to adult
136 enterocytes, most probably as a result of their enhanced lysosomal function. To explore the consequences
137 of autophagy disruption in these cells during early development, we utilised a genetic mouse model.
138 ATG16L1 is crucial for both autophagosome formation and LC3 lipidation, two processes essential for
139 autolysosomal degradation (Fujita et al., 2008; Mizushima et al., 2003). This gene has been extensively
140 studied for its association with inflammatory bowel diseases (Foerster et al., 2022; Larabi et al., 2020);
141 nonetheless, its specific role in LRE functionality during the neonatal period remains largely unexplored.
142 For this, we crossed with the *Atg16l1*$^{fl/fl}$ mice (Hwang et al., 2012), with mice expressing the *Villin-creER*^{T2}
143 transgene (el Marjou et al., 2004). This breeding strategy generated an *Atg16l1* knockout offspring in which
144 the *Atg16l1* gene is conditionally deleted in the intestinal epithelium upon administration of tamoxifen
145 (*Atg16*cKO) (**Figure 1D**).

146 Initially, we validated our model via WB analysis by measuring the levels of ATG16L1 and LC3 isoforms
147 (cytoplasmic LC3-I and lipidated LC3-II) in the ileum of both WT and *Atg16*cKO mice at P14 (**Figures 1D**
148 **and 1E**). We observed a significant reduction in ATG16L1 protein levels across all *Atg16*cKO samples,
149 which led to a corresponding decrease in LC3-II/LC3-I ratio (**Figure 1D**). Specifically, our data showed an

150 84.5% reduction in ATG16L1 protein levels and an approximately 8-fold decrease in LC3-II/LC3-I ratio
151 (**Figure 1E**). Furthermore, we observed elevated levels of P62, indicating a reduction in its autophagy-
152 dependent degradation (**Figures 1D and 1E**). These outcomes are consistent with previous results (Cadwell
153 et al., 2008).

154 Subsequently, we examined the developmental trajectory of *Atg16*cKO mice, with a primary focus on their
155 intestinal morphology and function. We observed that the mice reached the post-weaning stage (P30)
156 without apparent issues, showing no weight defects throughout early postnatal development (**Figure S2A**).
157 No significant changes were noted in the length or histological state of the small and large intestines
158 (**Figures S2B and S2C**). However, a reduction in villus length and a decrease in the number of Goblet cells
159 (GCs) were detected in the ileum at P14 (**Figures 1F and 1G**), along with mild oedema at P30, an indicator
160 of inflammation (**Figure S2D**, arrowhead). Inspired by these observations, we quantified specific intestinal
161 epithelial (IEC) and immune cell subpopulations in the ileum of *Atg16*cKO mice at both neonatal and post-
162 weaning stages using flow cytometry (**Figures S2E and S2F**). For this, we applied specific markers to
163 identify various IEC subtypes, including enterocytes and their progenitors (EC), Goblet cells (GC), Paneth
164 cells (PC), and enteroendocrine cells (EEC) (Asano et al., 2017) (**Figure S3**, middle row). We also focused
165 on cells related to innate immunity (IIC), such as CD11b+ cells (including NK cells, granulocytes, and
166 macrophages/monocytes), as well as adaptive immunity, encompassing B lymphocytes (B cells) and CD4+
167 T helper cells (Th cells). We observed an increase in IIC and IEC populations during the neonatal period,
168 accompanied by a concurrent decrease in GC and EEC in adult IECs (**Figure S2E**). In contrast, post-
169 weaning samples showed a rise in B cells, stabilization in IIC and IEC levels, an increase in GC, and a
170 decrease in PC and EEC (**Figure S2F**). These results corroborate our histological findings regarding GCs
171 and inflammation.

172 Next, we investigated the effect of autophagy inhibition on the absorption of macromolecules in the ileum.
173 We gaveged rhodamine B–dextran (Rd-dextran) as a probe in *Atg16*cKO and WT mice as controls (**Figure**
174 **1H**). Our analysis differentiated between the apical and basal regions of enterocytes to assess the
175 sequential entry of Rd-dextran, according to the internalization dynamics observed in these cells (**Figure**
176 **S1D**). Confocal microscopy demonstrated that at P7, *Atg16*cKO enterocytes internalized Rd-dextran
177 similarly to WT counterparts. Nevertheless, it is worth noting that in *Atg16*cKO enterocytes, Rd-dextran
178 levels were slightly elevated in the apical region but reduced in the basal region compared to WT (**Figure**
179 **1H**). This observation suggests a deceleration in the internalisation of macromolecules during this
180 developmental period. Next, at P14, *Atg16*cKO enterocytes exhibited a complete abrogation of
181 macromolecule absorption, resembling post-weaning enterocytes and indicating an advancement in
182 intestinal maturation (**Figure 1H**). To further validate the observed decrease in absorption at P14, we probed
183 neonates from both WT and *Atg16*KO groups with mCherry and quantified the internalised mCherry in the
184 ileum via WB. The results confirmed consistently lower levels of nutrient absorption in *Atg16*KO mice
185 (**Figures 1I and 1J**). Altogether, we conclude that blocking autophagy severely disrupts macromolecule
186 absorption in the neonatal ileum.

187 To further investigate this role autophagy in macromolecule absorption, we examined the expression of the
188 endocytic genes *Dab2*, *Amn*, and *Mamdc4*, as well as the lysosomal genes *Mcoln3*, *Lamp2*, and *Ctsl1*.
189 Previous studies have demostrated the specific role of these genes on the endolysosomal function of LREs
190 (Cox et al., 2018; Park et al., 2019; Remis et al., 2014). Indeed, we validated their expression during early
191 postnatal intestinal development (**Figure 2A**). As expected, an upregulation of these genes was observed
192 in distal samples at P7, coinciding with the presence of LREs (**Figure 2A**). Moreover, a proximodistal
193 expression pattern was observed, consistent with the antero-posterior maturation of the intestine (Spence
194 et al., 2011) (**Figure 2A**).

195 Then, we studied the mRNA expression of *Dab2*, *Mcoln3*, and *Lamp2* genes in both the proximal and distal
196 regions of the small intestines of WT and *Atg16*cKO mice at P7 and P14 (**Figures 2B and S2G**). Since LREs
197 predominantly localise in the distal region, the proximal segment was also analysed to assess potential
198 compensatory mechanisms. In distal *Atg16*cKO samples at P7, mRNA levels of these LRE markers were
199 significantly reduced (**Figure 2B**), while the proximal region showed no significant changes compared to
200 WT mice (**Figure S2G**). By P14, a substantial reduction in gene expression was evident in both proximal
201 and distal *Atg16*cKO mice samples (**Figures 2B and S2G**). Additionally, we analysed *Amn*, *Mamdc4,* and
202 *Ctsl1* mRNA expression in the ileum at P14, finding lower expression levels in the *Atg16*cKO samples
203 (**Figure S2H**).

204 To delve deeper into the protein levels of Dab2, we performed WB and immunofluorescence (IF) analysis
205 in the ileum of *Atg16*cKO mice at P7 and P14. While P7 samples exhibited reduced mRNA expression
206 (**Figure 2B**), Dab2 protein levels remained comparable to WT; however, by P14, a marked reduction in
207 Dab2 was observed in *Atg16*cKO samples (**Figures 2C–2F**).

208 Furthermore, we assess the lysosomal occupancy and content in the apical and basal regions of WT and
209 *Atg16*cKO ileal enterocytes using confocal microscopy with an anti-LAMP1 antibody as a lysosomal marker,
210 as the *Lamp1* and *Lamp2* genes exhibit similar expression patterns (data not shown). Post-weaning (P21–
211 30) WT mice were used as controls (**Figures 2G and 2H**). At P7, both WT and *Atg16*cKO enterocytes
212 exhibited comparable lysosomal occupancy and content, with peak intensity observed in both conditions.
213 However, by P14, while lysosomal occupancy remained similar, *Atg16*cKO enterocytes demonstrated
214 reduced intensity in both the apical and basal regions (**Figures 2G and 2H**). Magnified images also revealed
215 that lysosomes in *Atg16*cKO enterocytes were smaller in P14 neonates, resembling those of adult
216 enterocytes (**Figure 2G**, arrowheads). This reduction in lysosomal content in *Atg16*cKO P14 ileum was
217 further confirmed by WB analysis (**Figures 2I and 2J**).

218 In summary, our results indicate that autophagy plays a crucial role in preserving endolysosomal
219 homeostasis of LREs. Disruption of autophagy in LREs using the *Atg16*cKO mice results in significant
220 defects in macromolecule uptake and lysosomal function, accompanied by the downregulation of key
221 endocytic and lysosomal genes, particularly in the distal ileum of late neonatal mice. These outcomes
222 highlight the importance of autophagy in maintaining LRE function and, consequently, ensuring proper

223 postnatal development. However, the precise mechanisms by which autophagy exerts its effects remain
224 unclear.

225

226 ***LREs show a significant induction of mitophagy to control mitochondrial homeostasis***

227 To elucidate the primary type of autophagy in neonatal enterocytes, we defined the gene expression
228 signature of LREs through bulk RNA sequencing. Leveraging the high levels of macromolecular absorption
229 and autophagy in LREs, we probed neonatal GFP-LC3 mice (P7) with Rd-dextran and isolated LREs from
230 the cellular suspension of the ileum by fluorescence-activated cell sorting (FACS), selecting them as the
231 epithelial cells with high levels of autophagy and Rd-dextran (Dextran^{+}GFP^{high}). Moreover, to highlight their
232 genetic neonatal signature, LREs were compared to mature enterocytes (MECs) from post weaning mice
233 (P42). Following RNA extraction, we conducted next-generation sequencing (NGS) analysis (**Figures 3A**
234 **and S4A**).

235 We detected a total of 1,537 differentially expressed genes (DEGs), of which 1,036 were upregulated and
236 501 were downregulated in LREs (**Figure 3B**). Differential expression analysis and principal component
237 analysis demonstrated that each population exhibited unique enrichment signatures (**Figures S4B and**
238 **S4C**). The computational method of over-representation analysis (ORA) identified which biological
239 processes were overrepresented in the differentially expressed genes (DEGs) (Boyle et al., 2004). The
240 majority of differentially regulated pathways were associated with lysosomal function, nutrient absorption,
241 processing, and transport (**Figures 3C, 3D, and S4D**). These findings are consistent with earlier RNA-Seq
242 data from LREs in zebrafish (Park et al., 2019). Nonetheless, the regulation of lipid metabolism pathways
243 differed (**Figure 3C and S4D**), suggesting that mammalian LREs significantly modulate these pathways to
244 process lipids from maternal milk.

245 Among the most upregulated genes were those associated with endocytosis, such as *Mamdc4*, *Dab2*, and
246 *Amn*, as well as lysosome-associated genes like *Mcoln3* and *Ctsl1* (**Figure 3B**). The upregulation of *Dab2*,
247 *Amn*, and *Lamp2* genes corresponded with previously published ileum transcriptome data from mice and
248 zebrafish (Park et al., 2019). Additionally, the overexpression of *Mamdc4* and *Mcoln3* genes also aligned
249 with earlier results in LREs from rodents (Remis et al., 2014; Wilson et al., 1991). We confirmed elevated
250 levels of *Ctsl1* mRNA expression and lysotracker staining in LREs compared to MECs in WT mice (**Figures**
251 **S4E and S4F**), which validated the RNA-Seq data and ensured that the lysosome-associated pathway was
252 not positively regulated due to the selection of neonatal enterocytes with high autophagy levels.

253 Interestingly, the 'positive regulation of autophagy of mitochondrion ' and 'mitochondrial outer membrane'
254 pathways appeared significantly enriched in LREs (**Figures 3C and 3D**). These outcomes, along with the
255 upregulation of several genes involved in mitophagy, such as *Bnip3*, *Atg10*, and *Map1lc3a* (**Figure 3B**) (Li
256 et al., 2022; Yang et al., 2024), indicated that mitophagy is a significant component of the elevated
257 autophagic activity observed in LREs. To explore this hypothesis, we examined the mRNA expression of

258 the canonical mitophagy genes *Prkn* (Parkin) and *Pink1* (Picca et al., 2023), together with *Bnip3* as a
259 control, in ileal samples from WT mice across developmental stages (E18.5-P42). While *Bnip3* exhibited a
260 progressive decrease in expression throughout development, *Prkn* and *Pink1* showed upregulation in
261 neonatal samples, especially *Prkn* (**Figure 3E**). Moreover, we observed that LREs displayed increased
262 Parkin protein levels compared to MECs through IF (**Figure 3F**).

263 Next, we assessed mitophagy in LREs and MECs using the fixable *mito*-QC reporter C57BL/6J mouse
264 (McWilliams et al., 2016), which ubiquitously expresses a chimeric protein consisting of pH-insensitive
265 mCherry, a pH-sensitive GFP, and the mitochondria-targeting sequence (MTS) from the outer mitochondrial
266 membrane protein FIS1 (amino acids 101–152). This allowed us to differentiate between cytoplasmic
267 mitochondria ($mCherry^{+}GFP^{+}$) and mitochondria degraded by mitophagy in lysosomes ($mCherry^{+}GFP^{-}$)
268 (**Figure 3G**). Confocal images of LREs revealed a high concentration of red-fluorescent mitochondria inside
269 their endolysosomal system (**Figures 3H and 3I**). In fact, when we inhibited autophagic flux by treating the
270 neonates with the protease inhibitor Leupeptin (40 mg/kg for 16 hours) (Jiménez-Loygorri et al., 2024), we
271 observed a significant expansion of LVs and a considerable accumulation of red-only mitochondria within
272 them (**Figure 3H**, arrows; **and 3I**). In contrast, MECs exhibited fewer red mitochondria in lysosomes and
273 a uniform distribution of yellow mitochondria throughout the cytoplasm (**Figures 3H and 3I**).

274 Thus, we confirmed the high mitophagic activity of LREs, suggesting severe impairment of mitophagy and
275 mitochondrial integrity in *Atg16*cKO enterocytes. Indeed, we found that mRNA expression levels of both
276 *Bnip3* and *Prkn* (**Figure 3J**), along with Parkin protein levels (**Figure 3K**), were significantly lowered in
277 neonatal *Atg16*cKO enterocytes. To further investigate the robust mitophagic activity of LREs, we generated
278 an autophagy-deficient *mito*-QC mouse line (*mQ-Atg16*cKO) to evaluate their status. We observed that in
279 *Atg16*cKO LREs exhibited reduced mitochondrial mass within the lysosomes (**Figures 3L and 3M**),
280 consistent with the low mitophagy observed in MECs (**Figures 3L**, lower panels). Therefore, the suppression
281 of autophagy in LREs results in the downregulation of mitophagy-related genes and a reduced uptake of
282 mitochondria into lysosomes.

283 Motivated by these results, we addressed the mitochondrial status of *Atg16*cKO mice. Using transmission
284 electron microscopy (TEM), we analysed mitochondrial damage, quantity, and morphology in ileal
285 enterocytes from neonatal *Atg16*cKO mice (**Figure 4A–4C**). Mitochondria were categorized into three
286 classes based on electron density, cristae appearance, matrix loss, and outer membrane integrity: class I
287 (normal), class II (partially affected), and class III (damaged) (**Figure 4B**) (Moschandrea et al., 2023). For
288 each class, the number, percentage, area, and dimensional ratio (aspect ratio, AR: major axis/minor axis)
289 were quantified (**Figure 4C**). The data showed that number and percentage of mitochondria within each
290 class were similar across both WT and *Atg16*cKO enterocytes. However, while class I mitochondria in
291 *Atg16*cKO enterocytes exhibited a smaller area and a higher AR, class III mitochondria showed a larger
292 area, suggesting an accumulation of damaged mitochondrial mass due to impaired autophagy (**Figure 4C**).

293 To further validate the mitochondrial status, we performed flow cytometry on neonatal *Atg16*cKO
294 enterocytes using mitochondrial probes *ex vivo*: Mitotracker Green for mitochondrial mass, Mitotracker Red
295 CMXROS for membrane potential, and CM-H_2DCFDA for ROS (Asano et al., 2017; Iborra-Pernichi et al.,
296 2024). This analysis confirmed an increase in mitochondrial mass, membrane potential, and ROS in
297 *Atg16*cKO enterocytes (**Figure 4D**). In conclusion, the inhibition of mitophagy in LREs leads to an increased
298 in the mass of dysfunctional mitochondrial.

299 Collectively, mitophagy represents a significant component of the heightened autophagic activity observed
300 in LREs. Its inhibition not only contributes to the mitochondrial defects seen in neonatal *Atg16*cKO
301 enterocytes but may also account for the impairment of their endolysosomal system. These findings
302 highlight a compelling link between the mitochondria-lysosomes crosstalk and neonatal development, as
303 well as the associated metabolic adaptations.

304

305 ***Dysfunction of the mitochondria-lysosome axis in the neonatal epithelium causes an early***
306 ***metabolic switch dependent on BLIMP1 and MAFB***

307 An interesting phenotype observed in neonatal *Atg16*cKO enterocytes was their resemblance to adult
308 enterocytes, particularly in terms of the abrogation of macromolecule absorption and the reduction in
309 endolysosomal system functionality. This phenotype could suggest an acceleration of their metabolic
310 transition. At the end of lactation, the mammalian intestine becomes capable of digesting nutrients
311 extracellularly, replaces LREs with adult enterocytes (without LVs), and regulates the expression of
312 enzymes to adapt to the new solid diet (Henning, 1981; Skrzypek et al., 2007). Previous studies have
313 demonstrated that the transcriptional factors BLIMP1, MAFB, and c-MAF (two members of the Maf family
314 of proteins) mediate the metabolic shift in enterocytes during neonatal development (Bara et al., 2022;
315 Harper et al., 2011; Muncan et al., 2011). At weaning, Blimp1 expression decreases, leading to a
316 downregulation of neonatal enzymes such as β-galactosidase (Glb1) and argininosuccinate synthase 1
317 (Ass1), and an increase in expression of adult enzymes, including sucrase-isomaltase (Sis), trehalase
318 (Treh), and arginase 2 (Arg2) (Harper et al., 2011; Muncan et al., 2011). Similarly, early inhibition of MAFB
319 and c-MAF in neonatal intestine induces a comparable metabolic switch (Bara et al., 2022).

320 Our RNA-Seq analysis comparing LREs and MECs confirmed these dynamics: LREs expressed higher
321 levels of *Mafb*, *Blimp1*, *Glb1*, and *Ass1*, along with a decrease of *Sis*, *Treh*, and *Arg2* (**Figure S5A**). *c-maf*
322 showed no significant differences (**Figure S5A**), though transient regulation at specific neonatal stages
323 cannot be excluded. Consistently, RT-qPCR analysis of proximal and distal small intestine samples from
324 WT mice across development (E18.5–P42) revealed neonatal enrichment of transcription factors and
325 neonatal enzymes, whereas post-weaning samples displayed the opposite profile, with strong induction of
326 adult enzymes (**Figures S5B and S5C**). *Arg2* expression levels closely paralleled those of Sis and Treh
327 (data not shown).

328 To investigate whether autophagy mediated by ATG16 contributes to this transition, we analyzed the
329 temporal expression patterns of these genes in our model. Gene expression analysis revealed a moderate
330 downregulation of the transcription factor genes *Blimp1* and *Mafb*, except for *c-maf*, as well as a more
331 pronounced downregulation of neonatal enzyme genes *Ass1* and *Glb1*. In contrast, there was an
332 upregulation of adult enzyme genes *Treh*, *Sis*, and *Arg2* (**Figure 5A**). Similarly, confocal microscopy
333 analysis revealed reduced levels of MAFB, BLIMP1 (**Figures 5B and 5C**), and ASS1, along with increased
334 levels of TREH in neonatal *Atg16*cKO enterocytes (**Figures 5D and 5E**). This later result was also confirmed
335 by WB analysis in neonates (**Figure 5F and 5G**). In summary, *Atg16*cKO mice advance their metabolic
336 transition in enzymes regulated by MAFB/BLIMP1 in their neonatal epithelium.

337 Next, we studied the metabolic profiles of neonatal enterocytes from *Atg16*cKO mice, in comparison with
338 neonatal and post-weaning WT mice. In order to evaluate deeply the metabolic transition during the
339 neonatal development and the impact of autophagy, we used a pioneer technique called Met-flow. The Met-
340 Flow technique is a flow cytometry-based method that examines the metabolic state of cells by evaluating
341 the levels of rate-limiting enzymes across key metabolic pathways. Specifically, we studied ASS1 and GLS
342 as markers of amino acid (AA) metabolism, HK1 as a marker of glycolysis, CPT1A and ACAC as markers
343 of fatty acid (FA) metabolism, CS and IDH2 for the tricarboxylic acid (TCA) cycle, and ATP5 for oxidative
344 phosphorylation (OXPHOS) (Ahl et al., 2020; Iborra-Pernichi et al., 2024) (**Figure S5D**). Met-Flow analysis
345 revealed higher expression of most metabolic pathways in LREs compared to MECs (**Figure S5E**),
346 reflecting a their hyperconsumptive signature aligned with the high energy demands of this developmental
347 period (Hulzebos and Sauer, 2007). Notably, neonatal *Atg16*cKO enterocytes exhibited a moderate
348 reduction in enzyme protein levels, positioning them between those of WT neonates and post-weaning
349 mice (**Figure 5H**). This intermediate profile is indicative of a globally accelerated metabolic transition toward
350 a more mature state.

351 In summary, our results reveal that autophagy is essential for coordinating mitochondrial and metabolic
352 remodeling during neonatal ileum development and the weaning transition. Suppression of autophagy
353 perturbs endolysosomal and mitochondrial integrity, thereby altering the transcriptional control of LREs.
354 Consequently, LREs undergo a premature metabolic switch, marked by MAFB and BLIMP1 dysregulation
355 and reduced activity of key metabolic pathways.

356

357 ***Mitochondrial homeostasis is critical for maintaining LREs function and their metabolic transition***

358 After identifying mitochondrial homeostasis defects as a downstream consequence of impaired
359 endolysosomal function in the *Atg16*cKO model, we next investigated whether mitochondria themselves
360 play an intrinsic role in sustaining LRE integrity. For this purpose, we used the *Tfam*cKO mouse model
361 (*Tfam*$^{fl/fl}$*/Villin-creER*^{T2}), which enables inducible deletion of Tfam in the neonatal intestinal epithelium. This
362 approach allowed us to directly test whether mitochondrial dysfunction is sufficient to compromise
363 lysosomal homeostasis in LREs.

364 TFAM is a transcription factor that regulates the transcription and replication of mitochondrial DNA (mtDNA)
365 (Campbell et al., 2012). While the role of mitochondria in maintaining intestinal homeostasis has been
366 extensively explored (Rath et al., 2018), and the consequences of Tfam deletion have been reported in
367 both embryonic and adult intestinal epithelium (Srivillibhuthur et al., 2018), its specific contribution during
368 the neonatal stage, and particularly in nutrient absorption and processing by LREs, remains unexplored.

369 We first characterized the general phenotype of *Tfam*cKO pups during the neonatal period. These mice
370 exhibited developmental defects, a generally poor appearance, and significantly reduced body weight,
371 starting around P8, which ultimately compromised their survival and prevented successful weaning (**Figures**
372 **6A–6C**). Given the severity of the phenotype and in adherence with animal welfare guidelines, euthanasia
373 was performed after two consecutive days without weight gain or upon observing weight loss of around
374 10% (**Figure 6C**). Based on the timing of euthanasia, we defined two experimental groups: mice euthanised
375 between P9–P11 (hereafter referred to as P10), and those euthanised between P13–P15 (hereafter
376 referred to as P14). In the ileum of both groups, we confirmed a marked reduction in *Tfam* mRNA expression
377 (**Figure 6D**), accompanied by decreased levels of mtDNA, as assessed through the quantification of
378 electron transport chain-encoded genes including *mt-Nd1*, *mt-Co*1, *mt-Co2*, and *mt-Atp6* (**Figure S6A**). In
379 addition, *Tfam* deletion resulted in a selective loss of mitochondrial gene expression at P10 (*mt-Nd1*, *mt-*
380 *Co2*), while nuclear *Sdha* expression was unaffected (**Figure S6B**). We also observed a significant reduction
381 in MTCO1 (complex IV subunit) protein levels in ileal sections of *Tfam*cKO at P14 (**Figures S6C and S6D**).
382 These results validated our neonatal *Tfam*cKO model and were consistent with findings from other *Tfam*KO
383 models (Baixauli et al., 2015; Chung et al., 2019; Iborra-Pernichi et al., 2024).

384 Further histological examination of the distal small intestine of *Tfam*cKO mice at P10 and P14 revealed
385 substantial structural alterations. The epithelium exhibited clear signs of disorganization and inflammation,
386 characterised by notably shorter, malformed villi, oedema, reduced GCs, and a thicker submucosa and
387 lower mucosa (**Figures S6E–S6H**). Enterocytes also exhibited aberrant vacuoles, suggesting dysfunctions
388 in nutrient processing (**Figure S6E**, arrows).

389 Moreover, flow cytometry analysis of the ileum at P10 and P14 revealed increased percentages of IIC (B
390 cells, and Th cells) in *Tfam*cKO samples (**Figures S6I–S6K**). Given the elevated OXPHOS activity
391 characteristic of intestinal stem cells (ISCs) (Rodríguez-Colman et al., 2017), we assessed ISC populations
392 in ileal sections from P10 and P14 *Tfam*cKO mice via Olfm4 immunofluorescence (**Figure S6L**, arrows),
393 which revealed a marked reduction in Olfm4^{+} crypts (**Figures S6M**). Additionally, lysozyme staining showed
394 a striking increase in mislocalised PCs (**Figures S6N and S6O**). These PCs exhibited mislocalization,
395 aberrant morphologies and enlarged granules, indicative of disrupted crypt architecture and compromised
396 ISC niche homeostasis (**Figure S6N**, arrowheads).

397 With the systemic and intestinal phenotypes of *Tfam*cKO mice defined, we next investigated how loss of
398 TFAM affects mitochondrial homeostasis in LREs. Firstly, mitochondria from *Tfam*cKO enterocytes at P10
399 and P14 were analyzed by TEM, following the same approach previously used in *Atg16*cKO mice. At P10,

400 *Tfam*cKO enterocytes displayed more class I and II mitochondria, with reduced area and AR (**Figures 6E,**
401 **6F, and S6P**). By P14, damaged class III mitochondria increased while class I mitochondria decreased in
402 number, size, shape and AR (**Figures 6E, 6F, and S6P**). This progressive mitochondrial damage resembles
403 that observed in a previously described *Tfam*KO model in renal epithelial cells (Chung et al., 2019). These
404 data were corroborated by subsequent flow cytometry analysis, which revealed increased mitochondrial
405 mass, membrane potential, and ROS levels in neonatal *Tfam*cKO enterocytes (**Figure 6G**), features
406 reminiscent of those observed in TFAM-deficient lymphocytes (Baixauli et al., 2015; Iborra-Pernichi et al.,
407 2024).

408 In summary, deletion of *Tfam* in the neonatal intestinal epithelium severely disrupted mucosal structure and
409 function, leading to developmental defects that culminated in early mortality. Specifically, in LREs, TFAM
410 loss caused the accumulation of damaged mitochondria and increased oxidative stress.

411 We next investigated whether mitochondrial dysfunction could similarly drive an accelerated metabolic
412 transition in neonatal enterocytes, as observed in the *Atg16*cKO model. The microscopy analysis indicated
413 a reduction in the expression levels of BLIMP1 and MAFB, with a more pronounced decrease in BLIMP1
414 (**Figures 6H and 6I**). As a result, we also observed lower levels of ASS1 and elevated expression of TREH
415 in the *Tfam*cKO enterocytes (**Figures 6J and 6K**). These results were further supported by gene expression
416 analyses of metabolic transition genes that are regulated by BLIMP1, MAFB, and c-MAF. We obtained a
417 progressive downregulation of *Mafb*, *c-maf*, *Blimp1*, *Ass1,* and *Glb1*, accompanied by an upregulation of
418 *Treh*, *Sis*, and *Arg2* at P14 (**Figure S7A**). Finally, the activity of key metabolic pathways was assessed in
419 neonatal *Tfam*cKO enterocytes using Met-Flow (Ahl et al., 2020; Iborra-Pernichi et al., 2024), revealing a
420 marked reduction in nearly all metabolic proteins, except for ATP5A (**Figure 6L**), which was increased,
421 possibly due to mitochondrial accumulation or as a compensatory response to mitochondrial dysfunction.
422 Taken together, these findings indicate that neonatal *Tfam*cKO enterocytes undergo a premature metabolic
423 transition, resembling the metabolic profile of adult enterocytes.

424 Following the analysis of mitochondrial defects in TfamcKO neonatal enterocytes, we next investigated
425 whether impaired mitochondrial function also perturbs the endolysosomal system of LREs. Although
426 lysosome–mitochondria crosstalk has been predominantly characterized in the context of mitophagy, our
427 findings suggest a reciprocal layer of regulation, whereby mitochondria control lysosomal biogenesis and
428 function. This bidirectional communication implies that mitochondrial dysfunction not only disrupts energy
429 metabolism but also secondarily compromises lysosomal integrity, thereby exacerbating the metabolic and
430 absorptive defects observed in neonatal *Atg16*cKO enterocytes. Indeed, neonatal *Tfam*cKO enterocytes
431 exhibited a complete loss of Rd-dextran uptake (**Figures 6M and 6N**) and a progressive downregulation of
432 the endocytic genes *Dab2*, *Amn*, and *Mamdc4* (**Figures S7B–S7D**). Subsequently, we characterised a
433 gradual reduction in the expression of lysosomal genes *Lamp2*, *Mcoln3*, and *Ctsl1* (**Figure S7E**),
434 accompanied by a decrease in lysosomal content and size (**Figures 6M, 6O, S7F and S7G**). Thus, neonatal

435 *Tfam*cKO enterocytes recapitulated the phenotype observed in the *Atg16*cKO model, validating a reciprocal
436 interaction between mitochondria and lysosomes in LREs.

437 In conclusion, the *Tfam*cKO model enabled us to establish a bidirectional relationship between mitochondria
438 and lysosomes by recapitulating the endolysosomal defects observed in autophagy-deficient neonatal
439 enterocytes. Furthermore, we confirmed that mitochondrial and lysosomal dysfunction drive an early
440 metabolic switch in LREs. These alterations, alongside epithelial inflammation, developmental delay, and
441 premature death, position the *Tfam*cKO model as a valuable tool for investigating the pathophysiology of
442 childhood malnutrition.

443

444 ***Antioxidant activity in LREs modulates the onset of metabolic switch***

445 After defining the metabolic switch underlying neonatal development, and the early metabolic switch in both
446 *Atg16*cKO and *Tfam*cKO models, we focused on uncovering the mechanisms responsible for this
447 phenotype. The observation that both *Atg16*cKO and *Tfam*cKO models presented heightened ROS levels
448 in enterocytes (**Figures 4D and 6G**) suggested that redox dysregulation may underlie their accelerated
449 metabolic maturation. Indeed, the high mitophagic activity observed in LREs may contribute to the control
450 of ROS (Wang et al., 2023; Zhong et al., 2024). Previous studies have shown that oxidative stress has
451 been reported to repress *c-maf* expression (Chen et al., 2015) and that antioxidant treatment can induce
452 *Blimp1* expression (Qi et al., 2020). Therefore, we hypothesise ROS regulation could represent a critical
453 mechanism for controlling the timing of the metabolic transition in LREs.

454 We found that LREs exhibited significantly higher levels of mitochondrial ROS (mROS) compared to MECs
455 (**Figure 7A**), possibly reflecting their elevated OXPHOS activity (Murphy, 2008). In contrast, total ROS levels
456 were lower in LREs than in MECs (**Figure 7A**), indicating the presence of mechanisms that tightly regulate
457 oxidative stress.

458 Then, we further explored our LREs vs MECs RNA-Seq dataset analysis to identify additional pathways
459 involved in ROS regulation. Numerous pathways related to ROS, ROS response, and antioxidant activity
460 stood out (**Figure 7B and 7C**). Further, there was an overexpression of genes for the antioxidant enzymes
461 Glutathione Peroxidase-3 (Gpx3) and Catalase (Cat) (not shown), suggesting that these antioxidants could
462 be reducing ROS levels in LREs. Indeed, we observed that neonatal ileal samples showed induction of
463 *Gpx3* and *Cat* expression compared to the embryo and post-weaning ileal samples, with the most drastic
464 changes in *Gpx3* (**Figure 7D**). Moreover, in both *Atg16*cKO and *Tfam*cKO neonates, *Gpx3* and *Cat*
465 expression were significantly decreased in the ileum (**Figure 7E and 7F**), and GPX3 protein levels were
466 likewise reduced, as shown by IF (**Figure 7G-J**). Thus, oxidative stress may act as a trigger for the metabolic
467 transition in LREs. To validate this hypothesis, neonatal mice were treated with hydrogen peroxide (H_2O_2)
468 to induce oxidative stress (Liang et al., 2024). mRNA expression analysis revealed a downregulation of the
469 transcription factors *Blimp1*, *Mafb*, and *c-maf*, alongside an upregulation of adult enzymes such as *Treh*

470 and *Arg2*. However, the expression of neonatal enzyme genes *Ass1* and *Glb1* remained unchanged (**Figure**
471 **7K)**. Subsequently, we characterised a reduction of BLIMP1 and ASS1 levels by both IF and flow cytometry
472 (**Figure 7L–7N**), while TREH expression was found to be increased (**Figure 7L and 7M**).

473 The data collectively suggest that elevated antioxidant activity is a key characteristic of LREs. When this
474 antioxidant function is compromised in neonatal *Atg16*cKO and *Tfam*cKO enterocytes, alongside
475 mitochondrial dysfunction, the oxyidative stress rise. This increase in ROS contributes to the repression of
476 genes such as *Blimp1*, *Mafb*, and *c-maf*, ultimately triggering an early metabolic transition (**Figure 7O**).
477 Therefore, this study emphasizses the critical role of mitochondrial-lysosomal coordination in mitigating
478 oxidative stress and regulating the transcriptional programs essential for neonatal intestinal development.
479 Additionally, it paves the way for future research into therapeutic strategies aimed at restoring mitochondria-
480 lysosome homeostasis and redox balance in early gut disorders.

481

482 **DISCUSSION**

483 In this work, we have elucidated new molecular mechanisms fundamental to the function and differentiation
484 of mammalian LREs, highlighting the role of the mitochondria-lysosome axis. Disruption of autophagy in
485 the neonatal gut, either through *Atg16*cKO or mitochondrial dysfunction via *Tfam*cKO, resulted in defective
486 nutrient absorption and a reduction in lysosomal content. Most importantly, *Tfam*cKO neonates exhibited
487 weight loss and premature death, resembling hallmarks of infant malnutrition. Notably, the early enzymatic
488 maturation of *Atg16*cKO and *Tfam*cKO enterocytes indicates a direct connection between autophagic and
489 mitochondrial processes in enterocytic maturation. Additionally, the associated increase in ROS observed
490 in both models may contribute to this metabolic switch by suppressing the expression of transcription factors
491 BLIMP1, MAFB, and c-MAF. These findings are consistent with our transcriptomic data, which reveal
492 upregulation of mitophagy- and antioxidant-related pathways in LREs compared to MECs, supporting the
493 concept that mitochondrial quality control and redox homeostasis are defining features of LRE identity and
494 function. Taken together, our outcomes offer interesting mechanistic insights into the mitochondria-
495 lysosome crosstalk and its role in postnatal intestinal physiology, with implications for understanding the
496 pathophysiology of neonatal malnutrition and related disorders.

497 Autophagy and endocytosis are vesicle-mediated pathways that converge at the lysosome to degrade and
498 recycle intra- and extracellular components. These processes intersect at multiple stages (vesicle
499 formation, trafficking, and fusion) and share several key regulators. Mounting evidence indicates reciprocal
500 dependence between these processes (Birgisdottir and Johansen, 2020; Yim and Mizushima, 2020). Using
501 GFP-LC3 mice, we demonstrated that neonatal ileal samples exhibit increased autophagosome
502 degradation compared to post-weaning counterparts (**Figures 1A–1C and S1C**). Consistently, *Atg16*cKO
503 neonates displayed impaired absorption (**Figures 1H–1J**) and showed reduced expression of crucial
504 endocytic genes characteristic of LREs (**Figures 2B–2F, S2G and S2H**). Moreover, *Atg16*cKO neonatal

505 enterocytes displayed reduced lysosomal size and content (**Figures 2G–2J**), along with downregulation of
506 key lysosomal genes (**Figures S2G and S2H**). These outcomes reveal a functional interplay between
507 autophagy and the endolysosomal system in LREs.

508 Despite these endolysosomal defects, *Atg16*cKO mice reached the post-weaning stage without apparent
509 physiological abnormalities, aside from mild signs of intestinal inflammation (**Figures S2A–S2D**). This
510 observation aligns with findings in mice lacking the lysosomal cation channels Mucolipin-1 and -3 (Mcoln1
511 and Mcoln3), which also exhibit pronounced endolysosomal abnormalities in neonatal enterocytes but
512 develop into phenotypically normal adults (Remis et al., 2014). Together, these results suggest that
513 endolysosomal and autophagic processes primarily affect LREs. Accordingly, once the neonatal period
514 concludes and LREs are replaced by adult enterocytes, the phenotype becomes attenuated or fully
515 resolves. However, further investigations will be needed to assess intestinal physiology and metabolism in
516 adult *Atg16*cKO mice comprehensively.

517 We characterized a significant increase in autophagic activity in LREs as primarily due to the lysosomal
518 degradation of mitochondria, a process known as mitophagy. Indeed, mitophagy-related genes exhibit a
519 higher expression in neonatal ileum compared to post-weaning samples (**Figures 3B–3F**). Correspondingly,
520 neonatal *mito*-QC mice (McWilliams et al., 2016) demonstrated enhanced mitochondrial degradation within
521 the LVs of LREs compared to MECs (**Figures 3H and 3I**). Furthermore, this process was inhibited either
522 by leupeptin treatment (Jiménez-Loygorri et al., 2024) (**Figures 3H and 3I**) or through genetic ablation of
523 autophagy (*Atg16*cKO) (**Figures 3L and 3M**), confirming the dependence of mitochondrial clearance on
524 lysosomal-autophagic activity. Consistent with this, neonatal *Atg16*cKO enterocytes accumulated
525 dysfunctional mitochondrial mass (**Figure 4**). Specifically, these cells showed an increase in the area of
526 damaged mitochondria (class III), whereas healthy mitochondria (class I) exhibited a smaller area but an
527 increased aspect ratio (**Figures 4A–4C**). These differences possibly reflect not only mitophagy blockade
528 but also alterations in mitochondrial dynamics, such as enhanced fusion or reduced fission, which are aimed
529 at preserving oxidative phosphorylation (OXPHOS) capacity (Zemirli et al., 2018). Future studies should
530 investigate the expression of proteins involved in mitochondrial fusion and fission in the *Atg16*cKO model
531 to define better the molecular landscape that integrates mitochondrial dynamics with mitophagy in LREs.

532 After identifying mitochondrial homeostasis defects secondary to impaired endolysosomal function in the
533 *Atg16*cKO model, we next investigated the reverse relationship by directly disrupting mitochondrial function
534 using the *Tfam*cKO model. *Tfam*cKO neonates exhibited severe growth impairment and premature death
535 (**Figures 6A–6C**), and their enterocytes accumulated markedly damaged mitochondria (**Figures 6E–6G and**
536 **S6P**). These mice also reproduced key features of the *Atg16*cKO phenotype, including loss of uptake
537 capacity, reduced lysosomal content, and downregulation of endolysosomal genes (**Figures 6M-6O and**
538 **S7B–S7G**). Interestingly, these lysosomal defects differ from what has been observed in *Tfam*-deficient T
539 and B lymphocytes, where dysfunctional acidic lysosomal compartments are expanded (Baixauli et al.,
540 2015; Iborra-Pernichi et al., 2024). In neonatal enterocytes, however, Tfam deletion results in diminished

541 lysosomal size and content, highlighting that mitochondria–lysosome interactions are highly cell-type
542 specific. Beyond this bidirectional crosstalk, our data raise the possibility of a retrograde signalling
543 mechanism. Mitochondria are increasingly recognized as signalling hubs that influence nuclear
544 transcriptional programs, as shown in immune cells. In LREs, two interconnected processes may be at play:
545 first, endolysosomal-mediated nutrient internalization, which is defective in both *Atg16*cKO and *Tfam*cKO
546 models; and second, mitophagy-driven mitochondrial degradation, which provides retrograde signals to the
547 nucleus. This latter pathway could be essential for controlling the transcriptional networks that govern the
548 metabolic switch (via BLIMP1 and MAFB) and for sustaining lysosomal functionality itself. In this view,
549 lysosomes must degrade mitochondria not only to preserve organelle quality control but also to control the
550 transcriptional reprogramming required for the neonatal-to-adult metabolic transition.

551 At weaning, the mammalian intestine undergoes a shift to extracellular nutrient digestion and adjusts its
552 enzymatic profile to meet the metabolic demands of a carbohydrate-rich solid diet (Henning, 1981). At the
553 same time, LREs are replaced by adult enterocytes lacking large lysosomal vacuoles (Skrzypek et al.,
554 2007). The transcription factors BLIMP1 (PRDM1), along with MAFB and c-MAF (both members of the Maf
555 protein family) have been positioned as central repressors of this switch. Neonatal mice lacking these
556 transcription factors in the intestinal epithelium exhibited impaired nutrient absorption, premature
557 downregulation of neonatal enzymes, and upregulation of adult counterparts, ultimately leading to
558 developmental defects (Bara et al., 2022; Harper et al., 2011; Muncan et al., 2011). Furthermore, our
559 research demonstrated that dysfunctions in autophagic, lysosomal, and mitochondrial processes in LREs
560 —induced by the deletion of *Atg16l1* and *Tfam*— led to a repression of these transcription factors, resulting
561 in similar phenotypes (**Figures 1H, 5, 6H–6N and S7A**).

562 We further analysed the activity of core metabolic pathways in WT, *Atg16*cKO, and *Tfam*cKO neonatal
563 enterocytes, comparing them to MECs (**Figures 5H, 6L, and S5E**). This analysis revealed a moderate
564 reduction in metabolic activity in *Atg16*cKO cells and a more noticeable decline in *Tfam*cKO enterocytes,
565 suggesting a shift toward an adult-like metabolic state. These findings contrast with previous transcriptomic
566 data from neonatal mice lacking MAFB and c-MAF, which reported an upregulation of OXPHOS and fatty
567 acid degradation pathways (Bara et al., 2022). However, that study did not include a direct comparison to
568 adult enterocytes, leaving open the possibility of compensatory mechanisms. In this context, our results
569 may provide a more accurate reflection of the metabolic trajectory during neonatal-to-adult transition and
570 its dependence on the mitochondria-lysosome axis.

571 We have defined the metabolic evolution of enterocytes during neonatal development beyond the genes
572 classically associated with the transcription factors BLIMP1, MAFB, and c-MAF, and established a
573 functional link between this transition and the maintenance of lysosomal and mitochondrial homeostasis.
574 At the same time, our data reinforce the idea that, in enterocytes, genetic programs prevail over the sensing
575 of external cues: despite the neonatal context (milk-based diet, reduced microbiota, and limited immune

576 activation) (Walker, 2013), the repression of these transcription factors leads to inevitable epithelial
577 maturation. Yet, the cellular mechanisms that regulate these genetic pathways still need to be clarified.

578 Reactive oxygen species (ROS) are oxygen-derived molecules that play a crucial role in various cellular
579 processes, including energy production, mitochondrial signalling, and cell differentiation (Sena and
580 Chandel, 2012; Sies et al., 2017). Their intracellular levels are tightly regulated through multiple
581 mechanisms: the mitochondrial electron transport chain constitutes a major source of ROS, while
582 antioxidant enzymes serve as key systems for neutralizing their excess (Murphy, 2008; Sena and Chandel,
583 2012; Sies et al., 2017). In the intestine, ROS have been primarily associated with more differentiated
584 epithelial cells exhibiting higher OXPHOS activity (Rath et al., 2018). However, their role in epithelial
585 maturation during neonatal intestinal development continues to be unexplored.

586 Our results indicate that LREs display a transcriptional signature consistent with elevated antioxidant
587 activity, possibly as a compensatory mechanism to counteract high levels of mitochondrial ROS resulting
588 from hyperactivated OXPHOS (**Figures 7A–7D**). Beyond this homeostatic role, recent studies suggest that
589 this antioxidant signature may also be linked to the repression of transcription factor genes *Blimp1*, *Mafb*,
590 and *c-maf*, and consequently, to the maintenance of LRE identity and function. The antioxidant vitamin
591 ascorbic acid has been shown to increase the expression of Blimp1 in B lymphocytes through the activity
592 of DNA demethylases TET2 and TET3 (Qi et al., 2020). Conversely, treatment with H_2O_2 decreases the
593 expression of *c-maf*, whereas the ROS scavenger N-acetyl cysteine (NAC) can restore *its* levels in human
594 adipose tissue-derived mesenchymal stem cells (Chen et al., 2015).

595 This hypothesis is further supported by the elevated ROS levels and the loss of the antioxidant signature
596 observed in our knockout models (**Figures 4D, 6G, 7E–7J**), as well as by our experiments in which H_2O_2
597 treatment of neonatal WT mice accelerated the metabolic transition of enterocytes (**Figures 7K–7N**).
598 Together, these outcomes suggest that both ROS levels and ROS-regulated genetic programs actively
599 shape epithelial differentiation and metabolic programming in the neonatal intestine (**Figure 7O**). This may
600 represent a physiological mechanism to prevent premature transitions until the tissue is developmentally
601 prepared. In this context, therapeutic strategies aimed at fine-tuning redox homeostasis could offer a
602 powerful approach to supporting neonatal intestinal health.

603 In addition to their role in nutrient absorption, LREs may act as immunometabolic sentinels during the
604 neonatal period, integrating microbial cues and intracellular metabolic status to modulate immune
605 responses. Due to their high endolysosomal activity, LREs could internalise and process luminal antigens,
606 including microbial components, thereby contributing to the development of the intestinal immune system
607 (Massaquoi and Guillemin, 2019). In line with this, our RNA-Seq analysis revealed multiple differentially
608 regulated immune-related pathways (data not shown).

609 Disruption of lysosomal and mitochondrial homeostasis in *Atg16*cKO and *Tfam*cKO mice likely impairs
610 these immune functions, as suggested by the inflammatory status observed in both models (**Figures S2D–**
611 **S2F, S6E, and S6H–S6K**). In fact, mice with autophagy defects also exhibit gut microbiota alterations and

612 immune dysregulation (Larabi et al., 2020). Furthermore, cytosolic mtDNA resulting from mitochondrial
613 damage due to TFAM deficiency has been shown to activate the cGAS–STING inflammatory pathway
614 (Chung et al., 2019), while mitophagy induction, along with improved mitochondrial status, attenuates this
615 response (Jiménez-Loygorri et al., 2024). Additionally, *c-maf* KO mice exhibit changes in intraepithelial
616 lymphocytes and microbiota composition (Cosovanu et al., 2022), suggesting that genetic programs
617 involved in epithelial maturation, affected in our KO models, may be tightly linked to intestinal immune and
618 microbial homeostasis.

619 Given the immunometabolic imbalance observed in *Atg16*cKO and *Tfam*cKO neonates, it is plausible that
620 these models experience alterations in their gut microbiota. These changes may not only reflect enterocytic
621 dysfunction but could also actively contribute to the phenotype by disrupting microbial-derived cues
622 essential for LRE maintenance and programming. Future studies involving microbiota profiling and
623 transplantation will help determine whether restoring a balanced microbial ecosystem can rescue LRE
624 function.

625 Finally, the potential microbiota alterations described above, together with the inflammation and oxidative
626 stress observed in our KO models, suggest parallels with known hallmarks of children's malnutrition
627 disorders. Particularly, *Tfam*cKO mice display a more pronounced phenotype and marked developmental
628 defects, resembling features of Kwashiorkor, a severe form of protein deficiency prevalent in low-income
629 settings (Bhutta et al., 2017; Trehan and Manary, 2015). Notably, the redox imbalance observed in our
630 models resembles clinical features reported in malnourished children, who typically exhibit reduced levels
631 of antioxidants (Bhutta et al., 2017). Accordingly, pilot studies have demonstrated that antioxidant
632 supplementation may provide therapeutic benefit in conditions such as Kwashiorkor (Becker et al., 2005).
633 Moreover, our H_2O_2 treatment experiments, which replicated the epithelial maturation phenotype
634 characterized in our gene-deficient mice, might similarly induce nutritional, microbial, and inflammatory
635 disturbances. Indeed, intestinal tissues from H_2O_2-treated neonates displayed signs of inflammation (data
636 not shown).

637 Collectively, these considerations suggest that malnourished children may also experience premature
638 intestinal maturation and highlight the need for deeper investigation into antioxidant therapies as potential
639 interventions. Furthermore, our KO models may serve as valuable experimental platforms to investigate
640 the mechanisms underlying neonatal malnutrition and to explore interesting avenues for its treatment.
641 Altogether, future studies aimed at restoring LRE mitophagy and metabolism, as well as modulating the
642 redox balance, could yield promising strategies to counteract the devastating consequences of malnutrition-
643 related disorders in early life.

644 In conclusion, our study uncovers novel mechanisms underlying the function and metabolic transition of
645 neonatal enterocytes. We demonstrate that lysosomal and mitochondrial homeostasis is indispensable for
646 efficient nutrient absorption and for sustaining the high metabolic activity required during this energy-
647 demanding stage of life. Further investigation of the mitochondria-lysosome axis in LREs will not only

advance our understanding of neonatal intestinal physiology but also contribute significantly to the development of targeted interventions against childhood malnutrition.

Limitations of the study

This work demonstrates that neonatal intestinal deficits in autophagy and mitochondrial homeostasis lead to endolysosomal dysfunction in enterocytes, impairing development and ultimately triggering inflammation and early lethality. However, since we used *Villin-cre*-based models, where gene deletion occurs in all intestinal epithelial cells, we cannot exclude their contribution to the observed phenotypes. Indeed, we detected altered abundance and morphology of these cells in both *Atg16*cKO (**Figures 1F, 1G, and S2E–S2F**) and *Tfam*cKO mice (**Figures S6G, S6L–S6O**). Previous studies support this interpretation: defects in GCs and PCs are linked to intestinal inflammatory diseases (Hodzic et al., 2017; Wallaeys et al., 2023), and intestinal autophagy loss has been associated with increased oxidative stress in ISCs (Asano et al., 2017), which could partially explain the elevated ROS levels in *Atg16*cKO enterocytes (**Figure 4D**). Similarly, *Tfam* deletion in the adult intestinal epithelium causes ISC loss and lethality (Srivillibhuthur et al., 2018), suggesting that depletion of ISCs may contribute to the early death of neonatal *Tfam*cKO mice, limiting our ability to study mitochondrial function in enterocytes at later developmental stages.

To address these limitations, we plan to develop an LRE-specific tamoxifen-induced conditional knockout (cKO) model to target critical genes specifically in neonatal enterocytes. Although selectively targeting neonatal enterocytes would yield a more precise model, this is hindered by the lack of fully specific promoters and the technical difficulty of isolating and culturing LREs, which are highly sensitive to dissociation-induced cell death. To overcome these challenges, we are also studying *in vitro* systems that recapitulate the properties of LREs and may serve as a platform for future functional validation.

RESOURCE AVAILABILITY

Lead contact

Further information and requests for resources and reagents should be directed to and will be fulfilled by the lead contact, Fernando Martin-Belmonte (fmartin@cbm.csic.es).

Materials availability

This study did not generate new unique reagents.

Data and code availability

RNA-seq Illumina paired-end reads (FASTQ) generated for this study are available at the European Nucleotide Archive (ENA; http://www.ebi.ac.uk/ena/) under the study accession number PRJEB46511.

ACKNOWLEDGMENTS

682 We thank Carmen M. Ruiz-Jarabo for her comments on the manuscript and members of the Martin-
683 Belmonte and Martinez-Martin labs for their support and helpful discussions. This work was supported by
684 MICINN (BFU2017-83243-P; PID2020-120367GB-I00; PID2023-151844OB-I00; RED2022-134927-T),
685 Fondos FEDER investigación (Horizon-MSCA-2022-DN-101119504**)** and Fundación Ramon Areces
686 (CIVP18A3904). HR22-00447 from ¨La Caixa¨, RTI2018-101586-A-I00, PID2021-126298OB-100 to N.M.-
687 M. G.H. and M.I.-P. were supported by FPI fellowships BES-2018-077789 and PRE2019-089076,
688 respectively, funded by the Spanish Ministry of Science and Innovation and the State Research Agency
689 (MCIN/AEI /10.13039/501100011033). D.A.L was supported by FPU and JAE fellowships FPU23/03569
690 and JAEINT_22_01549. L.A was supported by Horizon-MSCA-2022-DN -101119504. I.G.G. was funded
691 by the Medical Research Council, UK (MC_UU_00038/2). We thank Victor Lazaro Morato (currently at IMN-
692 CNM, CSIC, Madrid, Spain) for his contribution to the initial analyses of the general phenotype and
693 mitochondrial status by TEM in the *Tfam*cKO model. We acknowledge Michel Bagnat (Duke University,
694 USA) for the generous donation of mCherry plasmid, and Juan M. Serrador, Catalina Grabowski and
695 Dionisio Ureña (CBM), for their essential contribution to the protocol for the growth and purification of
696 mCherry plasmid. We are thankful to the Animal, Flow Cytometry, Advanced Optical Microscopy, and
697 Electron microscopy facilities at the CBM, as well as the Histology Service at the Centro Nacional de
698 Biotecnologia (CNB, CSIC, Madrid, Spain), for their excellent technical support. We acknowledge the
699 Centro de Análisis Genómico (CNAG-CRG, Barcelona, Spain) for the RNA sequencing, and to
700 Biocomputational Analysis Core Facility at the CBM, specially to Sandra González de la Fuente, for the
701 NGS data analysis and plotting. We thank the computational resources and support provided by the Centro
702 de Computación Científica at Universidad Autónoma de Madrid (CCC-UAM).

703 Certain Figures were inspired by or adapted from previously published sources, some of which are licensed
704 under Creative Commons (CC BY 4.0) (https://creativecommons.org/licenses/by/4.0/). While every effort
705 has been made to credit original sources, any omissions are unintentional and will be corrected in future
706 revisions if identified. Some figures were created with BioRender.com.

707

708 **DECLARATION OF INTERESTS**

709 The authors declare no competing interests.

710

711 **FIGURE TITLES AND LEGENDS**

712 **Figure 1. High Autophagic Activity of LREs Is Required for Nutrient Absorption**

713 **(A and B)** Assessment of autophagic flux and protein absorption along the small intestine of GFP-LC3 mice
714 during postnatal development. GFP-LC3 mice at postnatal days (P) 1, 7, 14, and 21 were orally gavaged
715 with mCherry and sacrificed 3 hours later (n = 3) (A). Proximal and distal intestinal segments were harvested
716 (A), and epithelial cell lysates analysed by immunoblotting for mCherry and GFP-LC3 isoforms (B). The

717 representative western blot in (B) distinguishes cytosolic LC3-I, membrane-bound LC3-II, and cleaved "free
718 GFP," a marker of autolysosomal degradation. The pink rectangle highlights mCherry and free GFP in
719 distal-P7, indicating maximal protein uptake and autophagic degradation. USP7, loading control. Figure 1A
720 includes images adapted from Birchenough et al. (2023) (CC BY 4.0) and Zhao et al. (2021), and the GFP-
721 LC3 isoforms scheme is based on Ni et al. (2011).

722 **(C)** Quantification of mCherry and free GFP levels in lysates of ileal epithelial cells from P7 (n = 4) and P21
723 (n = 5) GFP-LC3 mice. Data derived from Figure S1C.

724 **(D and E)** Generation and validation of *Atg16l1* intestinal knockout (*Atg16*cKO) mice. Ileal epithelial cell
725 lysates from WT and *Atg16*cKO P14 mice were immunoblotted for ATG16L1, LC3, and P62 (D). (E)
726 Quantification of ATG16L1 (n = 5,6) and P62 (n = 6,7), and LC3-II/LC3-I ratio (n = 17). In ATG16L1 and
727 P62 graphs, data relative to WT.

728 **(F and G)** Ileal architecture in *Atg16*cKO neonates. Periodic acid-Schiff (PAS)-haematoxylin staining of P14
729 ileal sections from WT and *Atg16*cKO mice (F) shows villus shortening (double red arrow) and a decrease
730 in goblet cells (PAS+, arrowheads) in *Atg16*cKO sections (n = 3). L, lumen; scale bar, 100 µm. (G)
731 Quantification of villus length and goblet cells per villus. Dots represent individual villi (n = 30 villi from 3
732 mice; 10 villi per mouse).

733 **(H)** Confocal analysis of Rd-dextran uptake in ileal *Atg16*cKO enterocytes. WT and *Atg16*cKO neonates at
734 P7 (early) and P14 (late), and post-weaning (P21–30) WT mice were gavaged with rhodamine B–dextran
735 (Rd-dext, red) 16 hours prior to sacrifice (n = 3). Ileal sections labelled with β-catenin (βcat, white) and DAPI
736 for DNA (blue). Dashed-line squares indicate magnified areas. Arrows point to lysosomal vacuoles;
737 arrowheads, apical endosomes. L, lumen. Scale bars: 10 µm (main); 5 µm (insets). Dot plot shows the
738 quantification of Rd-dextran intensity (integrated density) in the apical and basal regions of enterocytes.
739 Dots represent individual enterocytes (n = 25–40).

740 **(I and J)** *Atg16*cKO mice show impaired mCherry absorption. P14 mice were gavaged with mCherry and
741 ileal epithelial cell lysates collected 16 hours later for immunoblotting (I). Actin, loading control. (J)
742 Quantification of mCherry signal, normalised to WT (n = 9,11).

743 In (C, E, J), dots represent individual mice and charts depict mean + SEM. In (G, H), dot plots show mean
744 ± SEM (black lines).

745 (C, E, G): Student's t-test (mCherry, ATG16L1, P62, villus length) and Mann–Whitney test (free GFP, LC3
746 ratio, goblet cells/villus). (J): Mann–Whitney test. (H): Kruskal–Wallis test; only statistically significant
747 comparisons between WT and *Atg16*cKO are shown within each region (apical or basal). *$p < 0.05$; ****$p <$
748 0.0001.

749 **See also Figure S1.**

750

751 **Figure 2. Loss of Autophagy Compromises the Endolysosomal System in LREs**

752 **(A)** Reverse transcription quantitative polymerase chain reaction (RT-qPCR) analysis of *Dab2*, *Mcoln3*,
753 *Lamp2* and *Ctsl1* genes in epithelial cells from proximal and distal samples of small intestines from WT
754 mice at the indicated time points (n = 3). Data relative to values of proximal region of small gut from
755 embryonic day (E) 18.5 mice embryos, and presented as $\log_{10}$ fold changes ($\log_{10}$FC).

756 **(B)** RT-qPCR of *Dab2*, *Mcoln3*, and *Lamp2* in ileal epithelial cells from WT and *Atg16*cKO mice at P7 and
757 P14. Sample sizes: *Dab2* and *Lamp2* (n = 10,6,6,6), *Mcoln3* (n = 9,8,6,6).

758 **(C and D)** Immunoblot analysis of Dab2 protein in ileal epithelial cell lysates from WT and *Atg16*cKO mice
759 at P7 and P14 (C). Actin, loading control. (D) Quantification of Dab2 protein levels (n = 6,8,9,14).

760 **(E and F)** Confocal images of ileal sections from WT and *Atg16*cKO mice at P7 and P14 (n = 3) labelled
761 with anti-Dab2 (green), β-catenin (magenta), and DAPI (blue) (E). Arrowheads mark apical Dab2
762 localization. (F) Violin plot quantifying apical Dab2 intensity (integrated density) of P14 sections, normalised
763 to epithelial area (n = 10,8; 2–4 images per mouse).

764 **(G and H)** Lysosomal occupation and content in WT and *Atg16*cKO mice at P7 and P14, and in post-
765 weaning (P21–30) WT mice. Confocal sections labelled with anti-LAMP1 (green), β-catenin (white), and
766 DAPI (blue) (G). Arrows: endolysosomal system in WT LREs; arrowheads: reduced $LAMP1^+$ vesicles in
767 *Atg16*cKO and post-weaning enterocytes. (H) Dot plots quantify the percentage of $LAMP1^+$ area and
768 LAMP1 intensity (integrated density) within apical and basal regions of interest (ROIs) (n = 26–36).

769 **(I and J)** Immunoblot analysis of LAMP1 protein in ileal epithelial cell lysates from WT and *Atg16*cKO mice
770 at P14 (I). Actin, loading control. (J) Quantification of LAMP1 protein levels (n = 10,13).

771 In (E, F), dashed-line squares indicate magnified areas; L, lumen. Scale bars: 10 μm (main); 5 μm (insets).

772 Dots represent individual mice (B, D, J) or images (F) or cells (H). In (B, D, F, J), data relative to WT values.
773 Graphs of (A) represent mean + SD; graphs of (B, D, J), mean + SEM; violin plot of (F), median (thick line)
774 and interquartile range (IQR, thin lines); dot plots of (H), mean ± SEM (black lines).

775 Statistical analyses: Kruskal–Wallis test (A [*Dab2*, *Mcoln3*], H), two-way ANOVA (A: *Lamp2*, *Ctsl1*),
776 Student's *t*-test (B, D, J), Mann–Whitney test (F). In (A), only the most relevant statistically significant
777 comparisons are shown. In (H), only statistically significant comparisons are displayed within each group
778 (apical or basal). *$p < 0.05$, **$p < 0.01$, ***$p < 0.001$, ****$p < 0.0001$.

779 **See also Figure S2.**

780

781 **Figure 3. LREs Present High Levels of Mitophagy**

782 **(A)** Workflow of RNA sequencing (RNA-seq) analysis comparing LREs from P7 GFP-LC3 mice gavaged
783 with rhodamine B–dextran (16 hours prior) to MECs from post-weaning (P42) GFP-LC3 mice. Enterocytes

784 were isolated from ileal samples by fluorescence-activated cell sorting (FACS) and used for RNA-seq. See
785 Figure S4A for gating strategy. Scheme includes images adapted from Treuting et al. (2018) and Park et
786 al. (2019).

787 **(B)** Volcano plot of differentially expressed genes (DEGs) between LREs and MECs. Each point represents
788 a gene, plotted by $\log_2$ fold change (x-axis) and $-\log_{10}$ adjusted p-value (padj) (y-axis). DEGs (n = 1537;
789 shown in steel blue) were defined as genes with padj < 0.05 and $|\log_2 FC| > 1$. Upregulated genes associated
790 with endocytosis (amber), lysosome (purple), and mitophagy (red) are highlighted. Dashed lines indicate
791 significance (padj < 0.05) and fold-change thresholds (±1). Genes with $-\log_{10}(\text{padj}) > 60$ are not shown.

792 **(C)** Bubble plot of selected Gene Ontology (GO) terms from over-representation analysis (ORA) of the
793 differential gene expression data from the LREs vs MECs. Note the presence of regulation of autophagy,
794 positive regulation of autophagy of mitochondrion and mitochondrial outer membrane pathways. The x-axis
795 represents the z-score, bubble size reflects the number of associated genes, and bubble colour indicates
796 statistical significance (adjusted p-value), with a red-to-blue gradient from most to least significant. GO
797 terms are grouped into three categories: BP, biological process; CC, cellular component; MF, molecular
798 function.

799 **(D)** Enrichment plots of lysosome organization and mitochondrial outer membrane gene sets from gene set
800 enrichment analysis (GSEA) comparing LREs and MECs**.** The top panel shows the Enrichment Score (ES)
801 across ranked genes, with the peak indicating maximum enrichment. The middle panel marks gene
802 positions in the ranked list. The bottom colour bar reflects gene correlation with phenotype (red: positive,
803 blue: negative).

804 **(E)** RT-qPCR analysis of *Bnip3*, *Prkn*, and *Pink1* genes in ileal epithelial cells from WT mice at indicated
805 time points (n = 3). Values are expressed as $\log_{10}$ fold change relative to E18.5 embryonic levels.

806 **(F)** Confocal images of ileal sections from WT mice at P7 (LREs) and P21–30 (MECs), labelled with anti-
807 Parkin (green) and DAPI (blue). Left: violin plot of Parkin intensity (integrated density) normalised to
808 epithelial area.

809 **(G)** Schematic of the *mito*-QC reporter mouse model. Mitochondria are tagged with the chimeric protein
810 mCherry-GFP-FIS1$^{101–152}$. Upon mitophagy, mitochondria are delivered to the lysosome where acidic pH
811 quenches GFP but not mCherry, allowing identification of mitolysosomes as mCherry-only puncta.

812 **(H)** Confocal images of ileal sections from *mito*-QC mice at P7 (LREs) (± leupeptin, LP) and P21–30
813 (MECs). Samples stained with anti-LAMP1 (white) and DAPI (blue). Arrows indicate enlarged, blocked
814 lysosomes with red-only mitochondrial aggregates in LREs+LP; arrowheads point to LAMP1$^+$/mCherry$^+$
815 puncta lacking GFP, validating the *mito*-QC model.

816 **(I)** Violin plot of lysosomal mCherry intensity normalised to cellular mCherry intensity from (H), based on
817 integrated density measurements.

818 **(J)** RT-qPCR of *Bnip3* and *Prkn* in ileal epithelial cells from WT and *Atg16*cKO mice at P14. Dots represent
819 individual mice. Sample sizes: *Bnip3* (n = 6, 6), *Prkn* (n = 5, 6).

820 **(K)** Confocal images of ileal sections from WT and *Atg16*cKO mice at P14 stained with anti-Parkin (green)
821 and DAPI. Left: violin plot of Parkin intensity (Integrated Density) normalised to epithelial area.

822 **(L)** Confocal images of ileal sections from *mQ*-WT and *mQ-Atg16*cKO mice at P14 (n = 3), labelled with
823 anti-LAMP1 (white) and DAPI (blue).

824 **(M)** Violin plot of lysosomal mCherry intensity normalised to cellular mCherry intensity from (L), based on
825 integrated density measurements (n = 12–11; 3–4 images per mouse).

826 In images of (F, H, K, L), L, lumen. Scale bars: 5 µm. Images of (H, L) deconvolved with Huygens software.

827 In (A–I) and (K–M), n = 3; in (F, I, K), n = 9 images from 3 mice (3 images per mouse). In graphs of (F, I),
828 data relative to LREs values; in (J, K, M), relative to WT values. In (E), graph represents mean + SD; in (J),
829 mean + SEM. In violin plots of (F, I, K, M), the median (thick line) and IQR (thin lines) are shown and dots
830 represent individual images.

831 Statistical analyses: Kruskal–Wallis test (E: *Bnip3*), one-way ANOVA (E [*Prkn*, *Pink1*], I), Student's *t*-test
832 (F, J, K, M). *p< 0.05, **p< 0.01, ***p < 0.001.

833 **See also Figure S4.**

834

835 **Figure 4. *Atg16*cKO Neonatal Mice Exhibit Increased Mitochondrial Damage and Oxidative Stress in**
836 **Enterocytes**

837 **(A)** Representative transmission electron microscopy (TEM) micrographs of ileal sections from WT and
838 *Atg16*cKO mice at P14 (n = 3). Note the reduction of the endolysosomal system and the absence of
839 lysosomal vacuole in the *Atg16*cKO enterocytes. Dashed boxes indicate magnified areas. N, nucleus; LV,
840 lysosomal vacuole; AEC, apical endosomal complex; L, lumen. Asterisks indicate damaged mitochondria.
841 Scale bars: 2 µm (main); 500 nm (insets).

842 **(B)** TEM-based classification of mitochondria into three categories based on electron density and cristae
843 integrity: Class I (normal), Class II (partially affected), and Class III (damaged). Classification based on
844 Moschandrea et al. (2023). See Electron Microscopy Section in Methods. Scale bar: 500 nm.

845 **(C)** Distribution of mitochondrial integrity classes in *Atg16*cKO neonatal enterocytes. Quantification of the
846 number, percentage, area and aspect ratio (long axis / short axis) of each mitochondria class in (A), as
847 defined in (B). In count and percentage graphs, dots represent individual enterocytes; in area and aspect
848 ratio graphs, dots represent individual mitochondria. Sample sizes are indicated in Table S1.

849 **(D)** Flow cytometry analysis of mitochondrial status of *Atg16*cKO neonatal enterocytes. Graphs show
850 relative mean fluorescence intensity (MFI) for Mitotracker Green (mitochondrial mass, MM), Mitotracker

851 Red CMXROS (mitochondrial membrane potential, MMP) and CM-H_2DCFDA (ROS) in ileal EpCAM$^+$CD24$^-$
852 cKit$^-$ cells from WT and *Atg16*cKO mice at P14. See Figure S3 for gating strategy. Dots represent individual
853 mice (MM, n = 23,17; MMP, n = 10,9; ROS, n = 19,13).

854 In (C), dot plots represent mean ± SEM (black lines). In (D), bar chart show mean + SEM.

855 Statistics analyses: Mann–Whitney test (C, D [MM]), Student's *t*-test (D: MMP, ROS). *p < 0.05, **p < 0.01,
856 ***p < 0.001, ****p < 0.0001.

857 **See also Figure S3 and Table S1.**

858

859 **Figure 5. Autophagy Deficiency Causes Premature Metabolic Transition in LREs**

860 **(A)** RT-qPCR analysis of transcription factor (*Mafb*, *c-maf*, *Blimp1*), neonatal (*Ass1*, *Glb1*) and adult (*Treh*,
861 *Sis*, *Arg2*) enzyme genes in ileal epithelial cells from WT and *Atg16*cKO mice at late neonatal stage (P14)
862 and from WT mice at post-weaning stage (P21–30). Sample sizes: *Mafb* (n = 8, 9, 3), *c-maf* (n = 8, 11, 3),
863 *Blimp1* (n = 11, 9, 4), neonatal enzymes (n = 6, 5, 4), *Treh* (n = 5, 3, 4), *Sis* (n = 5, 5, 4), *Arg2* (n = 5, 6, 4).

864 **(B)** Confocal images of ileal sections from WT and *Atg16*cKO mice at P14 (n = 5), and from post-weaning
865 (P21–30) WT mice (n = 2–3), labelled with anti-MAFB (green, top) or anti-BLIMP1 (green, bottom), and with
866 phalloidin for F-actin (magenta) and DAPI (blue). Arrowheads point to nuclear localization of MAFB and
867 BLIMP1 in WT LREs.

868 **(C)** Violin plot of nuclear MAFB (n = 20, 21, 11) and BLIMP1 (n = 21, 16, 9) intensity (integrated density) in
869 (B), normalised to epithelial nuclear area.

870 **(D)** Confocal images of ileal sections from WT and *Atg16*cKO mice at P14, labelled with anti-ASS1 (green,
871 top) (n = 3) or anti-TREH (green, bottom) (n = 5), anti-E-cadherin (Ecad, magenta), and DAPI (blue).

872 **(E)** Violin plots of ASS1 (top; n = 12, 10) and TREH (bottom; n = 15,16) intensity (integrated density) in (D),
873 normalised to epithelial area.

874 **(F)** Western blot of TREH protein from ileal epithelial cells of WT and *Atg16*cKO mice at P14. USP7, loading
875 control.

876 **(G)** Bar chart quantifying TREH protein levels from (F) (n = 5, 4).

877 **(H)** Met-Flow profiling of ileal EpCAM$^+$CD24$^-$ cells from WT (n = 10–13) and *Atg16*cKO (n = 7–9) mice at
878 P14, and from post-weaning (P21–30) WT mice (n = 8). Bubble colour and size reflect group means for
879 each marker. See Figure S3 for the gating strategy and Table S2 for statistical significance.

880 In (B, D), dashed boxes indicate magnified areas; L, lumen. Scale bars: 10 μm (main); 5 μm (insets).

881 In (A, C, E, G, H), data relative to WT P14 values. In (A, G), graphs show mean + SEM and dots represent
882 individual mice. In (C, E), violin plots depict the median (thick line) and IQR (thin lines) and dots are
883 individual images (2–5 images per mouse, 2–5 mice per group).

884 Statistical analyses: one-way ANOVA (A, C [MAFB], H), Kruskal–Wallis test (C: BLIMP1), Mann–Whitney
885 test (E), Student's t test (G). *p < 0.05, **p < 0.01, ***p < 0.001, ****p < 0.0001.

886 **See also Figures S3 and S5, and Table S2.**

887

888 **Figure 6. *Tfam*cKO Neonates Recapitulate Endolysosomal and Metabolic Defects Observed in**
889 ***Atg16*cKO Enterocytes, and Exhibit Weight Loss and Early Lethality**

890 **(A)** Representative images of WT and *Tfam*cKO mice at postnatal day 14 (P14).

891 **(B)** Kaplan–Meier survival curves of WT and *Tfam*cKO mice. Animals were euthanized if they failed to gain
892 weight for two consecutive days or exhibited marked weight loss beginning at P9.

893 **(C)** Relative body weight of WT and *Tfam*cKO mice at P8, P10, P12, and P14, expressed as percentage.
894 Sample sizes are indicated at the bottom of the graph.

895 **(D)** RT-qPCR analysis of *Tfam* mRNA in ileal epithelial cells from WT and *Tfam*cKO mice at P10 and P14
896 (n = 12,12,12,10).

897 **(E)** *Tfam*cKO neonatal enterocytes show damaged mitochondria. TEM micrographs of ileal sections from
898 WT (n = 3) and *Tfam*cKO (n = 4) mice at P10 and P14. Asterisks indicate damaged mitochondria. Scale
899 bar, 1 µm.

900 **(F)** Quantification of mitochondrial classes in (E), as defined in Figure 4B. Dots represent individual
901 enterocytes. Sample sizes are indicated in Table S1.

902 **(G)** Flow cytometry analysis of mitochondrial status of *Tfam*cKO neonatal enterocytes. Bar charts show
903 relative MFI for Mitotracker Green (mitochondrial mass, MM), Mitotracker Red CMXROS (mitochondrial
904 membrane potential, MMP) and CM-H_2DCFDA (ROS) in ileal EpCAM$^+$CD24$^-$cKit$^-$ cells from WT and
905 *Tfam*cKO mice at P10 and P14. Sample sizes: MM (n = 5, 5, 8, 14), MMP (n = 3, 4, 10, 13), ROS (n = 9, 6,
906 10, 9). See Figure S3 for gating strategy.

907 **(H)** Confocal images of ileal sections from WT and *Tfam*cKO mice at P14 (n = 3–4), stained with anti-MAFB
908 (green, top) or anti-BLIMP1 (green, bottom), phalloidin (magenta), and DAPI (blue). Arrowheads mark
909 nuclear localization of MAFB and BLIMP1 in WT LREs.

910 **(I)** Violin plots quantifying nuclear MAFB (top; n = 15, 10) and BLIMP1 (bottom; n = 16, 16) intensity in (H),
911 normalised to epithelial nuclear area.

912 **(J)** Confocal images of ileal sections from WT and *Tfam*cKO mice at P14 (n = 3–4). Top: labelled with anti-
913 ASS1 (green), anti-E-cadherin (Ecad, magenta), and DAPI (blue). Bottom: labelled with anti-TREH (green)
914 and anti-Ecad (magenta).

915 **(K)** Violin plots quantifying ASS1 (top; n = 14, 16) and apical TREH (bottom; n = 9, 10) intensity in (J),
916 normalised to epithelial area.

917 **(L)** Met-Flow profiling of ileal $EpCAM^{+}CD24^{-}$ cells from WT (n = 6) and *Tfam*cKO (n = 5) mice at P14. Bubble
918 colour and size reflect group means for each marker. See Figure S3 for the gating strategy and Table S2
919 for statistical significance.

920 **(M)** Confocal images of ileal sections from WT (n = 4) and *Tfam*cKO (n = 3) mice at P14 gavaged with
921 rhodamine B–dextran (Rd-dext, red) 3 hours before sacrifice. Sections were stained with anti-LAMP1
922 (green), anti-β-catenin (white), and DAPI (blue). Arrow: endolysosomal system in WT LREs; arrowhead:
923 reduced $LAMP1^{+}$ vesicles in *Tfam*cKO enterocytes. Images deconvolved with Huygens software.

924 **(N)** Violin plot quantifying Rd-dextran uptake (integrated density) in (M), normalised to epithelial area (n =
925 11, 7).

926 **(O)** Quantification of lysosomal occupation and content in (M). Dot plots show the $LAMP1^{+}$ area as a
927 percentage of cell area (n = 167, 145) and LAMP1 intensity (integrated density) per enterocyte (n = 148,
928 139).

929 In (D–O), mice aged P9–11 and P13–15 were grouped as “P10” and “P14,” respectively.

930 In (H, J, M), dashed boxes indicate magnified areas; L, lumen. Scale bars: 10 μm (main); 5 μm (insets).

931 In (C, D, G, I, K, L, N), data relative to WT values. In (C, D, G), graphs depict mean + SEM and dots
932 represent individual mice. In (F, O), dot plots show mean ± SEM (red lines) and dots represent individual
933 enterocytes. In (I, K, N), violin plots show median (thick line) and IQR (thin lines) and dots represent
934 individual images (2–4 per mouse).

935 Statistical analyses: Gehan–Breslow–Wilcoxon test (B), Student’s *t*-test (C, D, F [P14 Class III only], G, K,
936 L, N), Mann–Whitney test (F [except P14 Class III], I, O). *$p < 0.05$, **$p < 0.01$, ***$p < 0.001$, ****$p < 0.0001$.

937 **See also Figures S3, S6 and S7, and Tables S1 and S2.**

938

939 **Figure 7. High Antioxidant Activity in LREs Regulates the Timing of Metabolic Transition**

940 **A)** Bar chart showing the relative mean fluorescence intensity (MFI) of MitoSOX (mitochondrial ROS) and
941 CM-H_2DCFDA (total ROS) in ileal $EpCAM^{+}CD24^{-}$ cells from WT mice at P7 (LREs) and P21–30 (MECs) (n
942 = 4). Data relative to LREs values. See Figure S3 for gating strategy.

943 **(B)** Bubble plot and list of ROS-related GO terms from over-representation analysis (ORA) of DEGs
944 between LREs and MECs. The x-axis represents the z-score, the y-axis shows the significance as –

945 $\log_{10}$(adjusted p-value), bubble size reflects the number of associated genes, and colors indicate GO
946 categories (BP, biological process; CC, cellular component; MF, molecular function).

947 **(C)** GSEA enrichment plot of antioxidant activity gene set (LREs vs MECs).

948 **(D)** RT-qPCR analysis of *Gpx3* and *Cat* genes in ileal epithelial cells from WT mice at the indicated time
949 points (n = 3). Values are expressed as $\log_{10}$ fold change relative to E18.5 embryonic levels.

950 **(E)** RT-qPCR analysis of *Gpx3* and *Cat* genes in ileal epithelial cells from WT and *Atg16*cKO mice at P14
951 (n = 6).

952 **(F)** RT-qPCR analysis of *Gpx3* (n = 7, 5) and *Cat* (n = 5, 7) in ileal epithelial cells from WT and *Tfam*cKO
953 mice at P14.

954 **(G)** Confocal images of ileal sections from WT and *Atg16*cKO mice at P14 (n = 3), stained with anti-GPX3
955 (green), anti-E-cadherin (Ecad, magenta), and DAPI (blue).

956 **(H)** Violin plot of GPX3 intensity from (G), normalised to epithelial area (n = 12, 9).

957 **(I)** Confocal images of ileal sections from WT and *Tfam*cKO mice at P14 (n = 4), labelled as in (F).

958 **(J)** Violin plot of GPX3 intensity from (H), normalised to epithelial area (n = 16).

959 **(K)** RT-qPCR analysis of transcription factor (*Mafb*, *c-maf*, *Blimp1*), neonatal (*Ass1*, *Glb1*) and adult (*Treh*,
960 *Arg2*) enzyme genes in ileal epithelial cells from control and H_2O_2 treated mice at P12. Sample sizes: *Mafb*
961 (n = 7, 6), *c-maf* (n = 7, 6), *Blimp1* (n = 7, 7), neonatal enzymes (n = 7, 7), *Treh* (n = 5, 6), *Arg2* (n = 6, 6).

962 **(L)** Confocal images of ileal sections from control (n = 4) and H_2O_2-treated (n = 4–5) mice at P12, stained
963 with anti-BLIMP1 (green, left) or anti-ASS1 (green, centre) or anti-TREH (green, right), and DAPI (blue). L,
964 lumen. Scale bars, 10 μm.

965 **(M)** Violin plots of BLIMP1, ASS1 and TREH intensity (integrated density) from (L). BLIMP1 data were
966 normalised to epithelial nuclear area; ASS1 and TREH data, to epithelial area. Sample sizes: BLIMP1 (n =
967 12, 15), ASS1 (n = 12, 16), TREH (n = 13, 12).

968 **(N)** Flow cytometry analysis of BLIMP1 (n = 7, 7) and ASS1 (n = 6, 7) in control and H_2O_2-treated mice at
969 P12. Bar charts show relative median fluorescent intensity of BLIMP1 and ASS1 in ileal $EpCAM^+CD24^-cKit^-$
970 cells. See Figure S3 for gating strategy.

971 **(O)** Working model: In *Atg16*cKO and *Tfam*cKO neonatal enterocytes, mitochondrial dysfunction and
972 reduced antioxidant responses elevate ROS levels, which repress *Blimp1* and *Mafb* expression and drive
973 premature metabolic transition. Enterocyte's design inspired by Fujita et al. (1990). Figure created with
974 BioRender.com.

975 In (G, I), dashed boxes indicate magnified areas; L, lumen. Scale bars: 10 μm (main); 5 μm (insets).

976 In (E, F, H, J), data relative to WT values; in (K, M, N), relative to control values. In (A, E, F, K, N), graphs
977 represent mean + SEM and dots represent individual mice; in (C), mean + SD. In (H, J, M), violin plots show
978 median (thick line) and IQR (thin lines) and dots represent individual images (2–4 per mouse, 3–5 mice per
979 group).

980 Statistical analyses: Student's t test (A, E, F, H, K, M [ASS1], N), one-way ANOVA (D), Mann–Whitney test
981 (J, M [BLIMP1, TREH]). *p < 0.05, **p < 0.01, ***p < 0.001, ****p < 0.0001.

982 **See also Figure S3.**

983

984 **SUPPLEMENTAL INFORMATION**

985 **Figure S1. Characterization of LREs in the Neonatal Mouse Ileum**
986 ***Related to Figures 1 and 2***

987 (**A**) Representative TEM image of LREs from the distal small intestine of a P7 mice (n = 3). The profile of
988 an LRE is outlined by a dashed line. Dashed boxes indicate magnified areas. N, nucleus; LV, lysosomal
989 vacuole; AEC, apical endosomal complex; e, endosome; mvb, multivesicular body; L, lumen. Scale bars:
990 5 μm (main); 2 μm (insets).

991 (**B**) Confocal microscopy images of ileal sections from P7 mice (n = 3), stained with anti-LAMP1 (green),
992 anti-Dab2 (magenta), anti-β-catenin (white), and DAPI (cyan). Dashed boxes highlight magnified areas.
993 Arrows indicate the endolysosomal system; arrowheads point to apical Dab2 localization. Scale bars: 20 μm
994 (main); 10 μm (first magnification); 5 μm (second magnification).

995 (**C**) Western blot of mCherry and GFP-LC3 isoforms in ileal epithelial cells from GFP-LC3 mice at P7 and
996 P21, gavaged with mCherry 3 hours before sacrifice. USP7, loading control.

997 (**D**) Sequential fluorescent dextran uptake assay. P7 mice were gavaged with Alexa 647-dextran (FR-dext,
998 green), followed by rhodamine B–dextran (Rd-dext, red) 3 hours later. Mice were sacrificed at 4 and 8 hours
999 post-initial gavage to assess uptake via confocal microscopy (n = 3). Arrows point to lysosomal vacuoles
1000 containing both dextrans at 8 hours. Arrowheads indicate endosomes. Scale bars: 5 μm (main); 2 μm
1001 (insets).

1002

1003 **Figure S2. Phenotype of *Atg16*cKO Mice**
1004 ***Related to Figures 1 and 2***

1005 **(A)** Relative body weight of WT and *Atg16*cKO mice at postnatal days P7, P14, and P30. Sample sizes are
1006 indicated in the graph.

1007 **(B)** Representative images of intestines from WT and *Atg16*cKO mice at the post-weaning stage (P30).

1008 **(C)** Quantification of intestinal lengths shown in (B). Bar graphs show the relative lengths of the small
1009 intestine (SI) and the colon–rectum (CR) segments (n = 7, 9).

1010 **(D)** Representative histological images of ileum and colon sections from WT and *Atg16*cKO post-weaning
1011 (P30) mice (n = 3). Ileal sections are stained with periodic acid-Schiff (PAS) and haematoxylin; colon
1012 sections are stained with haematoxylin and eosin (H&E). Asterisks denote oedema in *Atg16*cKO ileum;
1013 arrowheads indicate goblet cells. Scale bars: 200 μm (ileum), 400 μm (colon).

1014 **(E and F)** Flow cytometry analysis of immune and epithelial cell populations in the ileum of WT and
1015 *Atg16*cKO mice at P14 (E) and P30 (F). Left: B lymphocytes (LB) and T-helper lymphocytes (LTh)
1016 percentages. Centre: Innate immune cells (IIC) and intestinal epithelial cells (IEC) percentages. Right:
1017 Enterocyte and enterocytic progenitors (EC), goblet cell (GC), Paneth cell (PC), and enteroendocrine cell
1018 (EEC) percentages. See Figure S3 for gating strategy. (E): Left, n = 17,8–11; Centre, n = 22,16–17; Right,
1019 n = 15,12–13. (F): n = 6–7, 9–10.

1020 **(G)** RT-qPCR analysis of *Dab2* (n = 10,6,6,5), *Mcoln3* (n = 9,8,6,5), and *Lamp2* (n = 10,6,6,6) in epithelial
1021 cells from the proximal small intestine of WT and *Atg16*cKO mice at P7 and P14.

1022 **(H)** RT-qPCR analysis of *Amn* (n = 6,5), *Mamdc4* (n = 9,10), and *Ctsl1* (n = 9,11) in ileal epithelial cells
1023 from WT and *Atg16*cKO mice at P14.

1024 In (A, C, G, H), graphs represent mean + SEM. In (E, F), violin plots depict median (thick line) and
1025 interquartile range (IQR, thin lines). In all graphs, data relative to WT values, dots represent individual mice
1026 and Student's t test was conducted. *$p < 0.05$, **$p < 0.01$, ***$p < 0.001$, ****$p < 0.0001$.

1027

1028 **Figure S3. Gating Strategies Used for Cell Population Characterization by Flow Cytometry**
1029 ***Related to Figures 4–7, S2 and S4–S6***

1030 Biopool is the combination of immune cell markers anti-CD11c, anti-CD3e, anti-CD11b, anti-CD19, and
1031 anti-CD45.2. The strategy for selecting IEC subtypes is based on Asano et al. (2017). GD, ghost dye; LT_h,
1032 T-helper lymphocytes; LB, B lymphocytes; IIC, innate immune cells; IEC, intestinal epithelial cells; EEC,
1033 enteroendocrine cells; PC, Paneth cells; EC, enterocytes and enterocytic progenitors; GC, goblet cells.

1034

1035 **Figure S4. RNA-seq Analysis Comparing Gene Expression of LREs and MECs**
1036 ***Related to Figure 3***

1037 **(A)** FACS gating strategy used to isolate LREs and MECs from GFP-LC3 mice at P7 (gavaged with Rd-
1038 dextran, 16 hours) and P42, respectively, for RNA-seq analysis. Single-living $EpCAM^{+}CD24^{-}Biopool^{-}$ cells
1039 were gated. For LREs, $Dextran^{+}GFP^{high}$ cells were selected.

1040 **(B)** Heatmap with hierarchical clustering of differentially expressed genes (DEGs) with q-value < 0.05
1041 reveals distinct expression patterns between LREs and MECs. Each row represents a single gene and

1042 each column represents a condition sample. Each sub-column represents an individual sample (3 samples
1043 per group). Gene expression intensities were log_2-transformed and visualized as a colour gradient from
1044 yellow to light blue, representing the shift from downregulation to upregulation, as indicated in the key.

1045 **(C)** Principal component analysis (PCA) plotting for 2 groups based on normalised overall transcriptomic
1046 reads. The PCA figure represents a two-dimensional scatterplot of the first two principal components of the
1047 RNA-Seq data. Analyses in panels (B) and (C) show that replicates of the same cell population are more
1048 similar to each other than to replicates from a different population.

1049 (**D**) Bubble plot of selected Kyoto Encyclopaedia of Genes and Genomes (KEGG) pathways from over-
1050 representation analysis (ORA) of the differential gene expression data from the LREs vs MECs. The x-axis
1051 represents the z-score, the y-axis shows the significance as –log10(adjusted p-value), bubble size reflects
1052 the number of associated genes, and colours indicate KEGG pathway categories.

1053 **(E)** RT-qPCR validation of *Ctsl1* expression in LREs and MECs from WT mice at P7 (gavaged with Rd-
1054 dextran, 16 hours) and P42, respectively. FACS was used for cell sorting, selecting single-living
1055 $EpCAM^+CD24^-Biopool^-$ cells, with $Dextran^+$ cells further gated for LREs. In LREs, each dot represents one
1056 of three pooled samples (n = 3), each composed of multiple mice; in MECs, each dot corresponds to an
1057 individual mouse (n = 3). Data relative to LREs values.

1058 **(F)** Analysis of lysosomal content in LREs and MECs by measuring Lysotracker MFI by flow cytometry. Bar
1059 chart depicts Lysotracker MFI of LREs and MECs from WT mice at P7 (gavaged with mCherry, 16 hours)
1060 and P42 respectively. Single-living $EpCAM^+CD24^-Biopool^-$ cells were gated. For LREs, $mCherry^+$ cells were
1061 selected. See Figure S3 for gating strategy. Dots represent individual mice (n = 3).

1062 Graphs in (E, F) represent mean + SEM. In (E), Student's t test; in (F), Mann–Whitney test. *$p < 0.05$, **p
1063 < 0.01.

1064

1065

1066 **Figure S5. Metabolic Transition in the Small Gut During Postnatal Development**
1067 ***Related to Figure 5***

1068 (**A)** Expression and statistical data of selected genes encoding transcription factors (TFs: *Mafb, c-maf,*
1069 *Blimp1*), neonatal enzymes (*Ass1, Glb1*), and adult enzymes (*Treh, Sis, Arg2*) from the LREs vs MECs
1070 RNA-seq analysis.

1071 **(B and C)** RT-qPCR analysis of *Mafb* and *Blimp1* (B), and of *Ass1, Glb1, Treh,* and *Sis* (C) genes in
1072 epithelial cells isolated from proximal and distal small intestinal segments of WT mice at the indicated
1073 postnatal time points (n = 3). Data are normalised to the expression levels in the proximal small intestine of
1074 E18.5 embryos and expressed as log_{10}fold change (log_{10}FC).

1075 **(D)** Schematic representation of the cellular metabolic pathways. Enzymes used in the Met-flow panel are
1076 shown in red. Scheme adapted from Iborra et al. (2024) (CC BY 4.0).

1077 **(E)** Met-Flow analysis of ileal EpCAM^{+}CD24^{-} cells from WT mice at P7 (LREs) and P42 (MECs) (n = 2–4).
1078 Data relative to LREs values. Bubble colour and size reflect group means for each marker. See Figure S3
1079 for the gating strategy and Table S2 for statistical significance.

1080 In (B, C), graphs represent mean + SD, two-way ANOVA was conducted and only the most relevant
1081 statistically significant comparisons are shown. In (E), Student's *t*-test. *p < 0.05, **p < 0.01, ***p < 0.001,
1082 ****p < 0.0001.

1083

1084 **Figure S6. Validation and Intestinal Phenotype of *Tfamc*KO Neonatal Mice**
1085 ***Related to Figure 6***

1086 **(A)** Relative mitochondrial DNA (mtDNA) levels of *Nd1*, *Co1*, *Co2*, and *Atp6* in ileal epithelial cells from WT
1087 and *Tfam*cKO mice at P10 (n = 2) and P14 (n = 4), measured by qPCR.

1088 **(B)** RT-qPCR analysis of mitochondrial genes *mt-Nd1*, *mt-Co2*, and *Sdha* in ileal epithelial cells from WT
1089 and *Tfam*cKO mice at P10 (n = 5–6).

1090 **(C)** Confocal images of ileal sections from WT (n = 3) and *Tfam*cKO (n = 2) mice at P14, labelled with anti-
1091 MTCO1 (green) and anti-β-catenin (magenta). Arrows point to mitochondria in WT LREs.

1092 **(D)** Violin plot shows MTCO1 intensity (integrated density) from (C), normalised to epithelial area. Dots
1093 represent individual images (n = 9,7; 3–4 images per mouse).

1094 **(E)** PAS and haematoxylin staining of ileal sections from WT and *Tfam*cKO mice at P10 and P14 (n = 4–6)
1095 shows inflamed and disorganized epithelium in *Tfam*cKO mice. Phenotypes include shortened villi (double
1096 red arrows), thickened submucosa and lower mucosa (double black arrows), oedema (asterisks), reduced
1097 PAS+ goblet cells (arrowheads), and abnormal vacuoles in enterocytes (arrows).
1098 Scale bars: 200 µm (main); 100 µm (insets).

1099 **(F–H)** Quantification of villi length (F), percentage of villi with goblet cells (G), and the maximum thickness
1100 of submucosa and lower mucosa (H) from (E). In (F), each dot represents a villus (n = 50,60,50,50; 10 villi
1101 per mouse). For (G–H), n = 4–6 mice.

1102 **(I–K)** Flow cytometry analysis of innate immune cells (IIC, I), B lymphocytes (LB, J), and T-helper cells (LT_h,
1103 K) percentages in the ileal of WT and *Tfam*cKO mice at P10 and P14 (n = 3–5). See Figure S3 for gating
1104 strategy.

1105 **(L–O)** Confocal imaging and quantification of stem and Paneth cells in WT and *Tfam*cKO ileal at P10 and
1106 P14:

1107 - (**L**) Olfm4 (green) labels crypt stem cells; arrows point to Olfm4^{+} crypts.

1108 • (**M**) Quantification of Olfm4$^+$ crypts (30-100 crypts/mouse).

1109 • (**N**) Lysozyme (green) marks Paneth cells; arrows show normal crypt localization, arrowheads
1110 indicate mislocalised Paneth cells in villi.

1111 • (**O**) Quantification Paneth cells/mm² of epithelial area.

1112 For (L, N), sections are also stained with anti-Ecad (white) and DAPI (blue). Scale bars: 200 µm (main);
1113 50 µm (insets). For all panels, n = 3 mice.

1114 **(P)** Distribution of mitochondrial integrity classes in *Tfam*cKO neonatal enterocytes. Quantification of the
1115 percentage, area and aspect ratio (long axis / short axis) of each mitochondria class in Figure 6E, as defined
1116 in Figure 4B. In percentage graph, dots represent individual enterocytes; in area and aspect ratio graphs,
1117 dots are individual mitochondria. Sample sizes are indicated in Table S1.

1118 In (C, E, L, N), dashed boxes indicate magnified areas; L, lumen.

1119 In (A, B, D, I–K), data relative to WT values. In (A, G–K, M, O), graphs represent mean + SEM and dots
1120 represent individual mice. In (B, D), violin plots show the median (thick line) and IQR (thin lines). In (F, P),
1121 dot plots show mean ± SEM (red lines).

1122 Statistical analyses: Student's t test (A, B, I–K, M, O), Mann–Whitney test (D, P), two-way ANOVA (F, H),
1123 Kruskal–Wallis test (G). In (F–H), only statistically significant comparisons between WT and *Tfam*cKO are
1124 indicated within each time group. *p < 0.05, **p < 0.01, ***p < 0.001, ****p < 0.0001.

1125

1126 **Figure S7. *Tfam*cKO Neonatal Enterocytes Exhibit a Decreased Endolysosomal System and**
1127 **Undergo an Early Metabolic Switch**
1128 ***Related to Figure 6***

1129 **(A)** RT-qPCR analysis of transcription factor (*Mafb*, *c-maf*, *Blimp1*), neonatal (*Ass1*, *Glb1*) and adult (*Treh*,
1130 *Sis*, *Arg2*) enzyme genes in ileal epithelial cells from WT and *Tfam*cKO mice at P10 and P14.

1131 **(B)** RT-qPCR analysis of *Dab2*, *Amn*, and *Mamdc4* genes in ileal epithelial cells from WT and *Tfam*cKO
1132 mice at P10 and P14.

1133 **(C)** Confocal images of ileal sections from WT and *Tfam*cKO mice at P10 (n = 3) and P14 (n = 2–3), labelled
1134 with anti-Dab2 (green), anti-β-catenin (white), and DAPI (blue). Arrowheads indicate apical Dab2
1135 localisation.

1136 **(D)** Violin plot shows apical Dab2 intensity (integrated density) from (C), normalised to epithelial area and
1137 relative to WT values. Dots represent individual images (n = 6, 6, 6, 4; 2 images per mouse).

1138 **(E)** RT-qPCR analysis of *Lamp2*, *Mcoln3*, and *Ctsl1* in ileal epithelial cells from WT and *Tfam*cKO mice at
1139 P10 and P14.

1140 **(F)** Confocal images of ileal sections from WT and *Tfam*cKO mice at P10 (n = 3), labelled with anti-LAMP1
1141 (green), anti-β-catenin (white), and DAPI (blue). Arrows indicate endolysosomal system in WT cells;
1142 arrowheads highlight the reduced lysosomal vesicles in *Tfam*cKO enterocytes.

1143 **(G)** Quantification of lysosomal occupation and content in (E). Dot plots show the LAMP1$^+$ area as a
1144 percentage of cell area (n = 157,99) and LAMP1 intensity (integrated density) per enterocyte (n = 117,74).
1145 Dots represent individual enterocytes.

1146 In (C, F), dashed boxes indicate magnified areas; L, lumen. Scale bars: 10 μm (main); 5 μm (insets).

1147 In (A, B, E), data relative to WT-P10 values, dots represent individual mice (n = 4–7), and graphs represent
1148 mean + SEM. In (D), violin plot shows the median (thick line) and IQR (thin lines). In (G), dot plots depict
1149 mean ± SEM (red lines).

1150 Statistical analyses: Kruskal–Wallis test (A [*Treh*], B [*Dab2*], E [*Lamp2*]), two-way ANOVA (A, B, E; except
1151 *Treh*, *Dab2*, *Lamp2*), Student's t test (D), Mann–Whitney test (G). In (A, B, E), only statistically significant
1152 comparisons between WT and *Tfam*cKO are indicated within each time group. *p < 0.05, **p < 0.01, ***p <
1153 0.001, ****p < 0.0001.

1154

1155 **Table S1. Sample sizes in TEM graphs**
1156 ***Related to Figures 4, 6 and S6***
1157 Values in the number (No.) and percentage columns correspond to enterocytes; in the area and aspect
1158 ratio columns, values correspond to individual mitochondria. For more detailed information on sample size
1159 of the analyses, see the TEM section in the Methods.

1160

1161 **Table S2. Statistical Significance of Met-Flow Experiments**
1162 ***Related to Figures 5, 6 and S5***
1163 For Figure 5H, statistical results are shown only for comparisons between WT and the two other groups.
1164 No statistical test was applied for HK1 of Figure S5E (n = 2). *p < 0.05, **p < 0.01, ***p < 0.001, ****p <
1165 0.0001. NS, not significant.

1166

1167

1168 **REFERENCES**

1169 Ahl, P.J., Hopkins, R.A., Xiang, W.W., Au, B., Kaliaperumal, N., Fairhurst, A.-M., Connolly, J.E., 2020. Met-
1170 Flow, a strategy for single-cell metabolic analysis highlights dynamic changes in immune
1171 subpopulations. Commun. Biol. 3, 305. https://doi.org/10.1038/s42003-020-1027-9

1172 Asano, J., Sato, T., Ichinose, S., Kajita, M., Onai, N., Shimizu, S., Ohteki, T., 2017. Intrinsic Autophagy Is
1173 Required for the Maintenance of Intestinal Stem Cells and for Irradiation-Induced Intestinal
1174 Regeneration. Cell Rep. 20, 1050–1060. https://doi.org/10.1016/j.celrep.2017.07.019

1175 Baixauli, F., Acín-Pérez, R., Villarroya-Beltrí, C., Mazzeo, C., Nuñez-Andrade, N., Gabandé-Rodriguez, E.,
1176 Ledesma, M.D., Blázquez, A., Martin, M.A., Falcón-Pérez, J.M., Redondo, J.M., Enríquez, J.A.,
1177 Mittelbrunn, M., 2015. Mitochondrial Respiration Controls Lysosomal Function during Inflammatory
1178 T Cell Responses. Cell Metab. 22, 485–498. https://doi.org/10.1016/j.cmet.2015.07.020

1179 Bara, A.M., Chen, L., Ma, C., Underwood, J., Moreci, R.S., Sumigray, K., Sun, T., Diao, Y., Verzi, M.,
1180 Lechler, T., 2022. Maf family transcription factors are required for nutrient uptake in the mouse
1181 neonatal gut. Dev. Camb. Engl. 149, dev201251. https://doi.org/10.1242/dev.201251

1182 Becker, K., Pons-Kühnemann, J., Fechner, A., Funk, M., Gromer, S., Gross, H.-J., Grünert, A., Schirmer,
1183 R.H., 2005. Effects of antioxidants on glutathione levels and clinical recovery from the malnutrition
1184 syndrome kwashiorkor--a pilot study. Redox Rep. Commun. Free Radic. Res. 10, 215–226.
1185 https://doi.org/10.1179/135100005X70161

1186 Beumer, J., Clevers, H., 2021. Cell fate specification and differentiation in the adult mammalian intestine.
1187 Nat. Rev. Mol. Cell Biol. 22, 39–53. https://doi.org/10.1038/s41580-020-0278-0

1188 Bhutta, Z.A., Berkley, J.A., Bandsma, R.H.J., Kerac, M., Trehan, I., Briend, A., 2017. Severe childhood
1189 malnutrition. Nat. Rev. Dis. Primer 3, 17067. https://doi.org/10.1038/nrdp.2017.67

1190 Birchenough, G.M.H., Schroeder, B.O., Sharba, S., Arike, L., Recktenwald, C.V., Puértolas-Balint, F.,
1191 Subramani, M.V., Hansson, K.T., Yilmaz, B., Lindén, S.K., Bäckhed, F., Hansson, G.C., 2023.
1192 Muc2-dependent microbial colonization of the jejunal mucus layer is diet sensitive and confers local
1193 resistance to enteric pathogen infection. Cell Rep. 42, 112084.
1194 https://doi.org/10.1016/j.celrep.2023.112084

1195 Birgisdottir, Å.B., Johansen, T., 2020. Autophagy and endocytosis – interconnections and
1196 interdependencies. J. Cell Sci. 133, jcs228114. https://doi.org/10.1242/jcs.228114

1197 Boyle, E.I., Weng, S., Gollub, J., Jin, H., Botstein, D., Cherry, J.M., Sherlock, G., 2004. GO::TermFinder—
1198 open source software for accessing Gene Ontology information and finding significantly enriched
1199 Gene Ontology terms associated with a list of genes. Bioinformatics 20, 3710–3715.
1200 https://doi.org/10.1093/bioinformatics/bth456

1201 Cadwell, K., Liu, J.Y., Brown, S.L., Miyoshi, H., Loh, J., Lennerz, J.K., Kishi, C., Kc, W., Carrero, J.A., Hunt,
1202 S., Stone, C.D., Brunt, E.M., Xavier, R.J., Sleckman, B.P., Li, E., Mizushima, N., Stappenbeck,
1203 T.S., Virgin IV, H.W., 2008. A key role for autophagy and the autophagy gene Atg16l1 in mouse
1204 and human intestinal Paneth cells. Nature 456, 259–263. https://doi.org/10.1038/nature07416

1205 Campbell, C.T., Kolesar, J.E., Kaufman, B.A., 2012. Mitochondrial transcription factor A regulates
1206 mitochondrial transcription initiation, DNA packaging, and genome copy number. Biochim. Biophys.
1207 Acta 1819, 921–929. https://doi.org/10.1016/j.bbagrm.2012.03.002

1208 Chen, P.-M., Lin, C.-H., Li, N.-T., Wu, Y.-M., Lin, M.-T., Hung, S.-C., Yen, M.-L., 2015. c-Maf regulates
1209 pluripotency genes, proliferation/self-renewal, and lineage commitment in ROS-mediated
1210 senescence of human mesenchymal stem cells. Oncotarget 6, 35404–35418.
1211 https://doi.org/10.18632/oncotarget.6178

1212 Choo, J., Glisovic, N., Matic Vignjevic, D., 2022. Gut homeostasis at a glance. J. Cell Sci. 135.
1213 https://doi.org/10.1242/jcs.260248

1214 Chung, K.W., Dhillon, P., Huang, S., Sheng, X., Shrestha, R., Qiu, C., Kaufman, B.A., Park, J., Pei, L.,
1215 Baur, J., Palmer, M., Susztak, K., 2019. Mitochondrial Damage and Activation of the STING
1216 Pathway Lead to Renal Inflammation and Fibrosis. Cell Metab. 30, 784-799.e5.
1217 https://doi.org/10.1016/j.cmet.2019.08.003

1218 Cosovanu, C., Resch, P., Jordan, S., Lehmann, A., Ralser, M., Farztdinov, V., Spranger, J., Mülleder, M.,
1219 Brachs, S., Neumann, C., 2022. Intestinal epithelial c-Maf expression determines enterocyte
1220 differentiation and nutrient uptake in mice. J. Exp. Med. 219, e20220233.
1221 https://doi.org/10.1084/jem.20220233

1222 Cox, C.M., Lu, R., Salcin, K., Wilson, J.M., 2018. The Endosomal Protein Endotubin Is Required for
1223 Enterocyte Differentiation. Cell. Mol. Gastroenterol. Hepatol. 5, 145–156.
1224 https://doi.org/10.1016/j.jcmgh.2017.11.001

1225 el Marjou, F., Janssen, K.-P., Chang, B.H.-J., Li, M., Hindie, V., Chan, L., Louvard, D., Chambon, P.,
1226 Metzger, D., Robine, S., 2004. Tissue-specific and inducible Cre-mediated recombination in the
1227 gut epithelium. Genes. N. Y. N 2000 39, 186–193. https://doi.org/10.1002/gene.20042

1228 Foerster, E.G., Mukherjee, T., Cabral-Fernandes, L., Rocha, J.D.B., Girardin, S.E., Philpott, D.J., 2022.
1229 How autophagy controls the intestinal epithelial barrier. Autophagy 18, 86–103.
1230 https://doi.org/10.1080/15548627.2021.1909406

1231 Fujita, M., Reinhart, F., Neutra, M., 1990. Convergence of apical and basolateral endocytic pathways at
1232 apical late endosomes in absorptive cells of suckling rat ileum in vivo. J. Cell Sci. 97, 385–394.
1233 https://doi.org/10.1242/jcs.97.2.385

1234 Fujita, N., Itoh, T., Omori, H., Fukuda, M., Noda, T., Yoshimori, T., 2008. The Atg16L complex specifies the
1235 site of LC3 lipidation for membrane biogenesis in autophagy. Mol. Biol. Cell 19, 2092–2100.
1236 https://doi.org/10.1091/mbc.e07-12-1257

1237 Gong, G., Song, M., Csordas, G., Kelly, D.P., Matkovich, S.J., Dorn, G.W., 2015. Parkin-mediated
1238 mitophagy directs perinatal cardiac metabolic maturation in mice. Science 350, aad2459.
1239 https://doi.org/10.1126/science.aad2459

1240 Gonnella, P.A., Neutra, M.R., 1984. Membrane-bound and fluid-phase macromolecules enter separate
1241 prelysosomal compartments in absorptive cells of suckling rat ileum. J. Cell Biol. 99, 909–917.
1242 https://doi.org/10.1083/jcb.99.3.909

1243 Hansson, J., Panchaud, A., Favre, L., Bosco, N., Mansourian, R., Benyacoub, J., Blum, S., Jensen, O.N.,
1244 Kussmann, M., 2011. Time-resolved Quantitative Proteome Analysis of *In Vivo* Intestinal
1245 Development. Mol. Cell. Proteomics 10, M110.005231. https://doi.org/10.1074/mcp.M110.005231

1246 Harper, J., Mould, A., Andrews, R.M., Bikoff, E.K., Robertson, E.J., 2011. The transcriptional repressor
1247 Blimp1/Prdm1 regulates postnatal reprogramming of intestinal enterocytes. Proc. Natl. Acad. Sci.
1248 U. S. A. https://doi.org/10.1073/pnas.1105852108

1249 He, C., 2022. Balancing nutrient and energy demand and supply via autophagy. Curr. Biol. 32, R684–R696.
1250 https://doi.org/10.1016/j.cub.2022.04.071

1251 Henning, S.J., 1985. Ontogeny of Enzymes in the Small Intestine. Annu. Rev. Physiol. 47, 231–245.
1252 https://doi.org/10.1146/annurev.ph.47.030185.001311

1253 Henning, S.J., 1981. Postnatal development: coordination of feeding, digestion, and metabolism. Am. J.
1254 Physiol.-Gastrointest. Liver Physiol. https://doi.org/10.1152/ajpgi.1981.241.3.G199

1255 Hodzic, Z., Bolock, A.M., Good, M., 2017. The Role of Mucosal Immunity in the Pathogenesis of Necrotizing
1256 Enterocolitis. Front. Pediatr. 5. https://doi.org/10.3389/fped.2017.00040

1257 Hulzebos, C.V., Sauer, P.J.J., 2007. Energy requirements. Semin. Fetal. Neonatal Med., Nutrition 12, 2–
1258 10. https://doi.org/10.1016/j.siny.2006.10.008

1259 Hwang, S., Maloney, N.S., Bruinsma, M.W., Goel, G., Duan, E., Zhang, L., Shrestha, B., Diamond, M.S.,
1260 Dani, A., Sosnovtsev, S.V., Green, K.Y., Lopez-Otin, C., Xavier, R.J., Thackray, L.B., Virgin, H.W.,
1261 2012. Nondegradative role of Atg5-Atg12/ Atg16L1 autophagy protein complex in antiviral activity
1262 of interferon gamma. Cell Host Microbe 11, 397–409. https://doi.org/10.1016/j.chom.2012.03.002

1263 Iborra-Pernichi, M., Ruiz García, J., Velasco de la Esperanza, M., Estrada, B.S., Bovolenta, E.R., Cifuentes,
1264 C., Prieto Carro, C., González Martínez, T., García-Consuegra, J., Rey-Stolle, M.F., Rupérez, F.J.,
1265 Guerra Rodriguez, M., Argüello, R.J., Cogliati, S., Martín-Belmonte, F., Martínez-Martín, N., 2024.
1266 Defective mitochondria remodelling in B cells leads to an aged immune response. Nat. Commun.
1267 15, 2569. https://doi.org/10.1038/s41467-024-46763-1

1268 Jiménez-Loygorri, J.I., Villarejo-Zori, B., Viedma-Poyatos, Á., Zapata-Muñoz, J., Benítez-Fernández, R.,
1269 Frutos-Lisón, M.D., Tomás-Barberán, F.A., Espín, J.C., Area-Gómez, E., Gomez-Duran, A., Boya,

1270 P., 2024. Mitophagy curtails cytosolic mtDNA-dependent activation of cGAS/STING inflammation
1271 during aging. Nat. Commun. 15, 830. https://doi.org/10.1038/s41467-024-45044-1

1272 Kaur, J., Debnath, J., 2015. Autophagy at the crossroads of catabolism and anabolism. Nat. Rev. Mol. Cell
1273 Biol. 16, 461–472. https://doi.org/10.1038/nrm4024

1274 Kawamura, N., Sun-Wada, G.-H., Aoyama, M., Harada, A., Takasuga, S., Sasaki, T., Wada, Y., 2012.
1275 Delivery of endosomes to lysosomes via microautophagy in the visceral endoderm of mouse
1276 embryos. Nat. Commun. 3, 1071. https://doi.org/10.1038/ncomms2069

1277 Kleinman, R.E., Walker, W.A., 1984. Antigen processing and uptake from the intestinal tract. Clin. Rev.
1278 Allergy 2, 25–37. https://doi.org/10.1007/BF02991209

1279 Kulkarni, D.H., Newberry, R.D., 2019. Intestinal Macromolecular Transport Supporting Adaptive Immunity.
1280 Cell. Mol. Gastroenterol. Hepatol. 7, 729–737. https://doi.org/10.1016/j.jcmgh.2019.01.003

1281 Kuma, A., Hatano, M., Matsui, M., Yamamoto, A., Nakaya, H., Yoshimori, T., Ohsumi, Y., Tokuhisa, T.,
1282 Mizushima, N., 2004. The role of autophagy during the early neonatal starvation period. Nature
1283 432, 1032–1036. https://doi.org/10.1038/nature03029

1284 Larabi, A., Barnich, N., Nguyen, H.T.T., 2020. New insights into the interplay between autophagy, gut
1285 microbiota and inflammatory responses in IBD. Autophagy 16, 38–51.
1286 https://doi.org/10.1080/15548627.2019.1635384

1287 Larsson, N.-G., Wang, J., Wilhelmsson, H., Oldfors, A., Rustin, P., Lewandoski, M., Barsh, G.S., Clayton,
1288 D.A., 1998. Mitochondrial transcription factor A is necessary for mtDNA maintance and
1289 embryogenesis in mice. Nat. Genet. 18, 231–236. https://doi.org/10.1038/ng0398-231

1290 Lennicke, C., Cochemé, H.M., 2021. Redox metabolism: ROS as specific molecular regulators of cell
1291 signaling and function. Mol. Cell 81, 3691–3707. https://doi.org/10.1016/j.molcel.2021.08.018

1292 Li, A., Gao, M., Liu, B., Qin, Y., Chen, L., Liu, H., Wu, H., Gong, G., 2022. Mitochondrial autophagy:
1293 molecular mechanisms and implications for cardiovascular disease. Cell Death Dis. 13, 444.
1294 https://doi.org/10.1038/s41419-022-04906-6

1295 Liang, H., Wu, S., Zhang, Z., Khan, M.Z., Zhan, Y., Zhu, M., Wang, S., Liu, W., Wang, C., Cao, G., Han,
1296 Y., 2024. Establishment of a mouse model of ovarian oxidative stress induced by hydrogen
1297 peroxide. Front. Vet. Sci. 11. https://doi.org/10.3389/fvets.2024.1484388

1298 Massaquoi, M.S., Guillemin, K., 2019. Packing in the Proteins. Dev. Cell 51, 1–2.
1299 https://doi.org/10.1016/j.devcel.2019.09.013

1300 McWilliams, T.G., Prescott, A.R., Allen, G.F.G., Tamjar, J., Munson, M.J., Thomson, C., Muqit, M.M.K.,
1301 Ganley, I.G., 2016. mito-QC illuminates mitophagy and mitochondrial architecture in vivo. J. Cell
1302 Biol. 214, 333–345. https://doi.org/10.1083/jcb.201603039

1303 Mizushima, N., Kuma, A., Kobayashi, Y., Yamamoto, A., Matsubae, M., Takao, T., Natsume, T., Ohsumi,
1304 Y., Yoshimori, T., 2003. Mouse Apg16L, a novel WD-repeat protein, targets to the autophagic
1305 isolation membrane with the Apg12-Apg5 conjugate. J. Cell Sci. 116, 1679–1688.
1306 https://doi.org/10.1242/jcs.00381

1307 Mizushima, N., Yamamoto, A., Matsui, M., Yoshimori, T., Ohsumi, Y., 2004. In vivo analysis of autophagy
1308 in response to nutrient starvation using transgenic mice expressing a fluorescent autophagosome
1309 marker. Mol. Biol. Cell 15, 1101–1111. https://doi.org/10.1091/mbc.e03-09-0704

1310 Mizushima, N., Yoshimorim, T., Levine, B., 2010. Methods in Mammalian Autophagy Research. Cell 140,
1311 313–326. https://doi.org/10.1016/j.cell.2010.01.028

1312 Morris, O., Jasper, H., 2021. Reactive Oxygen Species in intestinal stem cell metabolism, fate and function.
1313 Free Radic. Biol. Med. 166, 140–146. https://doi.org/10.1016/j.freeradbiomed.2021.02.015

1314 Moschandrea, C., Kondylis, V., Evangelakos, I., Herholz, M., Schneider, F., Schmidt, C., Yang, M., Ehret,
1315 S., Heine, M., Jaeckstein, M.Y., Szczepanowska, K., Schwarzer, R., Baumann, L., Bock, T.,
1316 Nikitopoulou, E., Brodesser, S., Krüger, M., Frezza, C., Heeren, J., Trifunovic, A., Pasparakis, M.,

2023. Mitochondrial dysfunction abrogates dietary lipid processing in enterocytes. Nature 1–8. https://doi.org/10.1038/s41586-023-06857-0

Muncan, V., Heijmans, J., Krasinski, S.D., Büller, N.V., Wildenberg, M.E., Meisner, S., Radonjic, M., Stapleton, K.A., Lamers, W.H., Biemond, I., Van Den Bergh Weerman, M.A., O'Carroll, D., Hardwick, J.C., Hommes, D.W., Van Den Brink, G.R., 2011. Blimp1 regulates the transition of neonatal to adult intestinal epithelium. Nat. Commun. https://doi.org/10.1038/ncomms1463

Murphy, M.P., 2008. How mitochondria produce reactive oxygen species. Biochem. J. 417, 1–13. https://doi.org/10.1042/BJ20081386

Ni, H.-M., Bockus, A., Wozniak, A.L., Jones, K., Weinman, S., Yin, X.-M., Ding, W.-X., 2011. Dissecting the dynamic turnover of GFP-LC3 in the autolysosome. Autophagy 7, 188–204. https://doi.org/10.4161/auto.7.2.14181

Park, J., Levic, D.S., Sumigray, K.D., Bagwell, J., Eroglu, O., Block, C.L., Eroglu, C., Barry, R., Lickwar, C.R., Rawls, J.F., Watts, S.A., Lechler, T., Bagnat, M., 2019. Lysosome-Rich Enterocytes Mediate Protein Absorption in the Vertebrate Gut. Dev. Cell. https://doi.org/10.1016/j.devcel.2019.08.001

Picca, A., Faitg, J., Auwerx, J., Ferrucci, L., D'Amico, D., 2023. Mitophagy in human health, ageing and disease. Nat. Metab. 5, 2047–2061. https://doi.org/10.1038/s42255-023-00930-8

Popov, L.-D., 2023. Mitochondria as intracellular signalling organelles. An update. Cell. Signal. 109, 110794. https://doi.org/10.1016/j.cellsig.2023.110794

Qi, T., Sun, M., Zhang, C., Chen, P., Xiao, C., Chang, X., 2020. Ascorbic Acid Promotes Plasma Cell Differentiation through Enhancing TET2/3-Mediated DNA Demethylation. Cell Rep. 33. https://doi.org/10.1016/j.celrep.2020.108452

Rath, E., Moschetta, A., Haller, D., 2018. Mitochondrial function — gatekeeper of intestinal epithelial cell homeostasis. Nat. Rev. Gastroenterol. Hepatol. 15, 497–516. https://doi.org/10.1038/s41575-018-0021-x

Remis, N.N., Wiwatpanit, T., Castiglioni, A.J., Flores, E.N., Cantú, J.A., García-Añoveros, J., 2014. Mucolipin Co-deficiency Causes Accelerated Endolysosomal Vacuolation of Enterocytes and Failure-to-Thrive from Birth to Weaning. PLoS Genet. 10. https://doi.org/10.1371/journal.pgen.1004833

Rodríguez-Colman, M.J., Schewe, M., Meerlo, M., Stigter, E., Gerrits, J., Pras-Raves, M., Sacchetti, A., Hornsveld, M., Oost, K.C., Snippert, H.J., Verhoeven-Duif, N., Fodde, R., Burgering, B.M.T., 2017. Interplay between metabolic identities in the intestinal crypt supports stem cell function. Nature 543, 424–427. https://doi.org/10.1038/nature21673

Rodríguez-Fraticelli, A.E., Bagwell, J., Bosch-Fortea, M., Boncompain, G., Reglero-Real, N., García-León, M.J., Andrés, G., Toribio, M.L., Alonso, M.A., Millán, J., Perez, F., Bagnat, M., Martín-Belmonte, F., 2015. Developmental regulation of apical endocytosis controls epithelial patterning in vertebrate tubular organs. Nat. Cell Biol. 17, 241–250. https://doi.org/10.1038/ncb3106

Rombout, J.H., Lamers, C.H., Helfrich, M.H., Dekker, A., Taverne-Thiele, J.J., 1985. Uptake and transport of intact macromolecules in the intestinal epithelium of carp (Cyprinus carpio L.) and the possible immunological implications. Cell Tissue Res. 239, 519–530. https://doi.org/10.1007/BF00219230

Schneider, C.A., Rasband, W.S., Eliceiri, K.W., 2012. NIH Image to ImageJ: 25 years of image analysis. Nat. Methods 9, 671–675. https://doi.org/10.1038/nmeth.2089

Sena, L.A., Chandel, N.S., 2012. Physiological roles of mitochondrial reactive oxygen species. Mol. Cell 48, 158–167. https://doi.org/10.1016/j.molcel.2012.09.025

Sies, H., Berndt, C., Jones, D.P., 2017. Oxidative Stress. Annu. Rev. Biochem. 86, 715–748. https://doi.org/10.1146/annurev-biochem-061516-045037

Skrzypek, T., Valverde Piedra, J.L., Skrzypek, H., Kazimierczak, W., Biernat, M., Zabielski, R., 2007. Gradual disappearance of vacuolated enterocytes in the small intestine of neonatal piglets. J. Physiol. Pharmacol. Off. J. Pol. Physiol. Soc. 58 Suppl 3, 87–95.

1365 Spence, J.R., Lauf, R., Shroyer, N.F., 2011. Vertebrate intestinal endoderm development. Dev. Dyn.
1366 https://doi.org/10.1002/dvdy.22540

1367 Srivillibhuthur, M., Warder, B.N., Toke, N.H., Shah, P.P., Feng, Q., Gao, N., Bonder, E.M., Verzi, M.P.,
1368 2018. TFAM is required for maturation of the fetal and adult intestinal epithelium. Dev. Biol. 439,
1369 92–101. https://doi.org/10.1016/j.ydbio.2018.04.015

1370 Stirling, D.R., Swain-Bowden, M.J., Lucas, A.M., Carpenter, A.E., Cimini, B.A., Goodman, A., 2021.
1371 CellProfiler 4: improvements in speed, utility and usability. BMC Bioinformatics 22, 433.
1372 https://doi.org/10.1186/s12859-021-04344-9

1373 Subramanian, A., Tamayo, P., Mootha, V.K., Mukherjee, S., Ebert, B.L., Gillette, M.A., Paulovich, A.,
1374 Pomeroy, S.L., Golub, T.R., Lander, E.S., Mesirov, J.P., 2005. Gene set enrichment analysis: A
1375 knowledge-based approach for interpreting genome-wide expression profiles. Proc. Natl. Acad.
1376 Sci. 102, 15545–15550. https://doi.org/10.1073/pnas.0506580102

1377 Trehan, I., Manary, M.J., 2015. Management of severe acute malnutrition in low-income and middle-income
1378 countries. https://doi.org/10.1136/archdischild-2014-306026

1379 Treuting, P.M., Arends, M.J., Dintzis, S.M., 2018. 11 - Upper Gastrointestinal Tract, in: Treuting, P.M.,
1380 Dintzis, S.M., Montine, K.S. (Eds.), Comparative Anatomy and Histology (Second Edition).
1381 Academic Press, San Diego, pp. 191–211. https://doi.org/10.1016/B978-0-12-802900-8.00011-7

1382 Walker, W.A., 2013. Initial Intestinal Colonization in the Human Infant and Immune Homeostasis. Ann. Nutr.
1383 Metab. 63, 8–15. https://doi.org/10.1159/000354907

1384 Wallaeys, C., Garcia-Gonzalez, N., Libert, C., 2023. Paneth cells as the cornerstones of intestinal and
1385 organismal health: a primer. EMBO Mol. Med. 15, e16427.
1386 https://doi.org/10.15252/emmm.202216427

1387 Walter, W., Sánchez-Cabo, F., Ricote, M., 2015. GOplot: an R package for visually combining expression
1388 data with functional analysis. Bioinformatics 31, 2912–2914.
1389 https://doi.org/10.1093/bioinformatics/btv300

1390 Wang, S., Long, H., Hou, L., Feng, B., Ma, Z., Wu, Y., Zeng, Y., Cai, J., Zhang, D., Zhao, G., 2023. The
1391 mitophagy pathway and its implications in human diseases. Signal Transduct. Target. Ther. 8, 304.
1392 https://doi.org/10.1038/s41392-023-01503-7

1393 Wilson, J.M., Whitney, J.A., Neutra, M.R., 1991. Biogenesis of the apical endosome–lysosome complex
1394 during differentiation of absorptive epithelial cells in rat ileum. J. Cell Sci. 100, 133–143.
1395 https://doi.org/10.1242/jcs.100.1.133

1396 Yang, Y., Chen, X., Liao, X., Jiang, W., Zhou, Y., Sun, Y., Zheng, B., 2024. Identification of MAP1LC3A as
1397 a promising mitophagy-related gene in polycystic ovary syndrome. Sci. Rep. 14, 16982.
1398 https://doi.org/10.1038/s41598-024-67969-9

1399 Yim, W.W.-Y., Mizushima, N., 2020. Lysosome biology in autophagy. Cell Discov. 6, 6.
1400 https://doi.org/10.1038/s41421-020-0141-7

1401 Yu, G., Wang, L.-G., Han, Y., He, Q.-Y., 2012. clusterProfiler: an R Package for Comparing Biological
1402 Themes Among Gene Clusters. OMICS J. Integr. Biol. 16, 284–287.
1403 https://doi.org/10.1089/omi.2011.0118

1404 Zemirli, N., Morel, E., Molino, D., 2018. Mitochondrial Dynamics in Basal and Stressful Conditions. Int. J.
1405 Mol. Sci. 19, 564. https://doi.org/10.3390/ijms19020564

1406 Zhao, Y.G., Codogno, P., Zhang, H., 2021. Machinery, regulation and pathophysiological implications of
1407 autophagosome maturation. Nat. Rev. Mol. Cell Biol. 22, 733–750. https://doi.org/10.1038/s41580-
1408 021-00392-4

1409 Zhong, Y., Xia, S., Wang, G., Liu, Q., Ma, F., Yu, Y., Zhang, Y., Qian, L., Hu, L., Xie, J., 2024. The interplay
1410 between mitophagy and mitochondrial ROS in acute lung injury. Mitochondrion 78, 101920.
1411 https://doi.org/10.1016/j.mito.2024.101920

1412

1413 **METHODS**

1414 **KEY RESOURCES TABLE**

REAGENT or RESOURCE	SOURCE	IDENTIFIER
Antibodies		
Mouse monoclonal anti-GFP, HRP-conjugated (clone GG4-2C2.12.10)	Miltenyi Biotec	130-091-833
Rat monoclonal anti-RFP (clone 5F8)	Chromotek	5F8
Rabbit polyclonal anti-USP7	Bethyl	A300-033A
Rabbit polyclonal anti-ATG16L1	MBL	PM040
Mouse monoclonal anti-LC3C (clone E5Q2K)	CST	83506
Rabbit polyclonal anti-Actin	Sigma	A2103
Mouse monoclonal anti-SQSTM1 (clone 2C11)	Abnova	H00008878-M01
Mouse monoclonal anti-Dab2 (clone 52/p96)	BD Biosciences	610464
Rat monoclonal anti-LAMP1 (clone 1D4B)	DSHB	1D4B
Rabbit polyclonal anti-Trehalase	GeneTex	GTX109979
Rabbit polyclonal anti-β-catenin	Santa Cruz Biotechnology	sc-7199
Rabbit polyclonal anti-Parkin	Abcam	ab15494
Rabbit polyclonal anti-MafB	Novus Biologicals	NBP1-81342
Rabbit polyclonal anti-Blimp1	Invitrogen	PA5-20310
Mouse monoclonal anti-E-Cadherin (clone 36/E)	BD Biosciences	610181
Goat polyclonal anti-GPX3	R&D Systems	AF4199
Mouse monoclonal anti-MTCO1 (clone 1D6E1A8)	Thermo Fisher Scientific	459600
Rabbit monoclonal anti-Olfm4 (clone D6Y5A)	CST	39141
Rabbit polyclonal anti-Lysozyme	Dako	A0099
Alexa Fluor 647 rabbit monoclonal anti-ASS1 (clone EPR12398)	Abcam	ab311083
Rat monoclonal anti-CD16/32 (clone 93)	Biolegend	101330
PerCP-eFluor710 rat monoclonal anti-EpCAM (clone G8.8)	Invitrogen	46-5791-82
APC rat monoclonal anti-EpCAM (clone G8.8)	Biolegend	118214
BV605 rat monoclonal anti-EpCAM (clone G8.8)	Biolegend	118227
Pacific Blue rat monoclonal anti-CD24 (Clone M1/69)	Biolegend	101820
PE rat monoclonal anti-c-Kit (clone 2B8)	Biolegend	105807
BV785 rat monoclonal anti-c-Kit (clone 2B8)	Biolegend	105841
Alexa Fluor 700 rat monoclonal anti-CD11b (clone M1/70)	Biolegend	101222
Biotin rat monoclonal anti-CD11c (clone N418)	Biolegend	105841
APC-Fire810 rat monoclonal anti-B220 (clone RA3-6B2)	Biolegend	103278
APC-Fire810 rat monoclonal anti-CD4 (clone GK1.5)	Biolegend	100480
RY586 rat monoclonal anti-CD4 (clone GK1.5)	BD Biosciences	568162
Biotin rat monoclonal anti-CD19 (clone 6D5)	Biolegend	115504
Biotin rat monoclonal anti-CD3e (clone 145-2C11)	Biolegend	79751
Biotin rat monoclonal anti-CD45.2 (clone 104)	Biolegend	109804
Rabbit polyclonal anti-GLS	Thermo Fisher Scientific	PA5-35365
Alexa Fluor 647 rabbit monoclonal anti-HK1 (clone EPR10134(B))	Abcam	ab197864

Alexa Fluor 488 mouse monoclonal anti-CPT1A (clone 8F6AE9)	Abcam	ab171449
Rabbit monoclonal anti-ACAC (clone EPR23235-147)	Abcam	ab269273
Alexa Fluor 488 rabbit monoclonal anti-CS (clone EPR8067)	Abcam	ab197488
PE rabbit monoclonal anti-IDH2 (clone EPR7577)	Abcam	ab212122
Alexa Fluor 594 rabbit monoclonal anti-ATP5A (clone EPR23235- 147)	Abcam	ab216385
BB700 rat monoclonal anti-BLIMP1 (clone 5E7)	BD Biosciences	567830
Alexa Fluor 488 donkey polyclonal anti-mouse IgGs	Thermo Fisher Scientific	A-21202
Alexa Fluor 488 donkey polyclonal anti-rabbit IgGs	Thermo Fisher Scientific	A-21206
Alexa Fluor 488 donkey polyclonal anti-rat IgGs	Thermo Fisher Scientific	A-21208
Alexa Fluor 555 donkey polyclonal anti-mouse IgGs	Thermo Fisher Scientific	A-31570
Alexa Fluor 647 donkey polyclonal anti-rabbit IgGs	Thermo Fisher Scientific	A-31573
Alexa Fluor 647 donkey polyclonal anti-mouse IgGs	Thermo Fisher Scientific	A-31571
Peroxidase AffiniPure donkey polyclonal Anti-Mouse IgG	Jackson Immunoresearch	715-035-151
HRP donkey anti-rabbit IgG	Cytiva	NA934
Peroxidase AffiniPure goat polyclonal Anti-Rat IgG	Jackson Immunoresearch	112-035-003
Chemicals, peptides, and recombinant proteins		
Tamoxifen	Merck	T5648
Leupeptin	Sigma	L2884
Hydrogen Peroxide 30%	Merck	108597
Dextran rhodamine B, 10000MW, neutral	Invitrogen	D1824
Dextran Alexa Fluor 647, 10000MW, anionic, fixable	Invitrogen	D22914
Paraformaldehyde, powder, TECHNICAL	VWR Chemicals	28794.295
Tissue-Tek O.C.T. Compound	Sakura	4583
Sucrose	Merck	1076511000
DAPI	Merck	268298
Phalloidin Alexa Fluor™ 488	ThermoFisher	A12379
Phalloidin Alexa Fluor™ 647	ThermoFisher	A22287
ProLong™ Glass Antifade Mountant	Thermo Fisher	P36984
Ghost Dye Violet 540	TONBO Biosciences	13-0879-T100
Ghost Dye Red 780	TONBO Biosciences	13-0865-T100
Streptavidin-BV421	Biolegend	405225
CM-H2DCFDA	Invitrogen	C6827
MitoTracker Green FM	Invitrogen	M7514
MitoTracker Red CMXRos	Invitrogen	M7512
MitoSOX	Invitrogen	M36008
LysoTracker Green DND-26	Invitrogen	L7526
eBioscience FOXP3/Transcription Factor Staining Buffer Set	Invitrogen	00-5523-00
ECL Western Blotting Reagents	Cytiva	RPN2106
DTT	Thermo Scientific	R0861
Oligonucleotides		
Genotyping primers for *Atg16l1*$^{fl/fl}$: forward: 5' CTTTCTCAACAGAACCAGCAGTAC 3'	IDT	N/A
Genotyping primers for *Atg16l1*$^{fl/fl}$: reverse: 5' GTTCAGGTCAATCACCAACTGAGC 3'	IDT	N/A

Genotyping primers for *Tfam*$^{fl/fl}$: forward: 5' CTGCCTTCCTCTAGCCCGGG 3'	IDT	N/A
Genotyping primers for *Tfam*$^{fl/fl}$: reverse: 5' GTAACAGCAGACAACTTGTG 3'	IDT	N/A
Genotyping primers for *Tfam*$^{fl/fl}$: reverse-2: 5' CTCTGAAGCACATGGTCAAT- 3'	IDT	N/A
Genotyping primers for *Villin-creER*^{T2}: forward: 5'- CAAGCCTGGCTCGACGGCC -3'	Sigma	N/A
Genotyping primers for *Villin-creER*^{T2}: reverse: 5'-CGCGAACATCTTCAGGTTCT-3'	Sigma	N/A
Genotyping primers for m*ito-QC*: forward: 5'- CAAAGACCCCAACGAGAAGC -3'	IDT	N/A
Genotyping primers for *mito-QC*: forward-2: 5'- CCCAAGGCACACAAAAAACC -3'	IDT	N/A
Genotyping primers for *mito-QC*: reverse: 5'-CTCTTCCCTCGTGACCTGCAACTCC-3'	IDT	N/A
Genotyping primers for *mito-QC*: reverse-2: 5'- CATGTCTTTAATCTACCTCGATGG -3'	IDT	N/A
Genotyping primers for *GFP-LC3*: forward: 5'-ATAACTTGCTGGCCTTTCCACT -3'	IDT	N/A
Genotyping primers for *GFP-LC3*: reverse: 5'- CGGGCCATTTACCGTAAGTTAT-3'	IDT	N/A
Genotyping primers for *GFP-LC3*: reverse-2: 5'-GCAGCTCATTGCTGTTCCTCAA-3'	IDT	N/A
RT-qPCR primers for *Atg16l1*: forward: 5' ACATGATGGTGCGTGGAATG 3'	Sigma	N/A
RT-qPCR primers for *Atg16l1*: reverse: 5' TCCTTGTCCTTCTGCTGCAT 3'	Sigma	N/A
RT-qPCR primers for *Tfam*: forward: 5' CAGGAGGCAAAGGATGATTC 3'	Sigma	N/A
RT-qPCR primers for *Tfam*: reverse: 5' CCAAGACTTCATTTCATTGTCG 3'	Sigma	N/A
RT-qPCR primers for *Dab2*: forward: 5' CGAAAGCGCCATCAAAGAAG 3'	IDT	N/A
RT-qPCR primers for *Dab2*: reverse: 5' CCTTTGAACCTGGCCAACAA 3'	IDT	N/A
RT-qPCR primers for *Mcoln3*: forward: 5' ATGGAGTTCATCAACGGGTG 3'	IDT	N/A
RT-qPCR primers for *Mcoln3*: reverse: 5' ATAGTTGACGTCCCGAGAAG 3'	IDT	N/A
RT-qPCR primers for *Lamp2*: forward: 5' TGCAGAATGGGAGATGAATTT 3'	IDT	N/A
RT-qPCR primers for *Lamp2*: reverse: 5' GGCACTATTCCGGTCATCC 3'	IDT	N/A
RT-qPCR primers for *Ctsl1*: forward: 5' CCAGCTACACAACGGGGAAT 3'	IDT	N/A
RT-qPCR primers for *Ctsl1*: reverse: 5' AGCATCAGCGGTTCCTGAAA 3'	IDT	N/A
RT-qPCR primers for *Bnip3*: forward: 5' TGTTGGATGCCCAGCATGAA 3'	IDT	N/A
RT-qPCR primers for *Bnip3*: reverse: 5' AATCTTCCTCAGACAGAGTGCT 3'	IDT	N/A
RT-qPCR primers for *Prkn*: forward: 5' AAACCGGATGAGTGGTGAGT 3'	IDT	N/A

RT-qPCR primers for *Prkn*: reverse: 5' AGCTACCGACGTGTCCTTGT 3'	IDT	N/A
RT-qPCR primers for *Pink1*: forward: 5' GCTGATCGAGGAGAAGCAG 3'	IDT	N/A
RT-qPCR primers for *Pink1*: reverse: 5' GATAATCCTCCAGACGGAAGC 3'	IDT	N/A
RT-qPCR primers for *Mafb*: forward: 5' AGAGGCGGACCCTGAAAAAC 3'	IDT	N/A
RT-qPCR primers for *Mafb*: reverse: 5' GTTTTCTCGGAAGCCGTTGC 3'	IDT	N/A
RT-qPCR primers for *c-maf*: forward: 5' GCATGCTGGACATGTATGGT 3'	IDT	N/A
RT-qPCR primers for *c-maf*: reverse: 5' ATGTACAACGGGAGGCTGAA 3'	IDT	N/A
RT-qPCR primers for *Blimp1*: forward: 5' TTCTTGTGTGGTATTGTCGGGACTT 3'	Sigma	N/A
RT-qPCR primers for *Blimp1*: reverse: 5' TTGGGGACACTCTTTGGGTAGAGTT 3'	Sigma	N/A
RT-qPCR primers for *Ass1*: forward: 5' CATTGGAATGAAGTCCCGAG 3'	IDT	N/A
RT-qPCR primers for *Ass1*: reverse: 5' GATTTTGCGTACTTCCCGAT 3'	IDT	N/A
RT-qPCR primers for *Glb1*: forward: 5' ACTGCTGCAACTGCTGGG 3'	Sigma	N/A
RT-qPCR primers for *Glb1*: reverse: 5' AATGGCTGTCCATCCTTGAG 3'	Sigma	N/A
RT-qPCR primers for *Treh*: forward: 5' GCACCTGCTGCTTCTGCT 3'	Sigma	N/A
RT-qPCR primers for *Treh*: reverse: 5' CATCTGAACTTGGTGCAGGA 3'	Sigma	N/A
RT-qPCR primers for *Sis*: forward: 5' GCCCACGCGTTTGGTGAGAC 3'	Sigma	N/A
RT-qPCR primers for *Sis*: reverse: 5' ATCAGCAGTGCAGGGCCCCA 3'	Sigma	N/A
RT-qPCR primers for *Arg2*: forward: 5' TGATTGGCAAAAGGCAGAGG 3'	Sigma	N/A
RT-qPCR primers for *Arg2*: reverse: 5' CTAGGAGTAGGAAGGTGGTC 3'	Sigma	N/A
RT-qPCR primers for *Gpx3*: forward: 5' AATTAGGCACAAAGCCCCCA 3'	IDT	N/A
RT-qPCR primers for *Gpx3*: reverse: 5' CATTCTGGGCTTCCCTTCCA 3'	IDT	N/A
RT-qPCR primers for *Cat*: forward: 5' GAACGGCAATAGGGGTCCTC 3'	IDT	N/A
RT-qPCR primers for *Cat*: reverse: 5' TGGTACACGCAAAAGGAGCA 3'	IDT	N/A
RT-qPCR primers for *Amn*: forward: 5' ATCTGTGAGAGCCTCGGCG 3'	IDT	N/A
RT-qPCR primers for *Amn*: reverse: 5' GTTGGAGGCAGTATCGAAGGA 3'	IDT	N/A
RT-qPCR primers for *Mamdc4*: forward: 5' TCACCACTGCCAGAACAAGG 3'	IDT	N/A
RT-qPCR primers for *Mamdc4*: reverse: 5' CTAACTGGTTCCACGGTCCC 3'	IDT	N/A

RT-qPCR primers for *mt-Nd1*: forward: 5' TCCCCTACCAATACCACACC 3'	Sigma	N/A
RT-qPCR primers for *mt-Nd1*: reverse: 5' TGAAATTGTTTGGGCTACGG 3'	Sigma	N/A
RT-qPCR primers for *mt-Co2*: forward: 5' ACGAAATCAACAACCCCGTA 3'	Sigma	N/A
RT-qPCR primers for *mt-Co2*: reverse: 5' GGCAGAACGACTCGGTTATC 3'	Sigma	N/A
RT-qPCR primers for *Sdha*: forward: 5' GCGGCTTTCACTTCTCTGTT 3'	IDT	N/A
RT-qPCR primers for *Sdha*: reverse: 5' CTCAGAAAGGCCAAATGCAG 3'	IDT	N/A
qPCR primers for *mt-Co1*: forward: 5' ATCCCTTGACATCGTGCTTC 3'	Sigma	N/A
qPCR primers for *mt-Co1*: reverse: 5' AAGTGGGCTTTTGCTCATGT 3'	Sigma	N/A
qPCR primers for *mt-Atp6*: forward: 5' ACAGGCTTCCGACACAAACT 3'	Sigma	N/A
qPCR primers for *mt-Atp6*: reverse: 5' GGTAGCTGTTGGTGGGCTAA 3'	Sigma	N/A
qPCR primers for *Hk2*: forward: 5' GCCAGCCTCTCCTGATTTTAGTGT 3'	Sigma	N/A
qPCR primers for *Hk2*: reverse: 5' GGGAACACAAAAGACCTCTTCTGG 3'	Sigma	N/A
RT-qPCR primers for *Ppib*: forward: 5' CACCAATGGCTCACAGTTCTT 3'	IDT	N/A
RT-qPCR primers for *Ppib*: reverse: 5' ATGACATCCTTCAGTGGCTTG 3'	IDT	N/A

Mice

Atg16l1$^{fl/fl}$ (Hwang et al., 2012), *Tfam*$^{fl/fl}$ (Larsson et al., 1998), and GFP-LC3 (Mizushima et al., 2004) mice were kindly provided by N. Martínez-Martín (Centro de Biología Molecular "Severo Ochoa", CBM, CSIC-UAM, Madrid, Spain). The *mito*-QC mouse line (McWilliams et al., 2016) was obtained from P. Boya (Centro de Investigaciones Biológicas Margarita Salas, CSIC, Madrid, Spain; University of Fribourg, Switzerland). *Villin-creER*^{T2} mice (el Marjou et al., 2004) were provided by N. Djouder (Spanish National Cancer Research Centre, CNIO, Madrid, Spain). *Atg16l1* $^{fl/fl}$, *Tfam* $^{fl/fl}$ mice were crossed at the CBM animal facility with *Villin-creER*^{T2} mice to generate intestinal epithelial-specific conditional knockout (cKO) mice: *Atg16*cKO and *Tfam*cKO, respectively. In turn, *Atg16*cKO mice were crossed with *mito*-QC mice to establish *the mQ-Atg16*cKO mouse line. Tamoxifen (0.12–0.5 mg in corn oil containing 10% ethanol) was administered subcutaneously at postnatal days 1 and 2 to pups from *Atg16*cKO, *mQ-Atg16*cKO, and *Tfam*cKO litters, following a protocol similar to that described by Gong et al. (2015). Cre-positive animals were classified as KO, and Cre-negative mice as WT. Neonatal mice were humanely sacrificed by decapitation; adult mice were euthanized via CO_2 inhalation. *Tfam*cKO neonates were sacrificed after two consecutive days without weight gain or upon observing approximately a 10% weight loss, in accordance with humane endpoint criteria. No test was performed to determine the influence of sex, as no apparent differences were found.

1434 Mouse colonies were maintained at CBM under specific pathogen-free conditions and on a C57BL/6 genetic
1435 background. Mice were housed four/five per cage with food and water available ad libitum and maintained
1436 in a temperature-controlled environment on a 12 h–12 h light–dark cycle with light onset at 08:00. Animal
1437 experiments were performed under protocols approved by the CBM and Comunidad Autónoma de Madrid
1438 ethical committees under the following protocol approval number (PROEX 307.2/21). All animal procedures
1439 conformed to EU Directive 86/609/EEC and Recommendation 2007/526/EC regarding the protection of
1440 animals used for experimental and other scientific purposes, enforced in Spanish law under Real Decreto
1441 1201/2005.
1442
1443 **mCherry / fluorescent-dextran uptake assay**
1444 Mice from GFP-LC3, *Atg16*cKO, and *Tfam*cKO lines were fasted for 1 hour and orally gavaged with either
1445 mCherry or 10 kDa fluorescent-dextran (0.3–1 mg/ml in PBS; 10 µl/g body weight). Following gavage, mice
1446 were sacrificed either 3 or 16 hours later, adapted from the protocol reported by Remis et al. (2014). To
1447 test the endocytic function in neonatal enterocytes, WT mice at postnatal day 7 (P7) were sequentially
1448 gavaged with two distinct 10 kDa fluorescent-dextrans (0.7 mg/ml in PBS; 10 µl/g body weight), following a
1449 modified version of the protocol established in mouse embryos by Kawamura et al. (2012). After a 1-hour
1450 fasting period, pups were first gavaged with Alexa Fluor 647-dextran and then returned to their mother.
1451 Three hours later, they were given rhodamine B–dextran again. Pups were subsequently sacrificed either
1452 1 or 5 hours after the second gavage, and ileal enterocytes were analysed by confocal microscopy to assess
1453 dextran uptake and intracellular localization.
1454
1455 **Leupeptin and hydrogen peroxide treatment**
1456 To inhibit lysosomal proteases and block autophagy, mice were injected subcutaneously with 40 mg/Kg
1457 leupeptin (Sigma) dissolved in PBS and sacrificed after 16h (Jiménez-Loygorri et al., 2024). To assess the
1458 effect of ROS on intestinal epithelial maturation, mice were injected intraperitoneally with hydrogen peroxide
1459 (5.1 µmol/g body weight; Merck) once daily from postnatal day (P)5 to P12 (day of sacrifice), following a
1460 protocol adapted from Liang et al. (2024).
1461
1462 **Histology and Immunofluorescence**
1463 Portions of the distal small intestine from mice were fixed in 4% PFA for 16 hours at 4 °C, embedded in
1464 paraffin resin, and cut transversely into 5-µm sections. Some samples were stained with hematoxylin-eosin
1465 (HE&E; Sigma and Merck, respectively), while others underwent Periodic Acid-Schiff (PAS) staining.
1466 Additionally, some samples were used for immunofluorescence. For immunofluorescence, sections were
1467 deparaffinized using xylene and then rehydrated through a series of decreasing ethanol concentrations
1468 (100%, 96%, 70%, 50%). For antigen retrieval, tissue was boiled at 100 °C on a heat block in sodium citrate
1469 buffer (10 mM Sodium citrate, 0.05% Tween 20, pH 6.0) for 20 min. Next, the slides were washed with
1470 water and PBS containing calcium and magnesium, and then incubated for 1 hour at room temperature

1471 with 3% bovine serum albumin (BSA) as a blocking solution. For O.C.T. embedded sections, portions of
1472 the distal small intestine were previously fixed in 4% PFA for 16 hours at 4 °C, incubated in 30% sucrose
1473 in PBS for 48-72 hours at 4 °C, and then embedded in O.C.T. compound and stored at -80 °C until use.
1474 O.C.T. blocks were cut transversely into 15 µm sections using Superfrost Plus Adhesion Microscope Slides
1475 (Epredia) and stored at -80 °C. For immunofluorescence, sections were dried at room temperature for 30
1476 minutes, washed with 0.1% Tween 20, and blocked for 1 hour at room temperature with BGT buffer (0.3%
1477 BSA, 0.75% Glycine, 0.3% Triton X-100 in PBS). For both paraffin-embedded and O.C.T.-embedded
1478 samples, the primary antibody was added and incubated overnight at 4 °C in the respective blocking buffer.
1479 After washing with PBS, the secondary antibody was incubated with DAPI for 1h at RT. Lastly, slides were
1480 assembled with coverslips with Prolong Glass Antifade (Thermo Fisher). Antibodies used are specified in
1481 the key resources table.
1482
1483 **Image Acquisition and Analysis**
1484 HE&E and PAS staining images were acquired using an Axio Imager M1 vertical wide-field microscope,
1485 coupled with a Leica DMC6200 CMOS Colour camera. The objective used was 10X/0.3 Air EC Plan-Neo.
1486 LASXv4.13 software was used to stitch the tiles into an image. The analysis of goblet cells, villi length, and
1487 submucosa–lower mucosa thickness was performed using Fiji (ImageJ 1.54f; https://fiji.sc/) (Wayne
1488 Rasband, NIH, USA) (Schneider et al., 2012). Lower mucosa was defined as the sum of the *muscularis*
1489 *mucosae*, *lamina propria* and epithelial compartment of the crypts. For villi length analysis, the 10 longest
1490 villi per section were chosen. One section per mouse was analysed from 3–6 mice per genotype. For
1491 immunofluorescence, images were acquired using a Zeiss LSM 900 confocal microscope mounted on an
1492 Axio Imager Z2 upright stand, with sequential acquisition and bidirectional scanning. For individual fields, a
1493 63×/1.4 NA oil-immersion Plan-Apochromat objective was used, with a voxel size of 50 × 50 × 520 nm. For
1494 tile scans, images were acquired using a 20×/0.8 NA air Plan-Apochromat objective, with a voxel size of
1495 0.624 × 0.624 × 1.9 µm, and stitched using ZEN Blue software version 3.4 (Zeiss;
1496 https://www.zeiss.com/zen). For the analysis of Paneth cells and Olfm4^{+} crypts in the ileum of *Tfam*cKO
1497 mice, all cells and all crypts were quantified per section (one section per mouse; 3 mice per genotype). For
1498 intensity analysis, all images were acquired with 16-bit resolution and under the same conditions. An
1499 average intensity projection was made, and the endothelial cells (lacteal vessel) were cropped. The same
1500 threshold was applied to all images to select positive areas. Images were analysed using CellProfiler 4.2.8
1501 (https://cellprofiler.org/) (Stirling et al., 2021) and Fiji (ImageJ 1.54f) (Schneider et al., 2012). Intensity
1502 values correspond to the integrated density, normalized to the epithelial nuclear area (defined by DAPI in
1503 epithelial cells) for BLIMP1 and MAFB, or to the epithelial area (delimited by β-catenin, E-cadherin, or F-
1504 actin) for all other markers, except for LAMP1 (in both KO models) and Rd-dextran (only in *Atg16*cKO mice),
1505 which were not normalized. For LAMP1 intensity and area analysis in *Tfam*cKO mice, images were
1506 deconvolved using Huygens Professional software (version 24.10; Scientific Volume Imaging,
1507 https://svi.nl/Huygens-Professional). For the analysis of Rd-dextran intensity and LAMP1 area and intensity

1508 in *Atg16*cKO mice, 25–40 and 26–36 enterocytes per condition were analysed, respectively. For LAMP1
1509 area and intensity analysis in *Tfam*cKO mice, a minimum of 30 enterocytes per mouse were quantified,
1510 across 3 mice per group (99–167 enterocytes per group). For all other intensity analyses, 2–5 random
1511 images per mouse were acquired from comparable villi, each containing approximately 50 cells, with 2–5
1512 mice per group.
1513
1514 **Transmission Electron Microscopy**
1515 Samples were processed by the Electron Microscopy Unit at CBM. Distal small intestine portions were fixed
1516 using 4% PFA (paraformaldehyde) and 2% glutaraldehyde in phosphate buffer 0.1M, pH 7.4, for 2 hours at
1517 room temperature. Then they were washed 3 times for 10 minutes with phosphate buffer. After fixation, the
1518 material was post-fixed in 1% osmium tetroxide and potassium ferricyanide for 1 hour at 4 °C, then
1519 embedded in tannic acid for 1 minute and block-stained with 2% uranyl acetate for 1 hour in the dark. Next,
1520 they were dehydrated in crescent concentrations of ethanol (30%, 50%, 70%, 95%, 3x100%; 10 minutes
1521 each) and infiltrated in propylene oxide for 45 minutes and Epon 100% for 1 hour. Finally, the samples were
1522 introduced into BEEM capsules (ESBE Scientific). Samples were observed using a JEM1400 Flash
1523 Transmission Electron Microscope (JEOL) equipped with a CMOS OneView camera (Gatan). Fiji (ImageJ
1524 1.54f) (Schneider et al., 2012) was used for image analysis. Mitochondria were classified into three
1525 categories, as in Moschandrea et al. (2023): class I (normal), characterized by mitochondria with narrow
1526 and well-defined cristae; class II (partly affected), with mitochondria exhibiting undefined cristae; and class
1527 III (damaged), including mitochondria with wide, short, and less electron-dense cristae, or those with
1528 ruptured membranes or internal inclusions. For the analysis of mitochondrial status in *Atg16*cKO mice, 291–
1529 340 mitochondria were analysed from 10–11 enterocytes (3 mice per genotype). For *Tfam*cKO mice, in the
1530 analysis of number and percentage of mitochondrial classes, 444–1040 mitochondria from 13–24
1531 enterocytes (3–4 mice per group) were used; for area and aspect ratio analysis, 261–520 mitochondria
1532 from 11–17 enterocytes (2–4 mice per group) were analysed. The graphs show data after outlier exclusion.
1533
1534 **Isolation of IEC**
1535 Mice were euthanized, and the abdominal cavity was opened to expose the intestine. The region of interest
1536 (proximal or distal intestine) was dissected, removed, and rinsed in PBS. The tissue was cut transversely
1537 into ~5 mm fragments, which were then opened longitudinally and incubated in epithelial dissociation buffer
1538 (1 mM DTT, 1 mM EDTA, 2% FBS in PBS) at 37°C with agitation for 20 minutes. After incubation, the
1539 samples were centrifuged at 1200 rpm for 5 minutes. The supernatant was discarded, and the pellet was
1540 resuspended in 10 mL of DMEM supplemented with 10% FBS at 4 °C. The suspension was passed through
1541 70 µm cell strainers (Falcon) and then centrifuged again at 1,200 rpm for 5 minutes. The resulting pellet
1542 was resuspended in FACS buffer (1 mM EDTA, 2% FBS in PBS) at 4 °C and centrifuged again under the
1543 same conditions. The final pellet containing epithelial cells was used for western blotting, flow cytometry,
1544 and RT-qPCR analysis.

1545

1546 **Immunoblotting**

1547 IECs pellets were lysed with lysis buffer (50 mM Tris-HCl, 150 mM NaCl, 1% NP-40, 50 mM NaF, 0.1%
1548 SDS, 1 mM Na_3VO_4, 30 mM β-glycerophosphate, 5 mM EDTA, protease inhibitors) and centrifuged for 10
1549 minutes at 4 °C, 15,000 rpm. Supernatants were collected and quantified using the Bradford protein assay
1550 (Biorad Protein Assay, Biorad). 25 µg of protein was loaded in 10 or 12% acrylamide gels for SDS-PAGE.
1551 After electrophoresis, proteins were transferred to an Immobilon-P transfer membrane (Millipore), blocked
1552 for 1 hour, and incubated overnight with primary antibodies at 4 °C. After washing with 0.05% Tween 20,
1553 they were incubated with HRP-conjugated secondary antibodies for 1 hour at room temperature. ECL
1554 western blotting reagents (Cytiva) were used for the chemiluminescence reaction. Bands were analysed
1555 using Fiji (ImageJ 1.54f) (Schneider et al., 2012). Antibodies used are specified in the key resources table.

1556

1557 **Flow Cytometry**

1558 Disaggregated epithelial cells were plated into a 96-well plate and incubated with FACS buffer with anti-
1559 CD16/CD32 Fc block and viability markers (Ghost Dye) for 10 min at room temperature. After centrifugation,
1560 cells were incubated for 20 min at 4ºC with the appropriate combination of the antibodies in FACS buffer to
1561 discern between the different epithelial and immune populations. Following protocols adapted from
1562 immunometabolic (Baixauli et al., 2015; Iborra-Pernichi et al., 2024) and intestinal studies (Asano et al.,
1563 2017), we assessed mitochondrial mass and membrane potential, cellular and mitochondrial ROS levels,
1564 and lysosomal content labelling cells with MitoTracker Green FM (50 nM), MitoTracker Red CMXRos (100
1565 nM), CM-H2DCFDA (2.5 µM), MitoSOX (1 µM), and Lysotracker Green DND-26 (100 nM), respectively.
1566 Probes were incubated for 15 min at room temperature and 15 min at 37 °C in DMEM with 5% FBS
1567 (Lysotracker), without FBS (MitoTracker and CM-H2DCFDA), or in HBSS (MitoSOX). Antibodies used are
1568 specified in the key resources table. Data were acquired using a Cytek Aurora full-spectrum cytometer at
1569 the CBM, and analysed with FlowJo software (versions 10 and 10.8.1; BD Biosciences). See Figure S3 for
1570 details on the gating strategies.

1571

1572 **Met-flow cytometry staining**

1573 Based on recent works on immune cell metabolism (Ahl et al., 2020; Iborra-Pernichi et al., 2024), we
1574 selected eight key metabolic enzymes to analyse their expression by flow cytometry in our epithelial cells:
1575 ASS1, GLS, HK1, CPT1A, ACAC, CS, IDH2, and ATP5A. After the disaggregated epithelial cells were
1576 incubated with surface antibodies according to the flow cytometry protocol, they were fixed and
1577 permeabilized using the eBioscience Foxp3/Transcription Factor Staining Buffer Set (Invitrogen). Next, they
1578 were washed in the provided wash buffer and blocked with 20% FBS in wash buffer and incubated for 2h
1579 at room temperature with the appropriate antibodies to detect the rate-limiting enzymes from different
1580 metabolic pathways. Lastly, they were rewashed with wash buffer. Antibodies used are specified in the key

1581 resources table. Data were acquired using a Cytek Aurora full-spectrum cytometer at the CBM, and
1582 analysed with FlowJo software (versions 10 and 10.8.1; BD Biosciences).
1583
1584 **RNA Sequencing and Bioinformatic Analyses**
1585 The FACS gating strategy used to isolate LREs and MECs for RNA sequencing (RNA-seq) is shown in
1586 Figure S4A. Cell sorting was performed using a FACSAria Fusion cytometer (BD Biosciences). Each
1587 population was collected in biological triplicate samples of 300,000–500,000 cells. For LREs, each replicate
1588 consisted of pooled cells from multiple neonatal litters; for MECs, each replicate corresponded to a single
1589 mouse at postnatal day 42 (P42). Cells were collected in RLT buffer (Qiagen), and total RNA was extracted
1590 using the RNeasy Plus Micro Kit (Qiagen). Samples with an RNA integrity number (RIN) >7.0 were selected
1591 for RNA-seq. Ultra-low input poly(A)-selected libraries (single-end) were prepared in triplicate and
1592 sequenced using the Illumina HiSeq 2500 platform (50 bp, single-end reads) at the Centro de Análisis
1593 Genómico (CNAG-CRG, Barcelona, Spain). Reads were aligned to the Mus musculus reference genome
1594 (mm39) using HISAT2 (v2.1.0), and gene counts were obtained using HTSeq-count (v0.11.2). Differential
1595 gene expression analysis was performed with DESeq2. Gene Set Enrichment Analysis (GSEA)
1596 (Subramanian et al., 2005) was conducted using the clusterProfiler (Yu et al., 2012) and enrichplot
1597 packages within the R environment. Predefined gene sets from the Gene Ontology (GO) database were
1598 assessed for statistically significant enrichment based on a ranked list of gene expression values. The full
1599 gene dataset, annotated with ENSEMBL identifiers and their associated statistical metrics (stat), was
1600 utilized as input for the GSEA. Enrichment was quantified by normalized enrichment scores (NES), with
1601 significance determined at an adjusted p-value threshold of < 0.05 following Benjamini-Hochberg
1602 correction. Over-Representation Analysis (ORA) (Boyle et al., 2004) was performed in R using the
1603 clusterProfiler package. Differentially expressed genes (DEGs) with an adjusted p-value < 0.05 and
1604 mapped using ENTREZID identifiers were used. Enriched GO terms and KEGG pathways were also filtered
1605 at an adjusted p-value < 0.05 (Benjamini-Hochberg correction). Selected GO and KEGG terms were
1606 visualized using bubble plots generated in R with the GOplot package (GOBubble function) (Walter et al.,
1607 2015). The biocomputational data analysis was carried out by the Biocomputational Analysis Service
1608 (SABio) at the Centro de Biologia Molecular "Severo Ochoa" (CSIC-UAM).
1609
1610 **RNA Extraction, cDNA Synthesis, and RT-qPCR**
1611 Epithelial cells were lysed in 500 µL of TRIzol (Invitrogen) and stored at -80 °C until RNA extraction. RNA
1612 was isolated using the RNeasy Micro Kit (Qiagen) according to the manufacturer's instructions. For cDNA
1613 synthesis, 500 ng of RNA was reverse transcribed using the High-Capacity cDNA Reverse Transcription
1614 Kit (Applied Biosystems). Gene expression was assessed by quantitative PCR (qPCR) using gene-specific
1615 primer pairs (listed in Kay Resources Table). Reactions were performed in 384-well plates using either the
1616 CFX384 Real-Time System (Bio-Rad) or the ABI 7900HT Fast Real-Time PCR System (Applied
1617 Biosystems), with SYBR Green Master Mix (Agilent, Santa Clara, CA). Each well contained 10 ng of cDNA

1618 and 2.5 µM of each primer in a final volume of 10 µL. All reactions were run in technical triplicates.
1619 Cyclophilin B (*Ppib*) was used as the reference gene for normalisation.
1620
1621 **mtDNA Quantification**
1622 Genomic DNA (gDNA) was extracted using the NZY Tissue gDNA Isolation Kit (NZYTech). Relative
1623 mitochondrial DNA (mtDNA) content was determined by qPCR using primers for the following mitochondrial
1624 genes: NADH dehydrogenase 1 (*mt-Nd1*), cytochrome c oxidase subunits 1 and 2 (*mt-Co1* and *mt-Co2*),
1625 and ATP synthase subunit 6 (*mt-Atp6*). Reactions were performed in 384-well plates using the CFX384
1626 Real-Time System (Bio-Rad) with SYBR Green Master Mix (Agilent, Santa Clara, CA). Each well contained
1627 10 ng of gDNA and 2.5 µM of each primer in a final volume of 10 µL. All reactions were run in technical
1628 triplicates. Hexokinase 2 (*HK2*) was used as the reference gene for normalization, with primers listed in the
1629 Kay Resources Table.
1630
1631 **QUANTIFICATION AND STATISTICAL ANALYSIS**
1632 GraphPad software (versions 8.0.1 and 9.5.1) and Microsoft Excel were used for data analysis and plotting.
1633 Results shown are either representative or cumulative from at least two independent experiments. Except
1634 for gene expression analyses during development, RT-qPCR and WB data were normalized to the average
1635 of at least two WT or control mice of their corresponding litter. Sample size, statistical tests, and the meaning
1636 of the dots in each graph are specified in figure legends, except for TEM graphs (Figures 4C, 6F and S6O;
1637 samples sizes indicated in Table S1). In violin plots, median and interquartile range (IQR) are shown; in dot
1638 plots, mean ± SEM; in bar plots with dots, the mean + SEM; and in standard bar plots, the mean + SD.
1639 Outliers were identified using the ROUT method (Q = 5%) or Grubbs' test ($\alpha = 0.05$) for datasets with $n \geq$
1640 6. Normality was assessed using the Shapiro–Wilk test ($n < 50$) or the Kolmogorov–Smirnov test ($n > 50$).
1641 Statistical significance between two groups was determined using Student's t-test for parametric data or
1642 the Mann–Whitney test for nonparametric data. Welch's correction was applied when variances between
1643 groups were unequal. For comparisons among more than two groups, one-way ANOVA or two-way ANOVA
1644 with Tukey's post hoc test was used for parametric data, and the Kruskal–Wallis test, followed by Dunn's
1645 multiple comparison test, was used for nonparametric data. Survival curves were compared using the
1646 Gehan–Breslow–Wilcoxon test. A critical value for significance of $p < 0.05$ was used throughout the study
1647 (*$p < 0.05$, **$p < 0.01$, ***$p < 0.001$, ****$p < 0.0001$). In Figures 1H, 2A, 2H, S5B–C, S6F–H, S7A, S7B, S7E,
1648 and Table S2, only the most relevant statistically significant comparisons are shown; non-significant results
1649 are not displayed. In all other figures, statistical significance is indicated only when differences are
1650 significant.

Figure 1

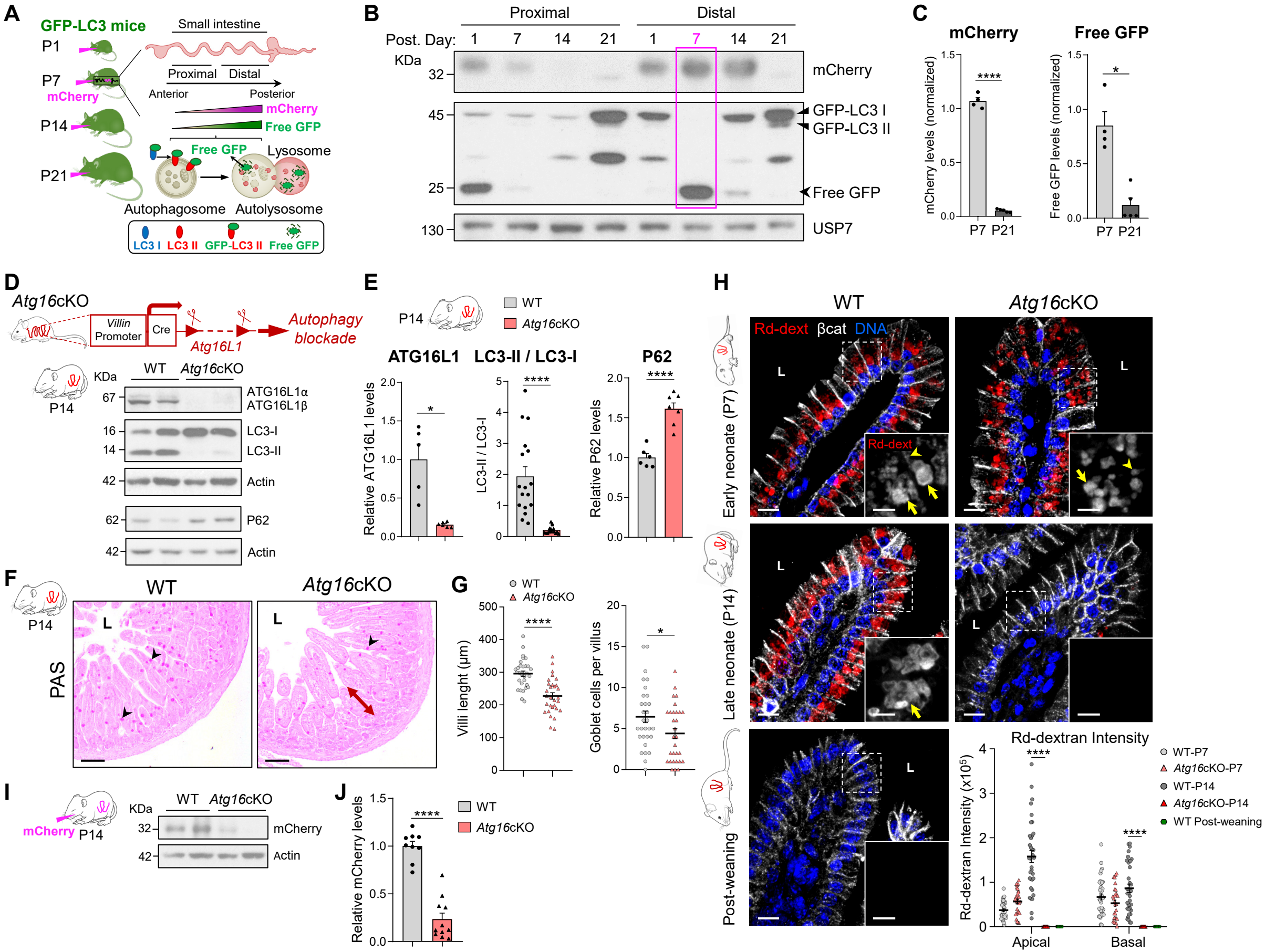
A
GFP-LC3 mice
P1
P7
mCherry
P14
P21
Small intestine
Proximal
Distal
Anterior
Posterior
mCherry
Free GFP
Free GFP
Lysosome
Autophagosome
Autolysosome
LC3 I
LC3 II
GFP-LC3 II
Free GFP
B
Proximal
Distal
Post. Day:
1
7
14
21
1
7
14
21
KDa
32
45
25
130
mCherry
GFP-LC3 I
GFP-LC3 II
Free GFP
USP7
C
mCherry
Free GFP
mCherry levels (normalized)
Free GFP levels (normalized)
****
*
P7
P21
D
Atg16cKO
Villin Promoter
Cre
Atg16L1
Autophagy blockade
P14
WT
Atg16cKO
KDa
67
16
14
42
62
42
ATG16L1α
ATG16L1β
LC3-I
LC3-II
Actin
P62
Actin
E
P14
WT
Atg16cKO
ATG16L1
LC3-II / LC3-I
P62
Relative ATG16L1 levels
LC3-II / LC3-I
Relative P62 levels
*
****
****
F
WT
Atg16cKO
P14
PAS
L
L
G
WT
Atg16cKO
Villi lenght (µm)
Goblet cells per villus
****
*
H
WT
Atg16cKO
Rd-dext
βcat
DNA
Early neonate (P7)
Late neonate (P14)
Post-weaning
L
Rd-dext
Rd-dextran Intensity
Rd-dextran Intensity (x10^5)
WT-P7
Atg16cKO-P7
WT-P14
Atg16cKO-P14
WT Post-weaning
****
****
Apical
Basal
I
mCherry
P14
KDa
WT
Atg16cKO
32
42
mCherry
Actin
J
Relative mCherry levels
WT
Atg16cKO
****

Figure 2

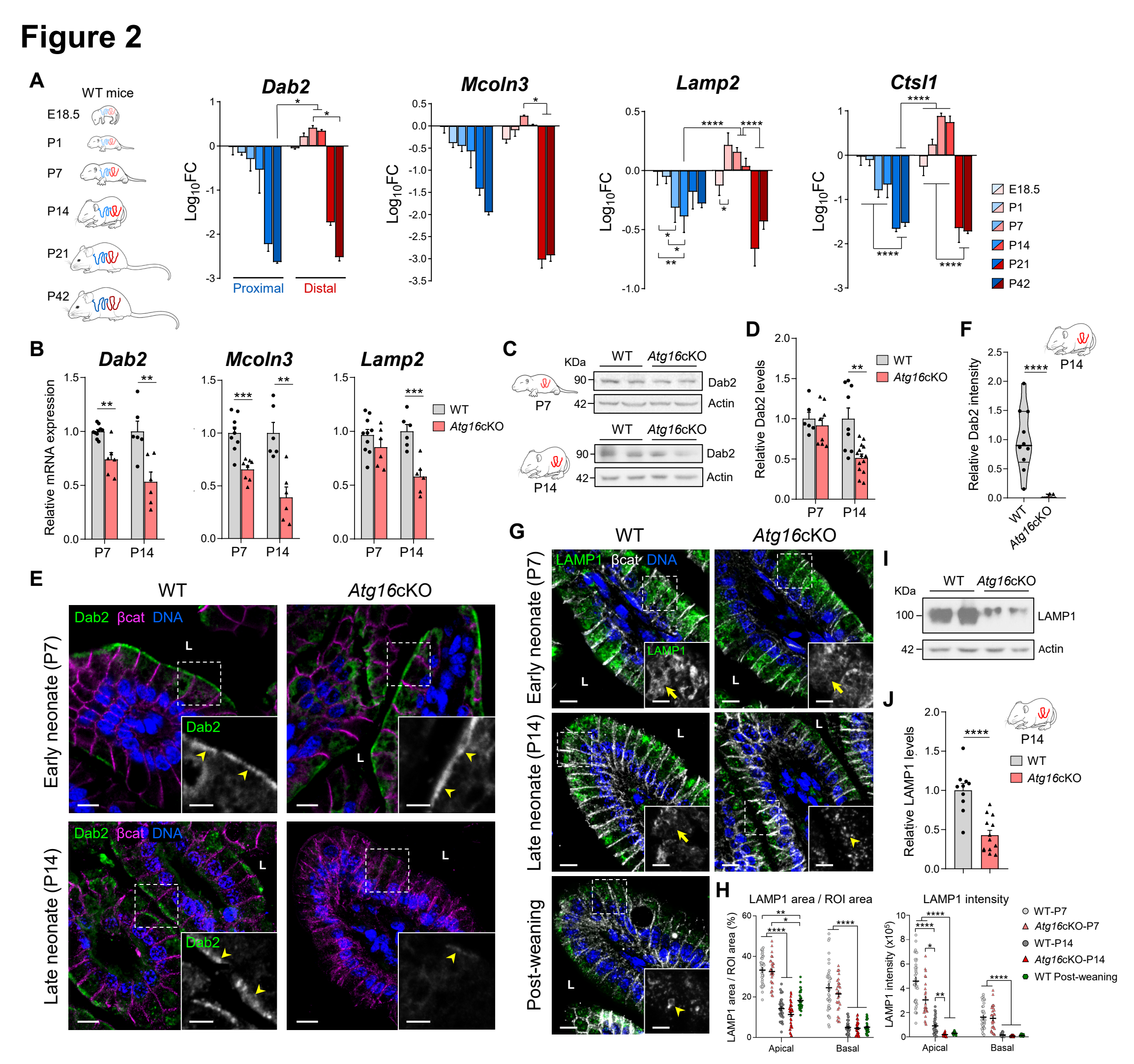
A
WT mice
E18.5
P1
P7
P14
P21
P42
Dab2
Mcoln3
Lamp2
Ctsl1
Log10FC
Proximal
Distal
E18.5
P1
P7
P14
P21
P42
B
Relative mRNA expression
WT
Atg16cKO
C
KDa
WT
Atg16cKO
90
42
Dab2
Actin
P7
P14
D
Relative Dab2 levels
F
Relative Dab2 intensity
WT
Atg16cKO
E
Dab2 βcat DNA
L
Early neonate (P7)
Late neonate (P14)
G
LAMP1 βcat DNA
LAMP1
Post-weaning
I
100
LAMP1
J
Relative LAMP1 levels
H
LAMP1 area / ROI area
LAMP1 intensity
LAMP1 intensity (x10^5)
Apical
Basal
WT-P7
Atg16cKO-P7
WT-P14
Atg16cKO-P14
WT Post-weaning

Figure 3

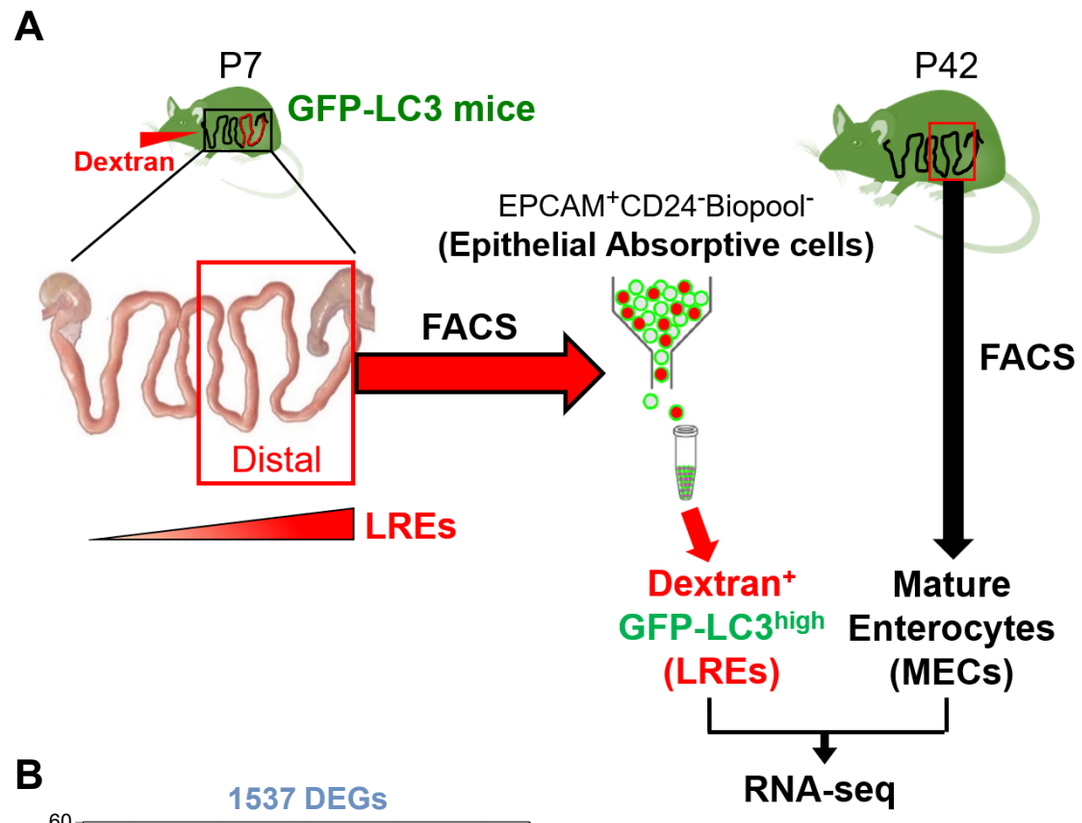
A
P7
GFP-LC3 mice
Dextran
Distal
LREs
EPCAM+CD24-Biopool-
(Epithelial Absorptive cells)
FACS
P42
FACS
Dextran+
GFP-LC3high
(LREs)
Mature
Enterocytes
(MECs)
RNA-seq

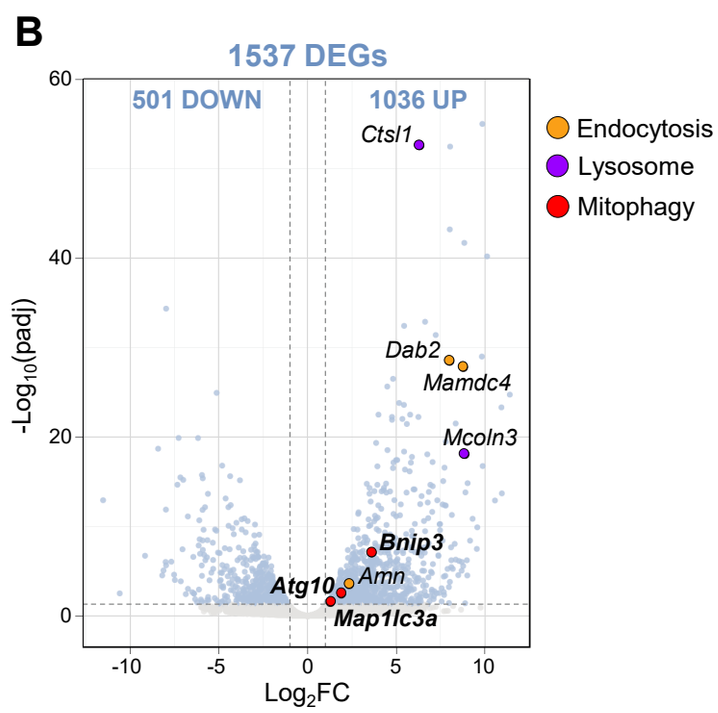
B
1537 DEGs
501 DOWN
1036 UP
Ctsl1
Dab2
Mamdc4
Mcoln3
Bnip3
Amn
Atg10
Map1lc3a
Endocytosis
Lysosome
Mitophagy
-Log10(padj)
Log2FC

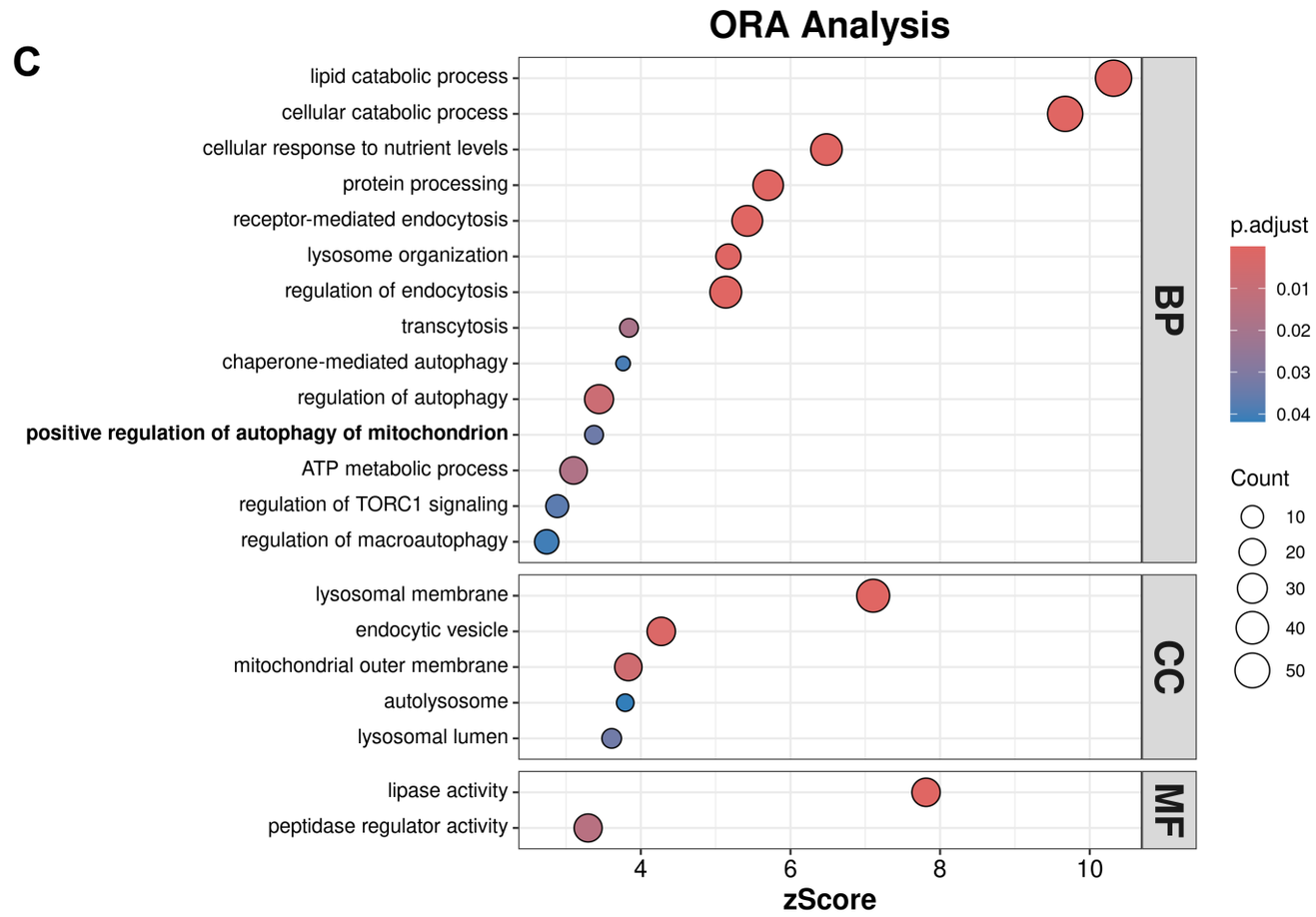
C
ORA Analysis
lipid catabolic process
cellular catabolic process
cellular response to nutrient levels
protein processing
receptor-mediated endocytosis
lysosome organization
regulation of endocytosis
transcytosis
chaperone-mediated autophagy
regulation of autophagy
positive regulation of autophagy of mitochondrion
ATP metabolic process
regulation of TORC1 signaling
regulation of macroautophagy
lysosomal membrane
endocytic vesicle
mitochondrial outer membrane
autolysosome
lysosomal lumen
lipase activity
peptidase regulator activity
BP
CC
MF
zScore
p.adjust
Count

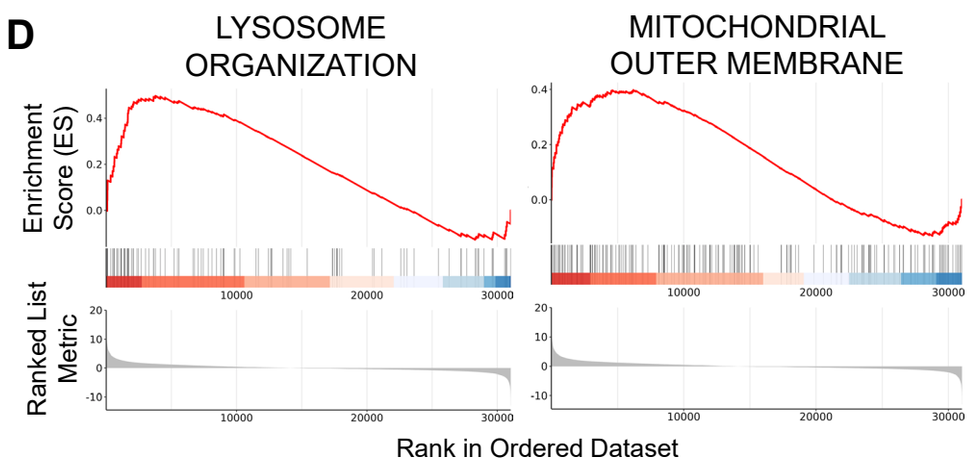
D
LYSOSOME ORGANIZATION
MITOCHONDRIAL OUTER MEMBRANE
Enrichment Score (ES)
Ranked List Metric
Rank in Ordered Dataset

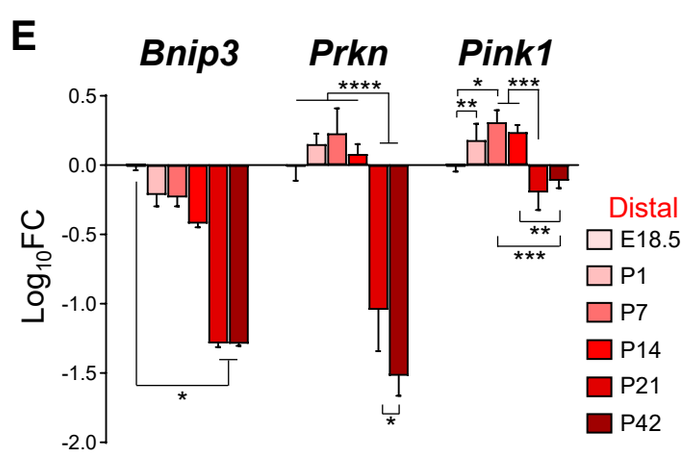
E
Bnip3
Prkn
Pink1
Log10FC
Distal
E18.5
P1
P7
P14
P21
P42

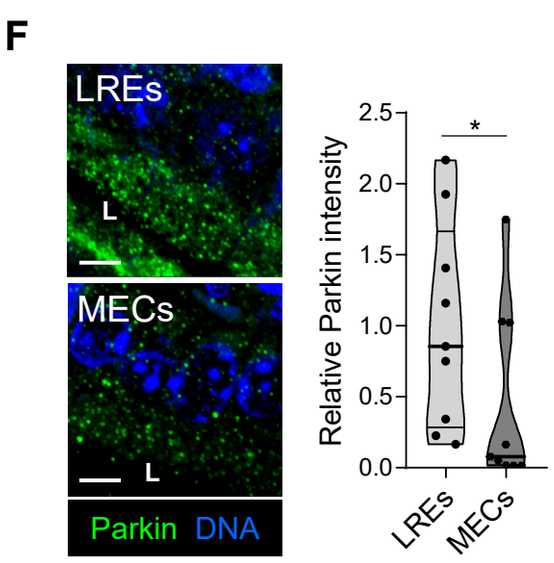
F
LREs
MECs
Parkin DNA
Relative Parkin intensity
LREs
MECs

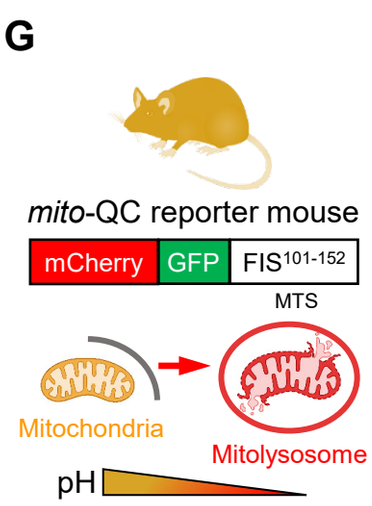
G
mito-QC reporter mouse
mCherry
GFP
FIS101-152
MTS
Mitochondria
Mitolysosome
pH

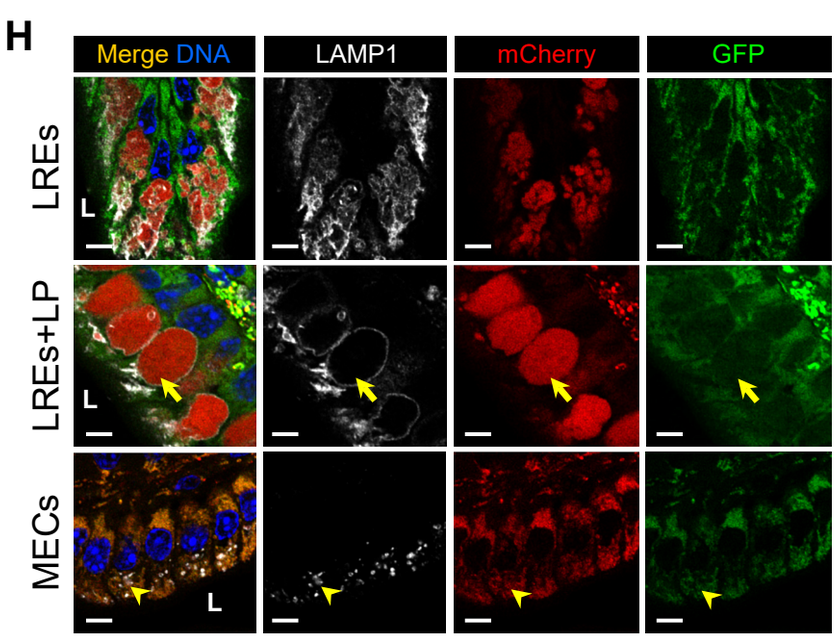
H
Merge DNA
LAMP1
mCherry
GFP
LREs
LREs+LP
MECs

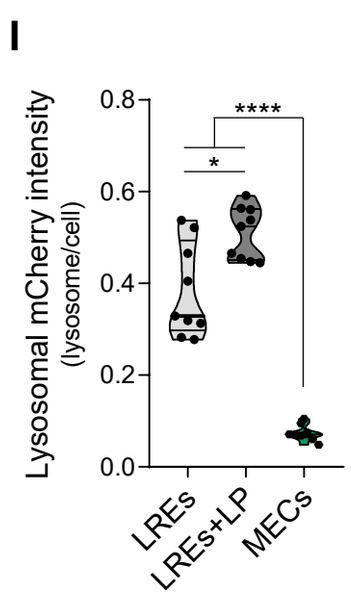
I
Lysosomal mCherry intensity
(lysosome/cell)
LREs
LREs+LP
MECs

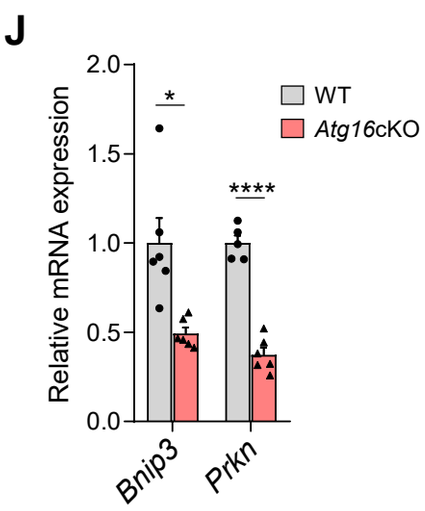
J
Relative mRNA expression
WT
Atg16cKO
Bnip3
Prkn

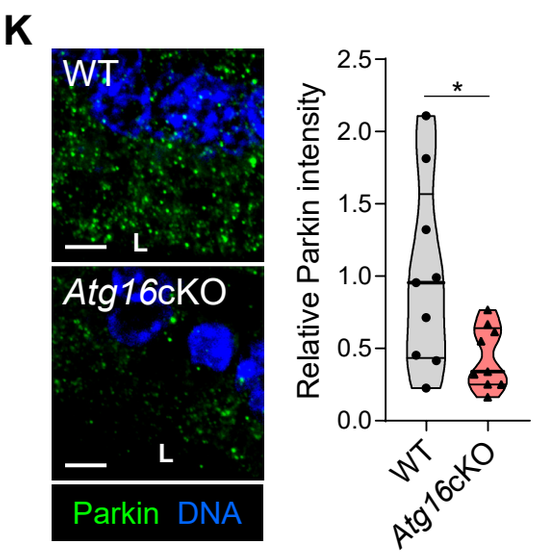
K
WT
Atg16cKO
Parkin DNA
Relative Parkin intensity
WT
Atg16cKO

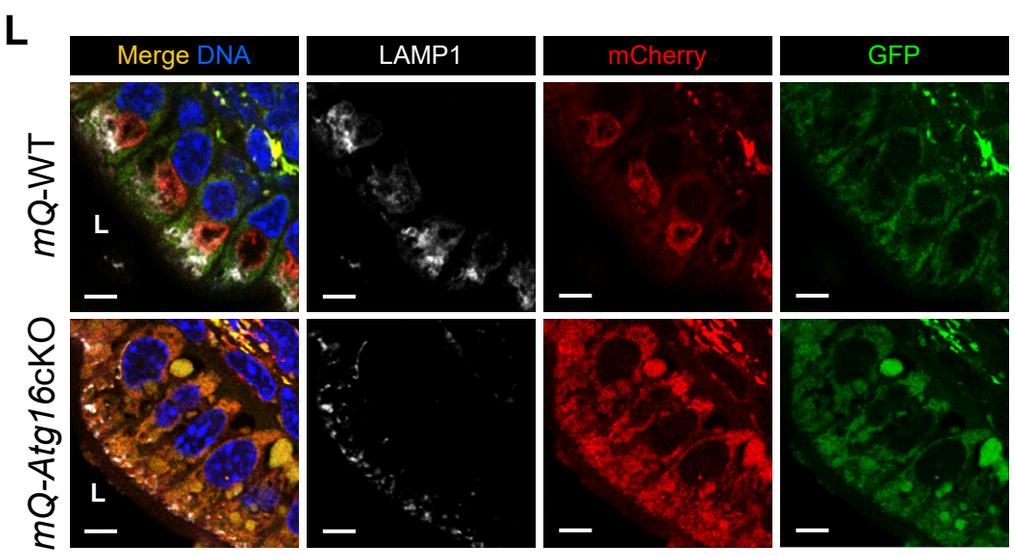
L
Merge DNA
LAMP1
mCherry
GFP
mQ-WT
mQ-Atg16cKO

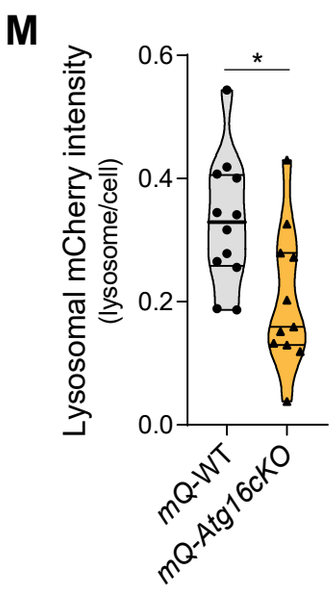
M
Lysosomal mCherry intensity
(lysosome/cell)
mQ-WT
mQ-Atg16cKO

Figure 4

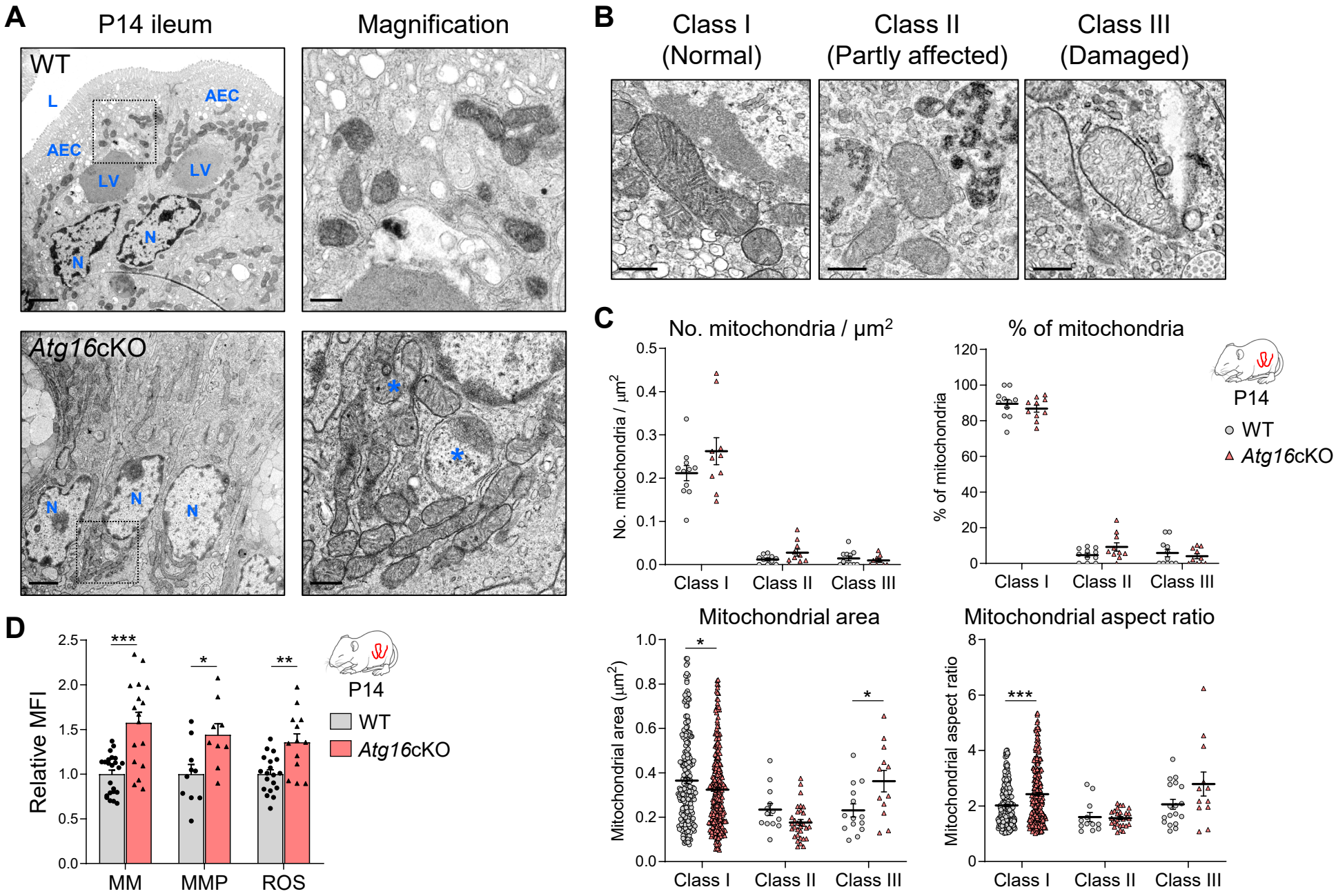
A
P14 ileum
Magnification
WT
L
AEC
AEC
LV
LV
N
N
Atg16cKO
N
N
N
B
Class I
(Normal)
Class II
(Partly affected)
Class III
(Damaged)
C
No. mitochondria / μm²
No. mitochondria / μm²
Class I
Class II
Class III
% of mitochondria
% of mitochondria
P14
WT
Atg16cKO
Mitochondrial area
Mitochondrial area (μm²)
Mitochondrial aspect ratio
Mitochondrial aspect ratio
D
Relative MFI
MM
MMP
ROS
P14
WT
Atg16cKO

Figure 5

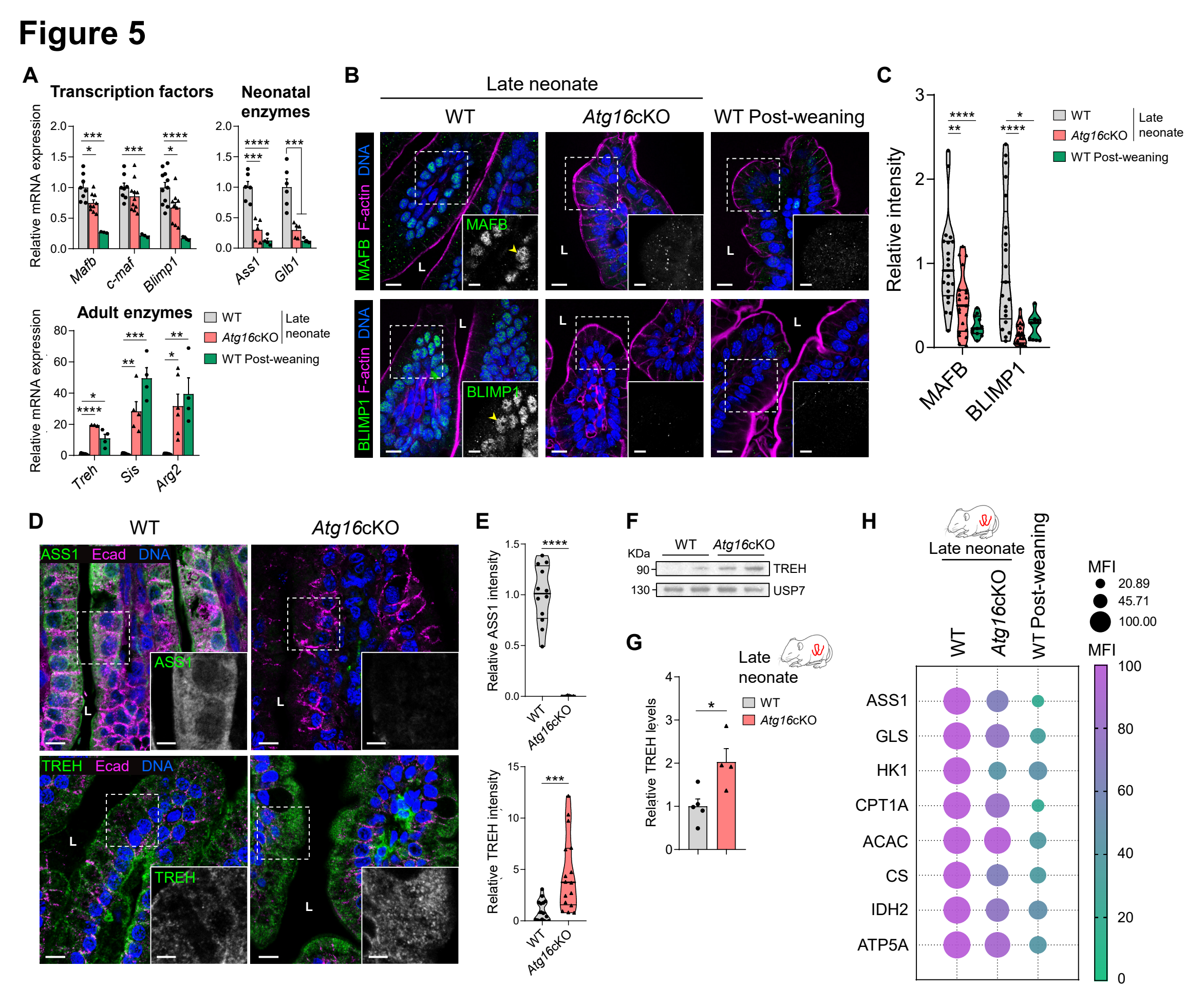
A
Transcription factors
Neonatal enzymes
Relative mRNA expression
Mafb
c-maf
Blimp1
Ass1
Glb1
Adult enzymes
Treh
Sis
Arg2
WT
Atg16cKO
WT Post-weaning
Late neonate
B
Late neonate
WT
Atg16cKO
WT Post-weaning
MAFB F-actin DNA
BLIMP1 F-actin DNA
MAFB
BLIMP1
L
C
Relative intensity
MAFB
BLIMP1
D
WT
Atg16cKO
ASS1 Ecad DNA
TREH Ecad DNA
ASS1
TREH
E
Relative ASS1 intensity
Relative TREH intensity
F
KDa
WT
Atg16cKO
90
130
TREH
USP7
G
Late neonate
Relative TREH levels
H
Late neonate
WT
Atg16cKO
WT Post-weaning
MFI
20.89
45.71
100.00
ASS1
GLS
HK1
CPT1A
ACAC
CS
IDH2
ATP5A

Figure 6

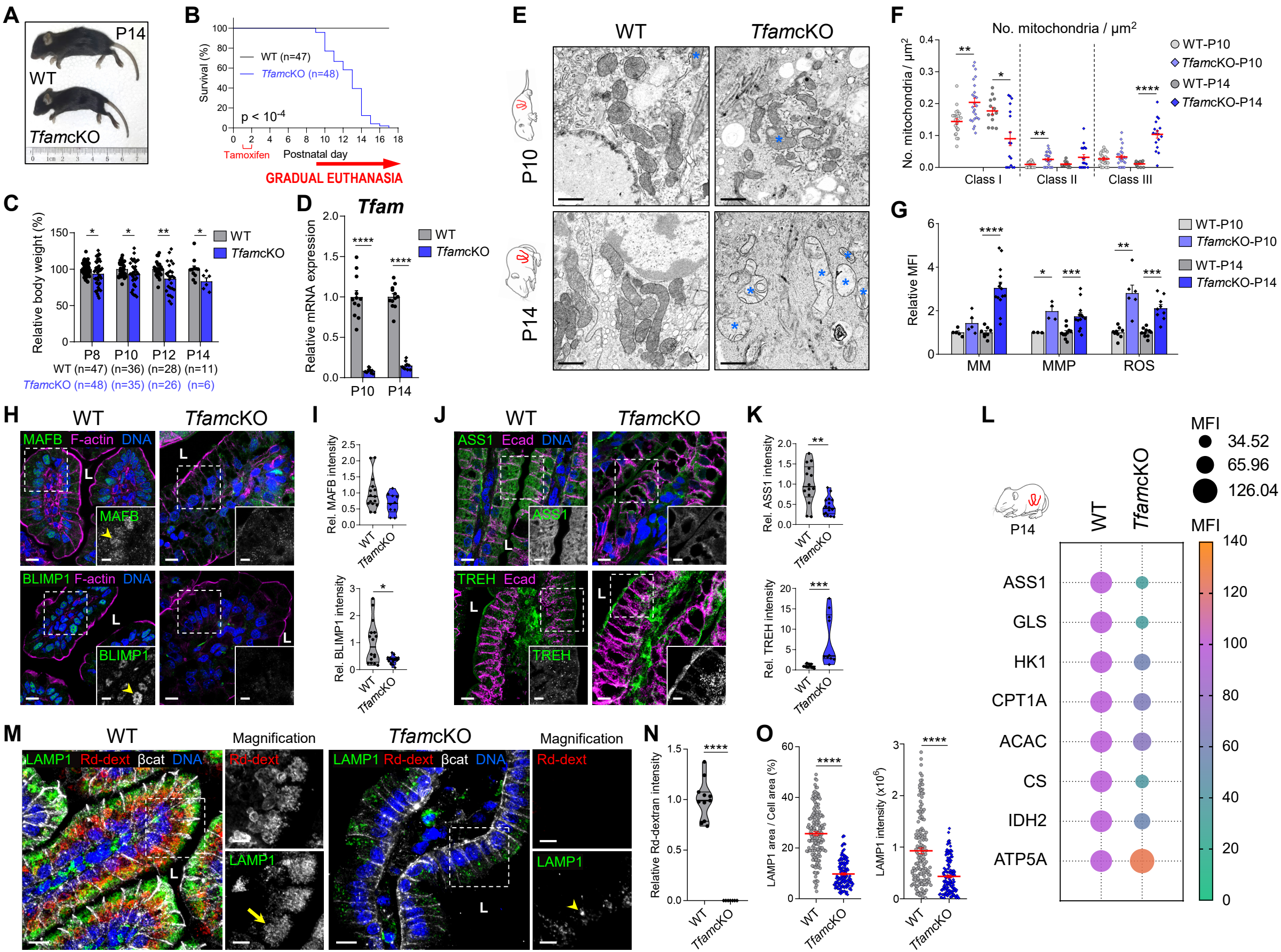
A
P14
WT
TfamcKO
B
Survival (%)
WT (n=47)
TfamcKO (n=48)
p < 10-4
Tamoxifen
Postnatal day
GRADUAL EUTHANASIA
C
Relative body weight (%)
WT
TfamcKO
P8 P10 P12 P14
WT (n=47) (n=36) (n=28) (n=11)
TfamcKO (n=48) (n=35) (n=26) (n=6)
D
Tfam
Relative mRNA expression
P10 P14
E
WT
TfamcKO
P10
P14
F
No. mitochondria / µm2
WT-P10
TfamcKO-P10
WT-P14
TfamcKO-P14
Class I
Class II
Class III
G
Relative MFI
MM
MMP
ROS
H
WT
TfamcKO
MAFB F-actin DNA
MAFB
BLIMP1 F-actin DNA
BLIMP1
Rel. MAFB intensity
Rel. BLIMP1 intensity
I
J
ASS1 Ecad DNA
ASS1
TREH Ecad
TREH
K
Rel. ASS1 intensity
Rel. TREH intensity
L
MFI
34.52
65.96
126.04
P14
ASS1
GLS
HK1
CPT1A
ACAC
CS
IDH2
ATP5A
M
WT
TfamcKO
Magnification
LAMP1 Rd-dext βcat DNA
Rd-dext
LAMP1
N
Relative Rd-dextran intensity
O
LAMP1 area / Cell area (%)
LAMP1 intensity (x10^6)

Figure 7

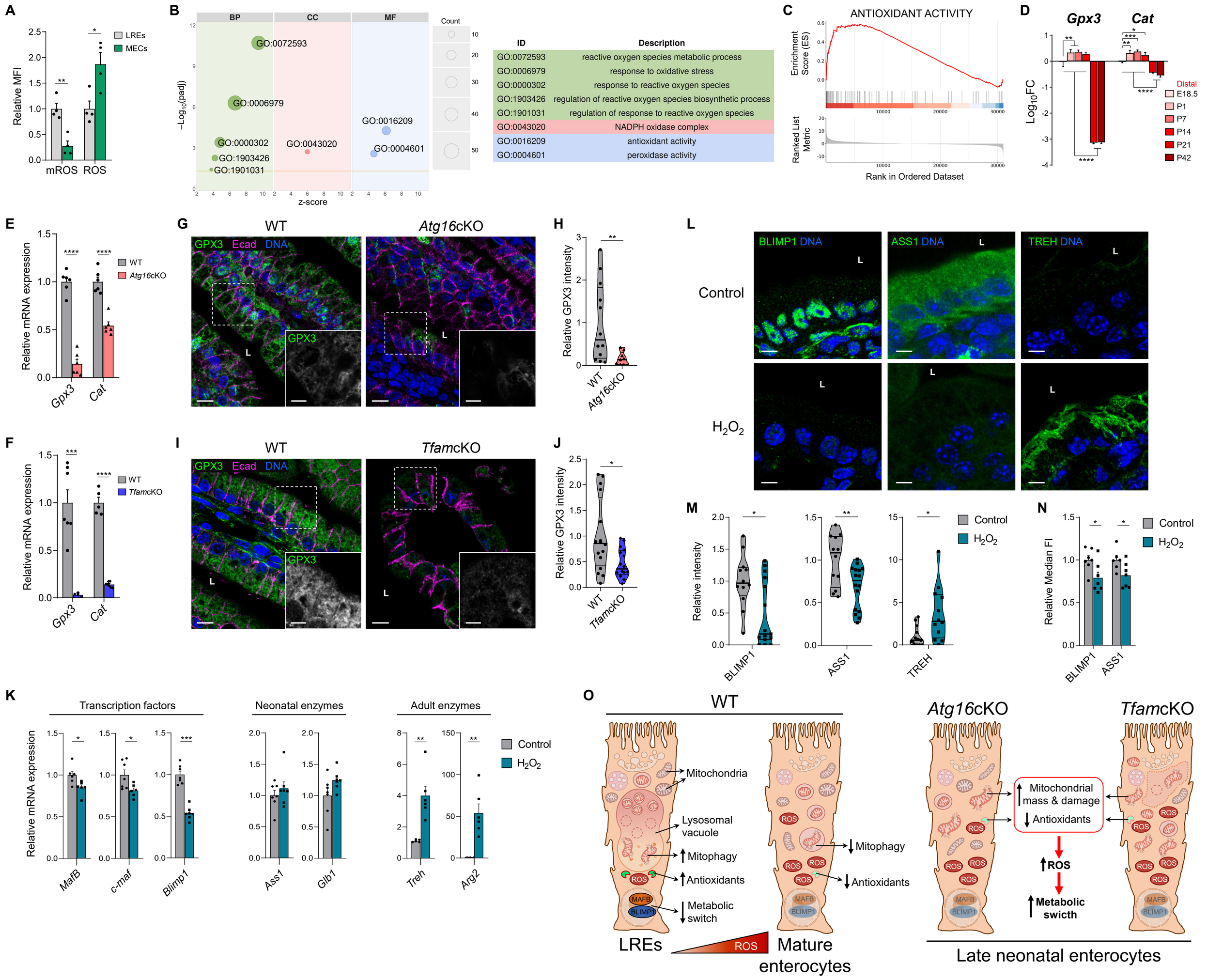
A
Relative MFI
LREs
MECs
mROS
ROS
B
BP
CC
MF
Count
GO:0072593
GO:0006979
GO:0000302
GO:1903426
GO:1901031
GO:0043020
GO:0016209
GO:0004601
z-score
ID
Description
GO:0072593 reactive oxygen species metabolic process
GO:0006979 response to oxidative stress
GO:0000302 response to reactive oxygen species
GO:1903426 regulation of reactive oxygen species biosynthetic process
GO:1901031 regulation of response to reactive oxygen species
GO:0043020 NADPH oxidase complex
GO:0016209 antioxidant activity
GO:0004601 peroxidase activity
C
ANTIOXIDANT ACTIVITY
Enrichment Score (ES)
Ranked List Metric
Rank in Ordered Dataset
D
Gpx3
Cat
Log10FC
Distal
E18.5
P1
P7
P14
P21
P42
E
Relative mRNA expression
WT
Atg16cKO
Gpx3
Cat
F
Relative mRNA expression
WT
TfamcKO
Gpx3
Cat
G
WT
Atg16cKO
GPX3 Ecad DNA
GPX3
L
H
Relative GPX3 intensity
WT
Atg16cKO
I
WT
TfamcKO
GPX3 Ecad DNA
GPX3
L
J
Relative GPX3 intensity
WT
TfamcKO
K
Transcription factors
Neonatal enzymes
Adult enzymes
Relative mRNA expression
Control
H2O2
MafB
c-maf
Blimp1
Ass1
Glb1
Treh
Arg2
L
BLIMP1 DNA
ASS1 DNA
TREH DNA
Control
H2O2
M
Relative intensity
Control
H2O2
BLIMP1
ASS1
TREH
N
Relative Median FI
Control
H2O2
BLIMP1
ASS1
O
WT
Mitochondria
Lysosomal vacuole
Mitophagy
Antioxidants
Metabolic switch
ROS
MAFB
BLIMP1
LREs
Mature enterocytes
Atg16cKO
TfamcKO
Mitochondrial mass & damage
Antioxidants
ROS
Metabolic switch
Late neonatal enterocytes

Figure S1

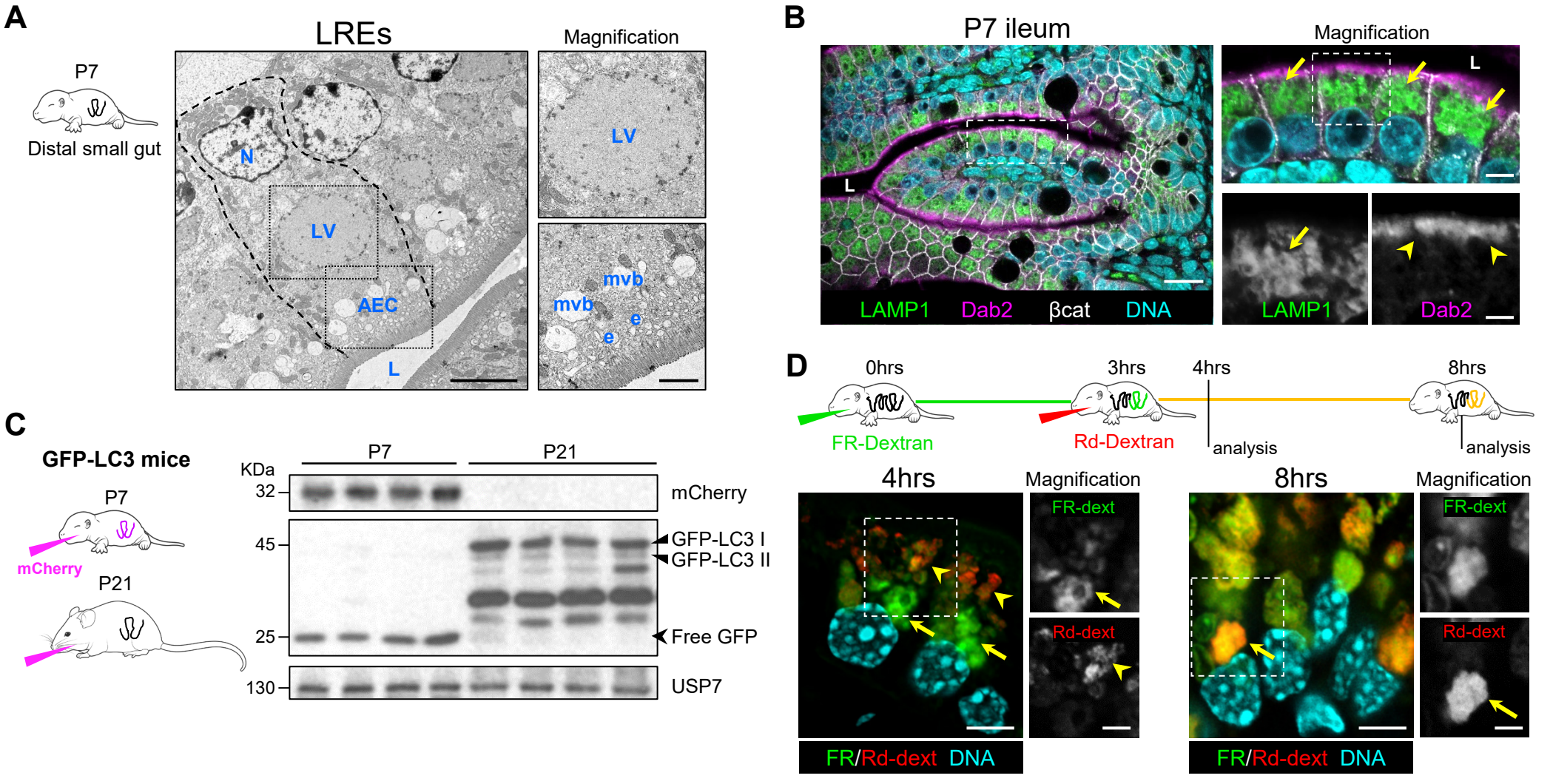
A
P7
Distal small gut
LREs
Magnification
N
LV
AEC
L
LV
mvb
mvb
e
e
B
P7 ileum
Magnification
L
L
LAMP1
Dab2
βcat
DNA
LAMP1
Dab2
C
GFP-LC3 mice
P7
mCherry
P21
KDa
P7
P21
32
45
25
130
mCherry
GFP-LC3 I
GFP-LC3 II
Free GFP
USP7
D
0hrs
3hrs
4hrs
8hrs
FR-Dextran
Rd-Dextran
analysis
analysis
4hrs
Magnification
8hrs
Magnification
FR-dext
Rd-dext
FR-dext
Rd-dext
FR/Rd-dext DNA
FR/Rd-dext DNA

Figure S2

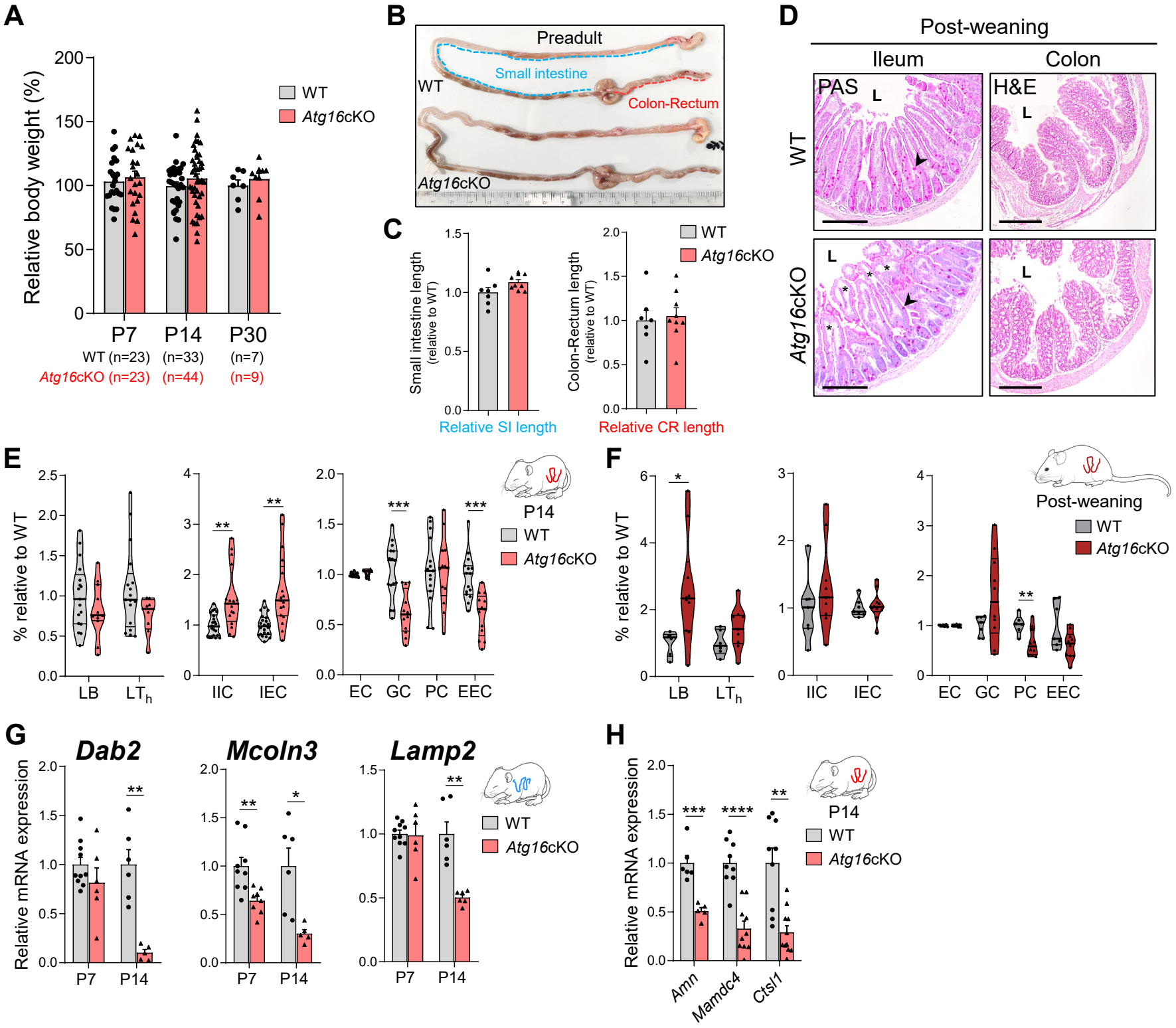
A
Relative body weight (%)
WT
Atg16cKO
P7
P14
P30
WT (n=23) (n=33) (n=7)
Atg16cKO (n=23) (n=44) (n=9)
B
Preadult
Small intestine
Colon-Rectum
WT
Atg16cKO
C
Small intestine length (relative to WT)
Colon-Rectum length (relative to WT)
Relative SI length
Relative CR length
D
Post-weaning
Ileum
Colon
PAS
H&E
L
E
% relative to WT
LB
LTh
IIC
IEC
EC
GC
PC
EEC
P14
F
Post-weaning
G
Dab2
Mcoln3
Lamp2
Relative mRNA expression
H
Amn
Mamdc4
Ctsl1

Figure S3

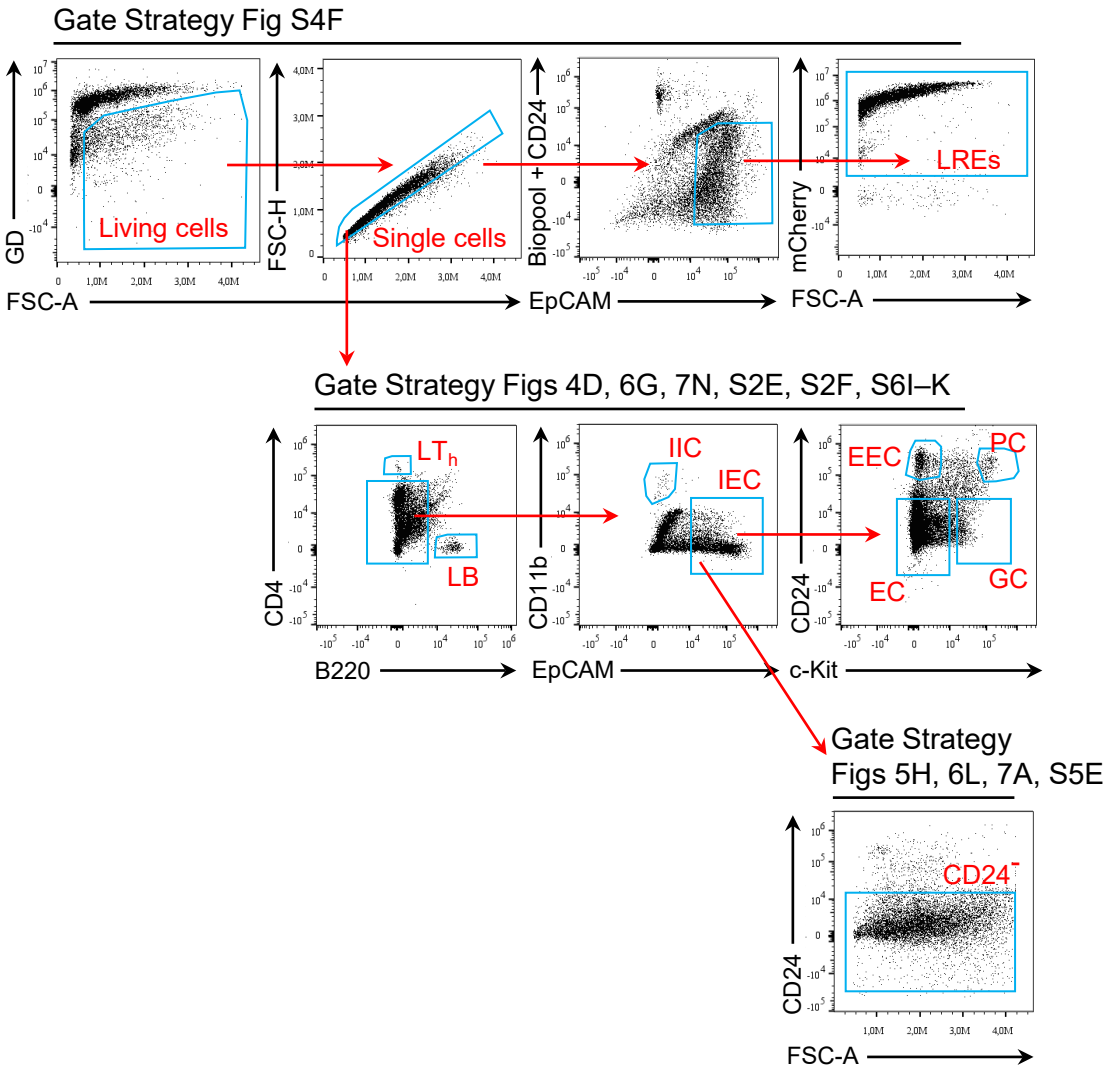
Gate Strategy Fig S4F
Living cells
Single cells
LREs
GD
FSC-A
FSC-H
Biopool + CD24
EpCAM
mCherry
FSC-A
Gate Strategy Figs 4D, 6G, 7N, S2E, S2F, S6I–K
LTh
LB
IIC
IEC
EEC
PC
EC
GC
CD4
B220
CD11b
EpCAM
CD24
c-Kit
Gate Strategy
Figs 5H, 6L, 7A, S5E
CD24-
CD24
FSC-A

Figure S4

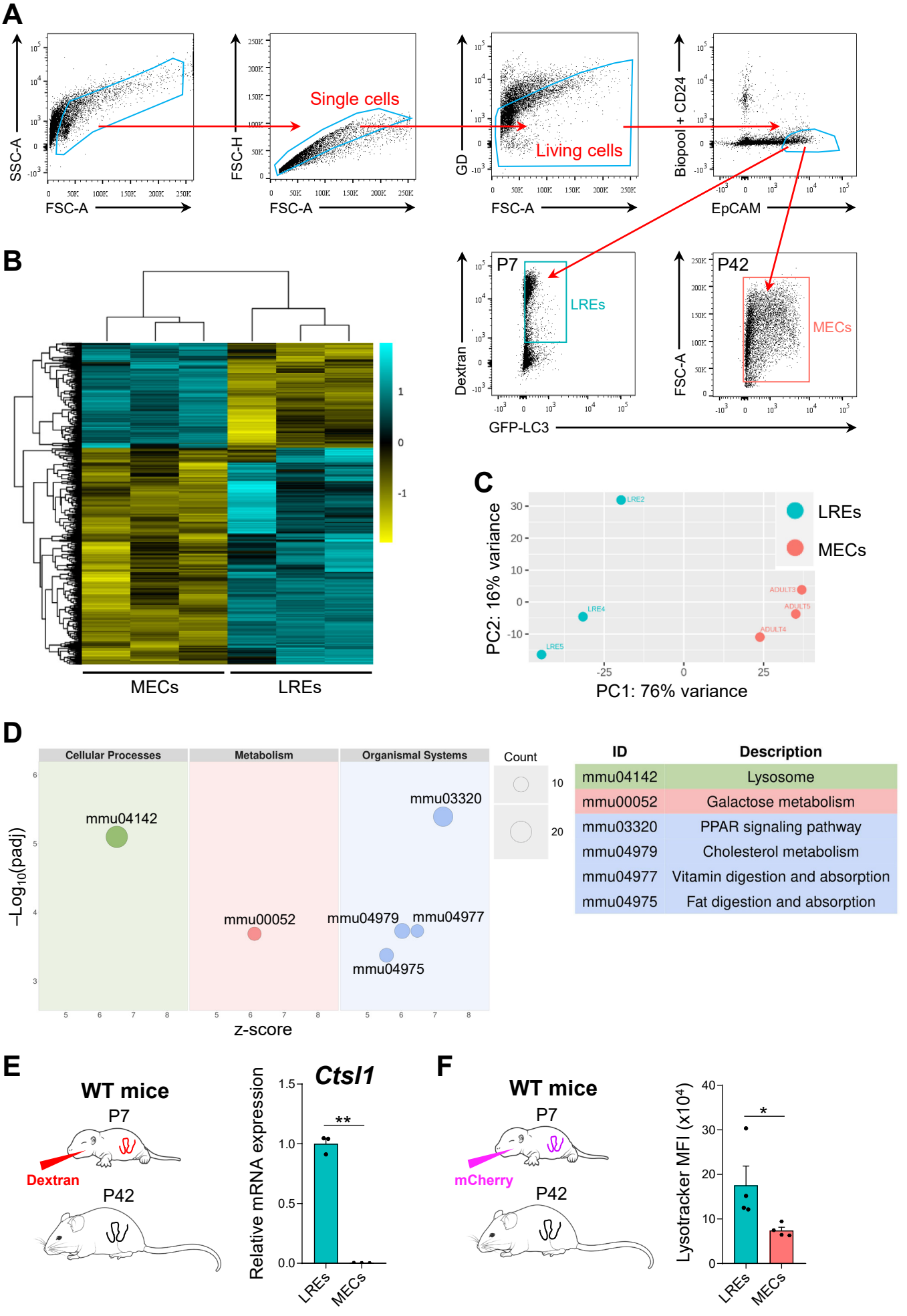
A
SSC-A
FSC-A
FSC-H
Single cells
GD
Living cells
Biopool + CD24
EpCAM
P7
LREs
P42
MECs
Dextran
FSC-A
GFP-LC3
B
1
0
-1
MECs
LREs
C
LREs
MECs
PC2: 16% variance
PC1: 76% variance
LRE2
LRE4
LRE5
ADULT3
ADULT5
ADULT4
D
Cellular Processes
Metabolism
Organismal Systems
Count
10
20
mmu04142
mmu03320
mmu00052
mmu04979
mmu04977
mmu04975
–Log10(padj)
z-score
ID
Description
mmu04142 Lysosome
mmu00052 Galactose metabolism
mmu03320 PPAR signaling pathway
mmu04979 Cholesterol metabolism
mmu04977 Vitamin digestion and absorption
mmu04975 Fat digestion and absorption
E
WT mice
P7
Dextran
P42
Ctsl1
Relative mRNA expression
**
LREs
MECs
F
WT mice
P7
mCherry
P42
Lysotracker MFI (x10⁴)
*
LREs
MECs

Figure S5

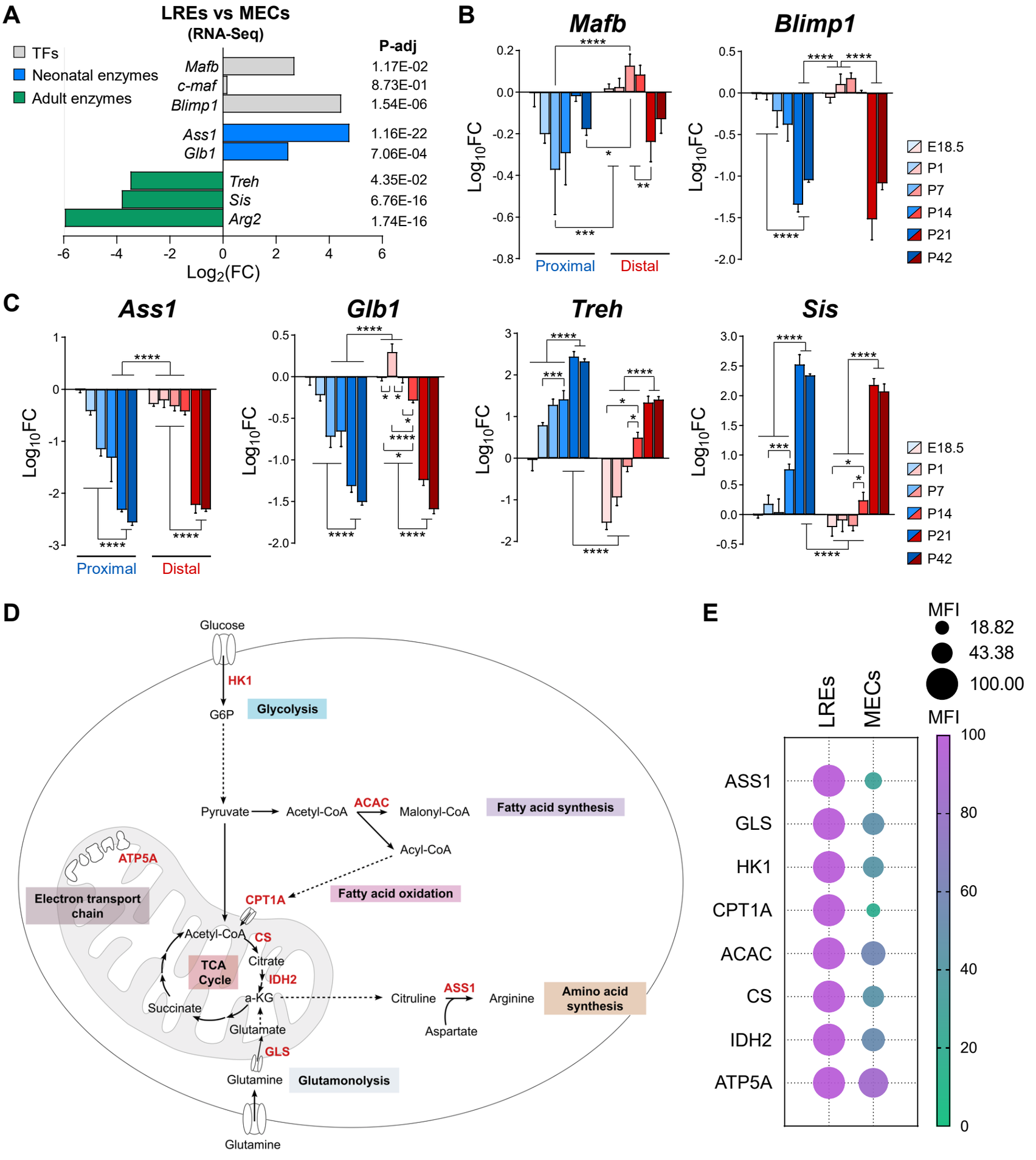
A
LREs vs MECs
(RNA-Seq)
TFs
Neonatal enzymes
Adult enzymes
P-adj
Mafb 1.17E-02
c-maf 8.73E-01
Blimp1 1.54E-06
Ass1 1.16E-22
Glb1 7.06E-04
Treh 4.35E-02
Sis 6.76E-16
Arg2 1.74E-16
Log2(FC)
B
Mafb
Blimp1
Log10FC
Proximal
Distal
E18.5
P1
P7
P14
P21
P42
C
Ass1
Glb1
Treh
Sis
D
Glucose
HK1
G6P
Glycolysis
Pyruvate
Acetyl-CoA
ACAC
Malonyl-CoA
Fatty acid synthesis
Acyl-CoA
ATP5A
Electron transport chain
CPT1A
Fatty acid oxidation
Acetyl-CoA
CS
Citrate
TCA Cycle
IDH2
a-KG
Succinate
Citruline
ASS1
Arginine
Amino acid synthesis
Aspartate
Glutamate
GLS
Glutamine
Glutamonolysis
Glutamine
E
MFI
18.82
43.38
100.00
LREs
MECs
ASS1
GLS
HK1
CPT1A
ACAC
CS
IDH2
ATP5A
100
80
60
40
20
0

Figure S6

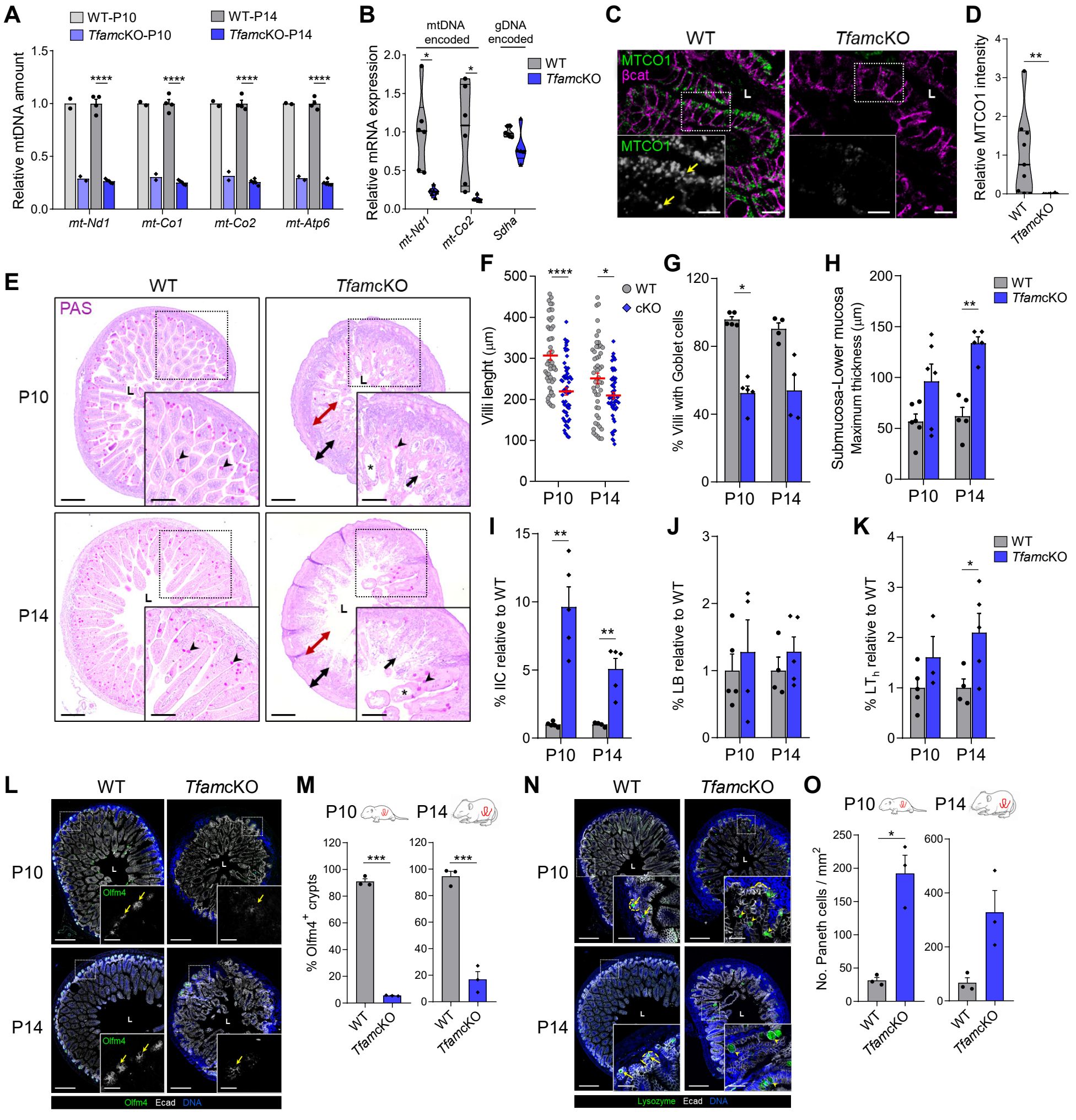
A
WT-P10
TfamcKO-P10
WT-P14
TfamcKO-P14
Relative mtDNA amount
mt-Nd1
mt-Co1
mt-Co2
mt-Atp6
B
mtDNA encoded
gDNA encoded
Relative mRNA expression
WT
TfamcKO
mt-Nd1
mt-Co2
Sdha
C
WT
TfamcKO
MTCO1
βcat
L
D
Relative MTCO1 intensity
E
WT
TfamcKO
PAS
P10
P14
F
Villi lenght (µm)
WT
cKO
G
% Villi with Goblet cells
H
Submucosa-Lower mucosa Maximum thickness (µm)
I
% IIC relative to WT
J
% LB relative to WT
K
% LTh relative to WT
L
Olfm4
Olfm4 Ecad DNA
M
% Olfm4+ crypts
N
Lysozyme Ecad DNA
O
No. Paneth cells / mm2
P
% of mitochondria
Mitochondrial area
Mitochondrial aspect ratio
Class I
Class II
Class III
WT-P10
TfamcKO-P10
WT-P14
TfamcKO-P14

Figure S7

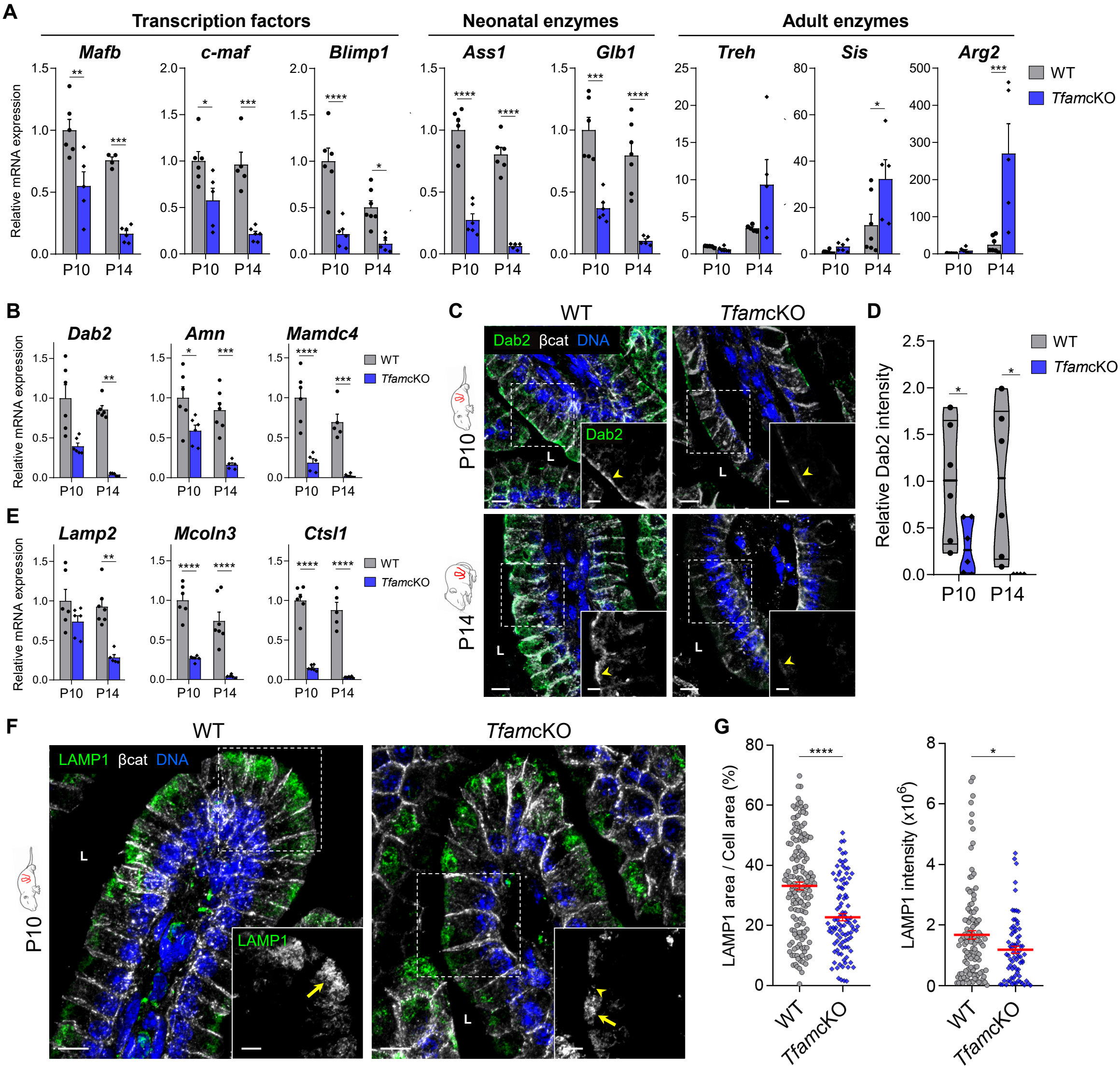
A
Transcription factors
Neonatal enzymes
Adult enzymes
Mafb
c-maf
Blimp1
Ass1
Glb1
Treh
Sis
Arg2
Relative mRNA expression
P10
P14
WT
TfamcKO
B
Dab2
Amn
Mamdc4
C
WT
TfamcKO
Dab2 βcat DNA
Dab2
L
P10
P14
D
Relative Dab2 intensity
E
Lamp2
Mcoln3
Ctsl1
F
LAMP1 βcat DNA
LAMP1
G
LAMP1 area / Cell area (%)
LAMP1 intensity (x10^6)

Table S1

	Class	No. mitochondria / μm^2	% of mitochondria	Mitochondrial area	Mitochondrial aspect ratio
Figure 4C	I	11, 10	11, 10	239, 271	239, 276
	II	11, 10	11, 10	13, 32	12, 28
	III	11, 9	11, 10	14, 12	18, 12
Figures 6F and S6P	I	23, 24, 13, 17	23, 24, 13, 17	184, 321, 259, 128	169, 329, 251, 130
	II	23, 24, 13, 17	23, 24, 12, 17	19, 73, 14, 45	21, 74, 15, 44
	III	23, 24, 13, 17	23, 24, 13, 17	45, 78, 17, 134	47, 78, 16, 149

Table S2

Protein	Figure 5H		Figure 6L	Figure S5E
	WT vs *Atg16*cKO	WT-P14 vs WT-Preadult		
ASS1	*	****	***	***
GLS	*	****	****	**
HK1	***	**	**	–
CPT1A	*	****	***	****
ACAC	NS	****	***	**
CS	****	****	***	****
IDH2	****	****	****	*
ATP5A	NS	****	*	NS